THE DEVELOPMENT OF 3D TISSUE AND NOVEL PHOTONICS TECHNOLOGIES FOR BIO-MEDICAL THERAGNOSTIC

Arooj

Doctor of Philosophy

Aston University

February 2025

Abstract

3D *in-vitro* models have emerged as substitutes of complex tissue structures of human body. These models can depict *in-vivo* conditions of real tissues and can be utilized as valuable tools for per-clinical applications. This work presented development of 3D *in-vitro* tissue models of full-thickness skin equivalents (FSE) and Melanoma full-thickness skin equivalents (Melanoma-FSE). The development of 3D architecture of FSE and Melanoma-FSE are crucial requirement for investigation of skin pathologies, personalized skin disease treatments, disease modelling, drug testing.

We designed high-resolution 3D scaffolds to support the growth and maturation of these skin models. Additionally, we developed and validated a cost-effective, custom-built system combining fluorescence spectroscopy (FS) and optical coherence tomography (OCT) for non-destructive analysis of the metabolism and morphology of 3D FSEs. This system proved highly sensitive in detecting fluorescence from key metabolic co-enzymes (NADH/NADPH and FAD) in solutions and cell suspensions, while OCT provided adequate resolution to observe the morphology of FSEs. As a result, both the 3D FSE model and the dual-mode optical system hold significant potential for use in 3D bioprinting of biological tissues, as well as in the development of cosmetics, drugs, and in monitoring their maturation over time.

In scaffold fabrication, we explored two latest emerging bioprinting technologies: Digital Light Processing (DLP) and Two-Photon Polymerization (2PP). The difference between 3D tissue engineered constructs by using these two methods are presented to demonstrate the selection of technology considering to the specific application and tissue construction. For microscale functional tissue structures, 2PP is unique and precise method but having some limitations as compared to DLP.

Furthermore, due to therapeutic potential of 1267nm laser irradiation, it is used for generation of singlet oxygen without using photosensitizer (PS). 1267nm laser-induced $^1O_2$ production can cause massive oxidative effect on cellular functions, e.g., mitochondrial dysfunction with mtDNA degradation, cancer cell death. In this study, we investigated real time monitoring of production and role of $^1O_2$ in apoptosis with the aim of optimizing therapeutic outcomes. We found that $^1O_2$ caused the initiation of apoptosis in melanoma cancer cell line more effectively as compared to the primary human fibroblasts and HaCaT cells. Collectively, this work demonstrates the integration of tissue engineering, optical diagnostics and phototherapy for advancing diagnostics and treatment.

Acknowledgement

All praises and thanks to Almighty Allah for granting me the strength, health, and opportunity to undertake and complete this PhD research project. I would like to begin by expressing my deepest gratitude to my parents, especially my beloved father, M. Khalid Hussain Hashmi (Late), and my mother, Bushra Bibi (Late). I am also deeply thankful to my uncle M. Aslam Hashmi as well as Parveen Akhtar and Balqees Akhtar (Late) for their love and prayers. May Allah (SWT) grant them the highest rank in Jannah and enable me to make them proud through my work and life.

I extend my sincere appreciation to my supervisor Professor Edik Rafailov and my associate supervisor Dr. Sergei Sokolovski for their support and giving me an opportunity to work on this research project. My gratitude also goes to my whole research group, especially Dr. Viktor Dremin for his support and guidance throughout this journey. A very special thanks to Dr. Kirill Tokmakov for his support during crucial phases of my research.

I am also deeply thankful to Dr. Shazia Bashir and to my brothers Dr. Awais Khalid, Bilal Khalid, and Jahanzeb Khalid along with my sister, Saima Shafique, for their unwavering encouragement. My heartfelt thanks also go to my dear aunty, Sabiha Nasreen, whose support has meant so much.

To my friends Dr. Abdul Raheem, Abdullah, Hira, Erum, Sana, and Safiya thank you for your companionship and encouragement. A special note of gratitude to Aisha Bibi and Zia Bhai for their exceptional support and friendship. I am also grateful to my office mates, who made this journey both productive and memorable.

Finally, I would like to express my sincere thanks to my uncle and aunt, Mr. Khalid and Mrs. Shazia Khalid. Their unwavering support, kindness, and generosity made my time in the UK feel like a second home.

List of abbreviation

ETC	Electron transport chain
NIR	Near Infrared
ECM	Extra cellular matrix
ATP	Adenosine triphosphate
ADP	Adenosine diphosphate
ROS	Reactive oxygen species
$^1O_2$	Singlet oxygen
CCO	Cytochrome C Oxidase
mt-DNA	Mitochondrial DNA
NADH	Nicotinamide adenine dinucleotide
NADPH	Nicotinamide adenine dinucleotide phosphate
FAD	Flavin adenine dinucleotide
OCT	Optical coherence tomography
FS	Fluorescence spectroscopy
DMEM	Dulbecco's modified eagle's medium
DPBS	Dulbecco's phosphate-buffered saline
DMSO	Dimethyl sulfoxide
Fb	Fibroblasts
HaCaT	Immortalized keratinocytes
Fb +FG	Fibroblasts+ fibrinogen gel
FSE	Full-thickness skin equivalent
Melanoma-FSE	Melanoma-full-thickness skin equivalent
ORR	Optical redox ratio
TE	Tissue engineering
SLA	Stereolithography
DLP	Digital light processing
2PP	Two-photon polymerization
PDT	Photodynamic therapy
PDD	Photodynamic diagnostics
PBM	Photobiomodulation

TNRF	Tumour necrosis Factor Receptor
IHC	Immunohistochemistry
RGP	Radial growth phase
VGP	Vertical growth phase
VGP	Photosensitiser
PS	Fluorescein Isothiocyanate
FITC	Tumour necrosis Factor Receptor
TNRF	Si-rhodamine moieties and 9,10-
Si-DMA	Dimethylanthracene

List of Figures

List of tables

Contents

Motivation

This dissertation consists of three interconnected but independent parts. The motivation behind this thesis is to combine the following three directions for the purpose of theragnostic.

1)The validity of multi-modal device for purpose of diagnostics

2) 3D-Bioprinting and tissue development

3) Near-infrared laser wavelength for purpose of treatment of cancer

Challenges and objectives

Main objectives of this PhD research work:

- Review of relevant literature and understand about the different methodologies regarding to diagnostics and treatment of different medical health issues especially melanoma cancer.
- Culturing of different cells, primary fibroblasts, HaCaT cells, melanoma cells for the purpose of 2D and 3D culturing.
- Culture Full Skin Equivalence (FSE) Model and Melanoma Full Skin Equivalence (Melanoma-FSE) for the purpose of diagnosis and treatment.

Implementation of near-infrared (NIR) laser with wavelength of 1267 (CW) mode for the purpose of treatment of cancerous cells in vitro.

Chapter 1

Literature Review

This chapter reviews background literature that will be used throughout the following chapters.

1.1 Electromagnetic spectrum

The electromagnetic spectrum (EM) is composed the range of wavelengths of light as shown in Figure 1.1, EM waves associated with photons having specific energy. The spectrum consists of cosmic radiations, gamma rays, x-rays, UV rays, visible light, infrared radiations and radio waves [1]. At present in medicine, both LEDs and lasers are used for different applications. LEDs and lasers are selected according to the required medical applications [2].

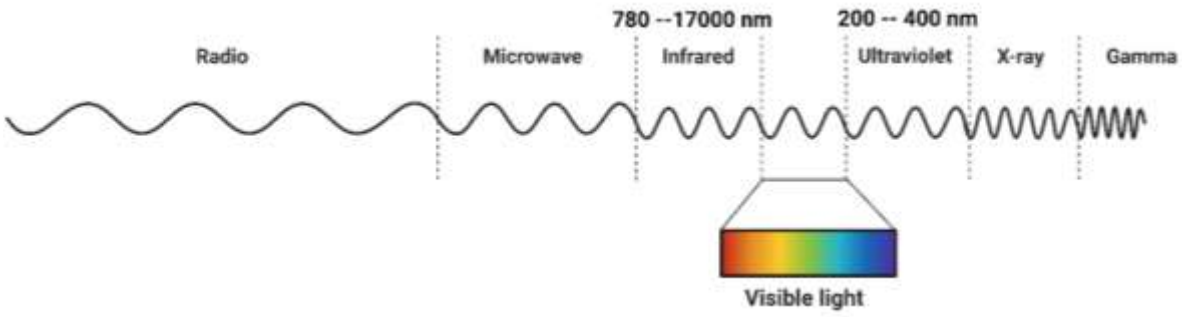

Figure 1.1: Electromagnetic spectrum of light (This image has been created by using Biorender).

1.1.1 UV rays

The UV radiation, the source of ionizing radiation of electromagnetic radiation. It is divided into three different ranges UVA (320-400 nm), UVB (280-320 nm) and UVC (<280 nm). UV radiation is important for normal physiology, mediating, cell growth and differentiation, for production of vitamin D [3].

1.1.2 Visible light

The visible light spectrum is used for therapeutic modality. It has effectiveness during *in-vitro* cell and tissue culturing, act as antioxidant for post thawing human stem cells, reduce appearance of aging, soft tissue handling, reduce pain and inflammation and act as an alternate of cancer therapy [4].

1.1.3 Near infrared light

It is reported that Near-infrared (NIR) light (780-1700 nm) is “extensively used” in bioimaging and different medical procedures. Due to its unique physical properties, minimal tissue absorption with high tissue penetration, low tissue auto-fluorescence interference as compared to visible light, it is suitable for many medical procedures [5].

1.2 Electron transport chain and photoacceptors

Mitochondria is branded as powerhouse of the cell in 1957 by Peter Siekevitz. The electron transport chain (ETC), in the presence of O_2 drives the synthesis of ATP from ADP by the mechanism of chemiosmotic coupling [6],[7]. ATP production is dominant role of mitochondria, this is done by oxidizing by major products of cytosol that are glycolysis, pyruvate and NADH [8]. Mitochondrial ETC composed of multiprotein complexes I-IV [9]. To synthesise energy, cells for their metabolic processes utilize carbohydrates, fats, and proteins. The catabolism of glucose is processed via glycolysis and subsequent pyruvate oxidation, fatty acids are processed through fatty acid β-oxidation, and amino acids are processed through oxidative deamination and transamination [10]. From these processes, molecules are produced and used in tricarboxylic acid (TCA) cycle to produce substrates to In TCA cycle, NADH and $FADH_2$ are generated these donate electrons to ubiquinol (CoQ) at complex I or complex II. CoQ carries further electrons to complex III, it pumps protons to intermembrane space to cytochrome c for transport to complex IV, then these electrons are transferred to oxygen which is reduced to water as shown in Figure 1.2 [7].

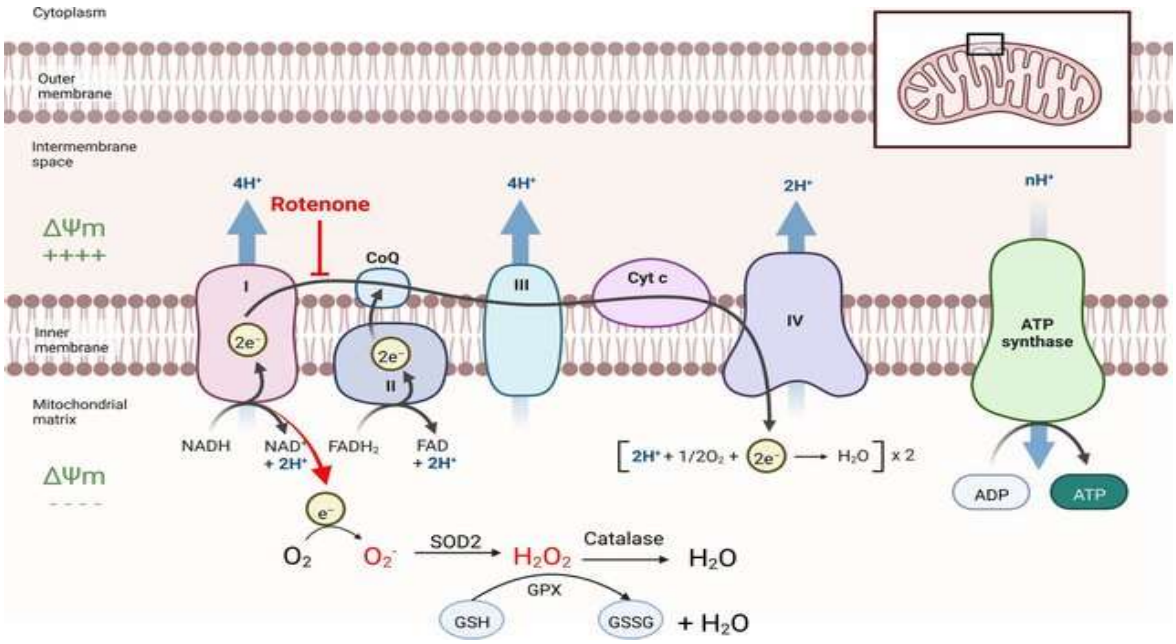

Figure 1.2 : Illustration of structure of the mitochondrial electron transport chain (ETC) along with Complex I, Complex II, Complex III, Complex IV and Complex V [11].

In response of electron transport, complexes I, III and IV pumped total ten protons into intermembrane space, acting in series with respect to electron flux in parallel with to the proton circuit. Their accumulation produces electrochemical proton gradient which is known as mitochondrial membrane potential (Δψ). Δψ generates proton-motive force (Δp) by combing with proton concentration (pH), Δψ is the dominant component Δp having value 150-180 mV of total of 200-220 mV of Δp [7], [12]. Δp is basic element during process of energy storage during mitochondrial oxidative phosphorylation (complexes I to IV) to ATP synthase (complex V), proton re-enter for dissipation of Δp [7]. Mitochondrial ETC is known as one of the major cellular generators of reactive oxygen species (ROS), this includes superoxide (O_2), hydrogen peroxide (H_2O_2) and the hydroxyl free radical [9]

1.2.1 Photoacceptors

The light interacting with biological system is absorbed by electronic absorption bands associated with photoacceptor or chromophore present in cells or tissues [13], [14]. List of the chromophores and fluorophores [15], [16] along with their associated excitation, emission, and absorption wavelength is shown in table 1.1

Table 1.1: List of chromophores and fluorophores.

List of chromophores and fluorophores	Excitation wavelength (nm)	Emission wavelength (nm)	Absorption wavelength (nm)	Ref.
Chromophores				
Protein			200-280	[17]
Haemoglobin			400, 546, 554, 581	[18]
Water			1400-12,800	[19]
Cytochrome C Oxidase			620-900	[20]
Fluorophores				
Lipofuscin	340-395	500-640		[15], [21]
Tryptophan	295	345		[16]
Collagen	330-340	400-410		[15], [22]
Elastin	350-420	420-510		[15], [22]
NADH	320-380	480		[23], [24]
FAD	420-480	520-580		[23], [24]
Porphyrins	390-450	635-690		[15]

1.2.1.1 Role of NADH and FAD in metabolic activities of cell

In cells and tissues, there exists a wide range of fluorophores. The most important fluorophores for monitoring the metabolic activity are Nicotinamide dinucleotide (NADH) and Flavin adenine dinucleotide (FAD) also play important roles in cellular oxidation reduction reaction. These are naturally fluorescent and allows non-invasive imaging of metabolic activities of live cells and tissues [25]. Biochemical, morphological, and metabolic information of cells and tissues are provided by optical imaging. NADH and FAD imaging are labelling free tool for study cell metabolism. The excitation wavelength of light for NADH is 335 nm to 365 nm while the emission peak is obtained around 440 nm to 490 nm. The excitation wavelength for FAD is 450 nm and maximum excitation peak is around 550 nm [26]. These fluorophores have different lifetime and spectral range due to their chemical structures. These metabolically active fluorophores NAD(P)H and FAD having protein bound and free structures. The difference between protein bound and free NAD(P)H and FAD is difference in fluorescence lifetime.

The lifetime attributed with NADH free is τ_{free} is 0.4 ns, for protein bound τ_{bound} is about 2.5 ns and for FAD+, τ_{free} is 2.3 ns and for FAD+ τ_{bound} is 0.3 ns [27]. Different techniques have been utilized for measuring the NADH and FAD that is helpful to investigate the metabolic activities of healthy and cancerous cells. There is difference between value of healthy and cancerous cells. Yu and Heikal have reported two photon fluorescence lifetime imaging of intracellular coenzyme NADH. The average value of NADH in both healthy and cancerous breast cells has been calculated. It's value in healthy cells is (99 ± 37 μM) and in cancerous cells is (168 ± 49 μM), that is approximately1.8 fold high in cancerous cells than the normal cells. Two photon fluorescence anisotropy imaging is used for obtaining the population fraction of free and enzyme bound NADH in both healthy and cancerous breast cells. The population fraction of free and enzyme bound NADH in healthy cells is (0.18 ± 0.08) and (0.82 ± 0.08) respectively while their value in cancerous cells is statistically different. Their value in cancerous cells is (0.25 ± 0.08) and (0.75 ± 0.08) for free and enzyme bound NADH respectively. These findings are then compared with the solution of free NADH mixing with malate dehydrogenase (mMDH) and lactate dehydrogenase (LDH). This study is useful for living cell physiology imaging and for sensing metabolic and signalling pathways [28], [29], [30], [31].

1.3 Light interaction with Mammalian cell

The biological response of the cell to the light is due to the physical and chemical changes in the photo acceptor molecules of the cells. The photons of light are absorbed by the electronic absorption bands of the photo acceptor or molecular chromophore and

fluorophores that in turns activates cellular metabolism. The interaction of light with biological samples depends upon laser wavelength, frequency, and wave number but the second important consideration is absorption spectrum of the photo acceptor molecules [32]. The most important part of the cell that is considered as the main site for the initial response of light is mitochondria. It is the cellular power plants and through the process of oxidative phosphorylation it produced energy in the form of ATP (adenosine triphosphate). The photon energy is absorbed by IV unit of the mitochondrial electron transport chain which is known as cytochrome c oxidase (CCO). This terminal enzyme leads to the activation of photo-signalling pathways and is responsible for the initiation a cascade of intracellular signals. The photon energy absorbed by the CCO causes in increase in ATP, ROS (reactive oxygen species), intracellular calcium and is responsible for stimulation of DNA and RNA synthesis. It is also assumed that due to reduction of CCO nitric oxide (NO) is also released and the activity of the CCO is inhibited by NO [8]. The most effective means to produce energy in the cell is electron transport chain. FAD and NADH are primary acceptor and donor of electrons produced during the electron transport chain. These are auto fluorescent and considered as the metabolic coenzymes and provide information about the cellular metabolic rate [33].

1.3.1 Light interaction with biological tissues

When light interacts with the biological tissues, then the following processes occurred reflection, elastic scattering (single and diffuse scattering), Raman scattering, absorption, and fluorescence. The biological tissues are optically inhomogeneous and multi-layered media. The light after the interaction with tissue reflect partially from multi-interface and remaining part of light is penetrated by the tissue. The impact of the laser light on the biological tissue depends on the parameters of laser light like wavelength, intensity, and time of exposure to the biological samples. When laser interacts with the biological samples (cells and tissues) then a wide range of phenomenon happened. The laser light has various impacts on the tissues according to their structures and due to the unique properties of laser light. The various effects of laser light are differentiated and classified according to the diagnostics and therapies. The most prominent types of effect are photodestructive effects.

1.3.1.1 Photodestructive effects

In this effect, hydrodynamic, photochemical, and thermal effects are dominant and can cause the destruction of tissues. In laser surgery, this effect may be prominent and can be observed. Light is absorbed by the biological tissues and is responsible for the excitation of atoms and molecules of the samples. Photochemical and photophysical reactions are dominant in this effect. In light tissue interactions, photothermal and photochemical effects

are induced in tissue samples only due to absorption. It is known that the radiation can interact with biological samples through photochemical effect. The absorption of light causes the changes in samples, but it depends on the wavelength of the interacted radiation and the absorption by the chromophores and fluorophores in samples. Nonperturbing impact: When the laser light interacts with the bio samples and has no changing in the properties of sample then it is specified as the nonperturbing effect of light. Penetration, reflection, and scattering are the examples of this effect. This type of laser interaction with bio tissue is applied for diagnostics purpose [34], [35].

1.4 Anatomy of human skin

Human skin is consisting of three layers called epidermis, the lower dermis, and the hypodermis as shown in Figure 1.3. The upper layer epidermis provides barrier function of the skin and mainly contain keratinocytes. At the innermost layer, they form a stratified epithelium with basal keratinocytes. These are in close association with melanocytes, that provides skin pigmentation. The lower layer of skin dermal contain multiple types of cells, one of the most important is fibroblasts that synthesise components of extracellular matrix (ECM) for cellular growth e.g., collagen, elastin is produced by them responsible for skin tensile strength and elasticity [36] [37]. Epidermis is separated from the dermis through dermal-epidermal junction. This junction is formed by basement membrane, both keratinocytes and fibroblasts in dermis contribute to the development of basement membrane. Dermis is organized into two layers, papillary and reticular dermis [37], [38]. Basement membrane composed of different proteins like laminin, nidogen, type I,III, IV, VII, and XVII collagens, proteoglycans and preclean, that separate the melanocytes and keratinocytes from papillary dermis [39].

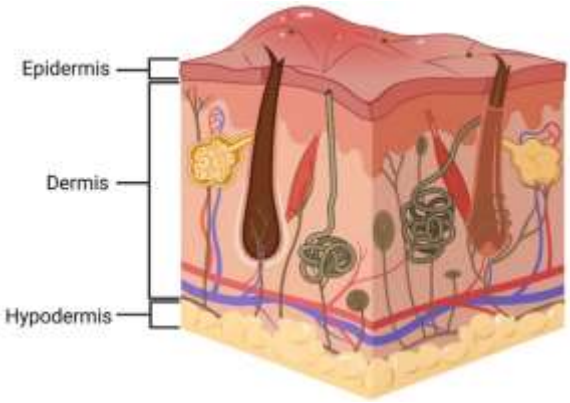

Figure 1.3: Anatomy of human skin (This image is generated by using Biorender).

1.4.1 Melanoma

Melanocytes are pigment producing cells in the skin and derived from neural crest, a group of highly migrated embryonic cells and reside in the basal layer of the epidermis. In melanocytes development many genes are involved those are also contributed to the development of an aggressive and fatal form of skin cancer called melanoma [40]. Melanocytes transformed and melanoma developed and begin to grow radially in skin this is early stage of a primary melanoma, where cancer cells are generally confined to the epidermis, it is called as the radial growth phase (RGP). When the radial growth phase leading to the invasion through basement membrane into dermis, it is known as vertical growth phase (VGP) [41]. The RGP phase developed via VGP and then press forward into highly aggressive phase called metastatic melanoma. RGP is confined in epidermis and is curable through surgical removal. VGP is an intermediate phase where cancer cells invaded vertically into dermis and in metastatic phase cancer cells moved into the blood stream [42].

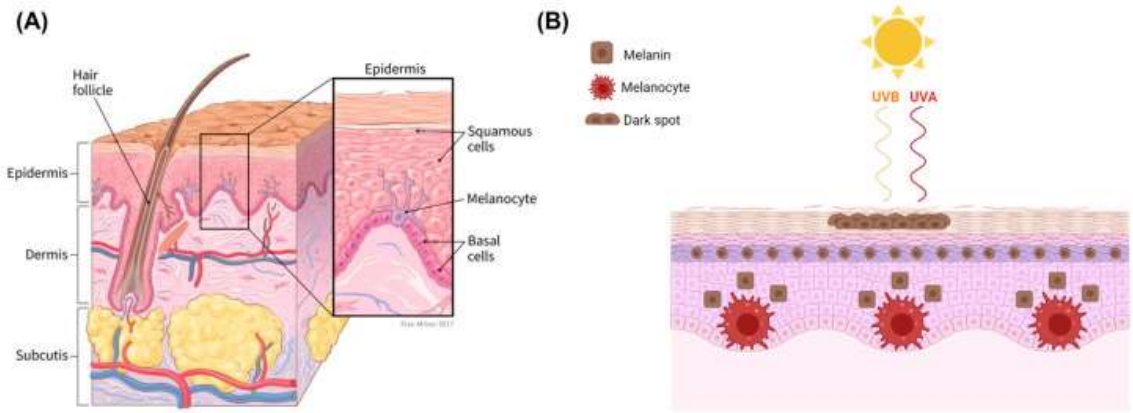

Figure 1.4: Structure of human skin with epidermis showing the melanocytes residing between squamous and basal cells. (B) The production of melanin due to UVA and UVB [43].

1.4.2 Melanoma cancer and Clark's level

One in every three diagnosed cancer is skin cancer and 5th most common cancer in UK [43]. Skin cancers are the most common diagnosed group of cancers among estimated 1.5 million new cases of cancer in 2020. During the last 50 years, the incidence of melanoma is increased annually by 4% to 6% in fair-skinned population in North America, Northern Europe, Australia, and New Zealand. During the last 50 years, it has been also increased in European ancestry. The increment in melanoma patients is due to increased exposure of population to UV radiations from sun or from artificial source.

The recent global estimation reveals newly diagnosed cases can be attributed to UV radiation [44], [45]. Overall skin cancer includes malignant melanoma and non-melanoma

skin cancer, the incidence of both types is on rise. But malignant melanoma is increasing 0.6% annually among adults [46]. In past, it was a rare cancer, but during last 50 years it is increasing faster compared to other cancer. Melanoma is a malignant tumour that arise from pigment producing cells called melanocytes (Figure 1.4) [47].

The overall incidence of melanoma and keratinocyte carcinoma (KC) is comprise of basal cell carcinoma (BCC) and squamous cell carcinoma (SCC) [45]. SCC and BCC are most common non-melanoma skin cancers, SCC has higher tendency to metastasize as compared to BCC [48]. Melanocytes are at the basal level of epidermis and are responsible for the production of melanin that is UV absorbing pigment. Two types of melanin is produced by melanocytes black or brown pigment eumelanin and red or yellow pigment pheomelanin [49]. Pheomelanin has weak shielding against UV radiations as compared to eumelanin and generate ROS due to UV radiations [50]. Melanoma is the deadliest form of skin cancer. In 1800s it was recognized as disease and in 1960s, it was classified on histological patterns by a dermatologist Wallace Clark [49].

1.4.2.1 Clark level

In 1969 Clark separated melanomas into superficial spreading, lentigo maligna and nodular, also defined level of invasion of melanoma from I to V from epidermis to subcutaneous fat as shown in Figure 1.5 [51].

- Level I: Malignant melanocytes are confined in the outer layer of skin (epidermis).
- Level II: Penetration of melanocytes in papillary dermis by single cell or nest of cells
- Level III: Few melanocytes may penetrate superficial reticular dermis, but growth is not permeative. This level usually implies to vertical growth phase of melanoma.
- Level IV: Melanocytes penetrate and spread in the reticular dermis.
- Level V: Melanocytes penetrate and grow in subcutaneous fat [52].

Clarks levels remained standardized way provide information related to risk of aggressiveness of melanoma but in 1970, Alexander Breslow introduced a more accurate method for classifying melanoma based on invasion depth of tumour. He divided melanoma into five different stages.

- Stage I: less than or equal to 0.75 mm
- Stage II: 0.76 to 1.5 mm
- Stage III: 1.51 mm to 2.25 mm
- Stage IV: 2.26 mm to 3.0 mm
- Stage V: greater than 3.0 mm

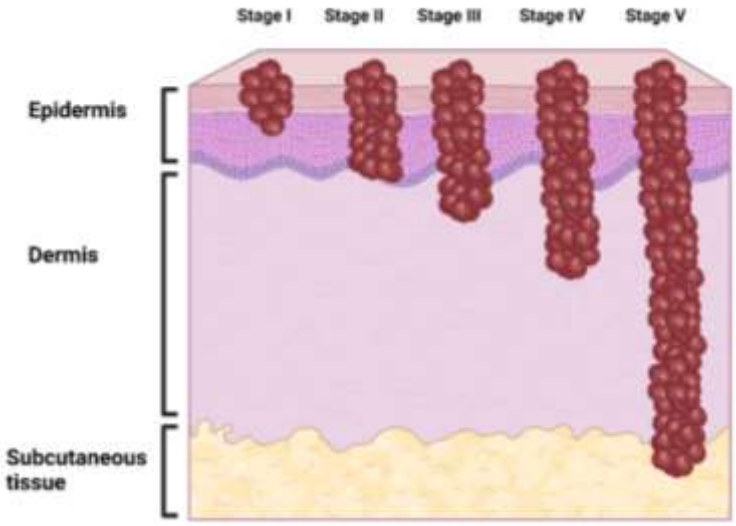

Figure 1.5: Invasion of melanoma in epidermis, dermis and subcutaneous tissue and level of melanoma cancer (This image is generated by using BioRender).

In 1980s, it became clear that Clark level and Breslow thickness resulted in variation for prediction and therapy. After 40 years, new and improved staging system TNM (tumour, node, metastasis) was introduced by American Joint Committee on Cancer (AJCC). The AJCC staging system provide guideline for detection stage of melanoma and most recent staging manual provide by AJCC in 2016 and implemented in 2018. For improvement of melanoma detection non-invasive imaging technology is more frequently used like fluorescence in situ hybridization, comparative genomic hybridization, sequencing, mass spectrometry [49].

1.5 Light penetration in human skin

Stratum corneum is the outer most section of human skin having thickness 0.01-0.02 mm and epidermis having thickness 0.027-0.15 mm. The dermis has thickness between 0.6-3 mm. Epidermis and dermis can propagate and absorb light; absorption of light in epidermis is due to natural pigment chromophore and melanin [53]. Laser light interact with tissues in four different ways reflection, scattering, transmission, and absorption. In skin absorption is the most important effect of laser light, absorbed by primary endogenous chromophores water, melanin and haemoglobin [2]. The interaction of light with human skin is presented in Figure 1.6.

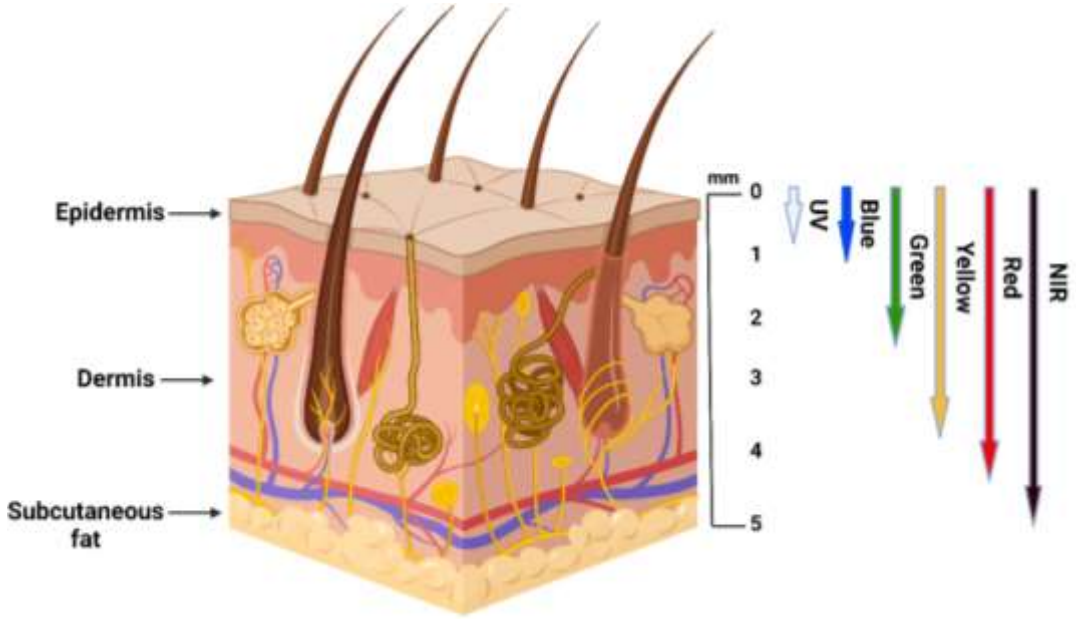

Figure 1.6: Representative image of skin with different layers penetration by different wavelengths of light [2], [54]. (This image is generated by using Biorender).

1.6 Cell culturing

Cell Culturing: In 1970, Harrison introduced first cell culture of nerve fibres during his research. From living organisms, primary cultures are isolated. These primary cultures having populations of different types of cells that are present in source tissues. These cells are carried out under some conditions ten according to situation these cells are attached to glass or dish or in the form of suspension. The most common type of cell culturing model is 2D model and 3D model [55].

1.6.1 2D cell culturing

To study biochemically and biophysically of cellular response, 2D cell cultures are used as in vitro models. Under some specific situations and conditions these models provide information about cell behaviour, growth, migration and cell differentiation and in vivo response. In conventional 2D culturing, cells grow in a culture flask or in a flat petri dish as monolayer. The monolayer of cells is helpful for obtain the equal nutrients from growth media. This leads to homogenous growth of cell layer in flask or petri dish. That's why 2D models of cells are more helpful and convenient for clinical use and studying for researchers. But some important characteristics cannot be studied in 2D culturing, to overcome this problem 3D culturing is an advanced technique to study necessary and specific features of cells [55].

1.6.2 3D culturing

3D culturing was introduced by Hamburg and Salmon in 1970. In conventional 2D culture models, tissue organization and cell differentiation are not possible to understand therefore to overcome these difficulties 3D cell culturing models have great attention. To understand the structure, pathophysiology, and function of organs, it is necessary to understand that how the cells and tissues are working as a part of the organ. To overcome all the limitations and for a better understanding of functions of tissues 3D model provides a convenient way as compared to 2D models. 3D models are a better approach for new treatments and for searching new biomarkers. 3D models are divided into three categories, suspension cultures, cultures in gel like substances or in concentrated medium, culture in scaffold [56]. The transition from 2D to 3D is an important step for developing biomimetic tissue models [57].

1.7 *In-vitro* 3D biological models

3D culture is an emerging and versatile system that can be utilize for various applications like disease modelling, drug target identification. Depending on the type of application, 3D cellular models are as simple as spheroids and complex like 3D bio-printed structures [58]. In 3D culturing, cells are grown in 3D environment closely mimicking the natural environment for development of 3D biological models. 3D models are developed by two different techniques i) scaffold-free 3D models and ii) scaffolds-based 3D models [59].

1.7.1. Scaffold-free 3D biological models

In tissue engineering (TE), scaffold-free method is bottom-up approach for developing 3D structures without any use of artificial scaffolds. The examples of 3D scaffold-free structures are spheroids, organoids. These structures are formed using single cell suspension, spheroids, tissue strands, and cell sheets [59].

1.7.2. Scaffold-based 3D biological models

In TE and regenerative medicines, scaffolds-based approaches are very prominent. These structures can be used for restoration of different types of lost or damaged tissues like bone regeneration, repairing of cartilage, skin formation. These provide temporary structure for uniform distribution of cells, growth of cells, and mimicking extra cellular matrix (ECM). Scaffolds have different designs including mesh, fibre, sponges according to the needs of developing tissues [59], [60].

1.7.2.1. Scaffold types and fabrication methods

In 1993, introduction the concept of 3D scaffolds was significant milestone in field of TE [61]. Scaffolds with different designs and from various biomaterials have been reported. It includes mechanical, biological, and physicochemical compatibility for replacing damaged tissues. The architecture of scaffold should be designed to provide enough porous structure for migration of nutrients. Scaffolds should provide support for attachment, growth, and differentiation of cells in host tissues. To facilitate and regulate the activities of replaced tissues, scaffolds interact with cellular components therefore it is necessary biomaterials of scaffolds should be compatible with biomolecules. The mechanical properties of the scaffold's biomaterial should match with the defective tissue properties to provide shape, stability, and mechanical strength to the replaced tissue [62].

The structural properties of scaffolds are crucial in regulation of cellular response like cell adherence, differentiation, and proliferation. There are three major cues for the fabrication of scaffolds porosity, grain size, and surface topography provide support for cells differentiation, proliferation, and cellular response [63]. There is wide range of scaffolds based on their geometry and source material for maintenance and reconstruction of tissue functions for example porous, hydrogel, fibrous, microsphere, metal and composite scaffolds are very pronounced as shown in Figure 1.7 [64], [65]. Table 1.2 represents types and applications of scaffolds in TE.

Table 1.2: Scaffold types and applications in TE.

Scaffold Type	Fabrication material	Applications	Reference
Porous scaffolds	CaP, bioceramic material	Bone regrowth, ECM deposition, Vascularization	[65], [66], [67]
Fibrous scaffolds	Biodegradable polymers like PCL, gelatin, cellulose, silk fibron	Skin, bone, muscle, vein, cartilage, nerve and skin tissue regeneration, wound healing, vascular grafts	[65], [68]
Hydrogel scaffolds	Hydrophilic polymer chains, synthetic materials, naturally derived polymers	Serve as ECM, space filling agent, bioactive molecule, and cell/tissue delivery	[65], [69]
Decellularized scaffolds	Tissues/organs (Remove cellular components from tissues to produce ECM)	Cardiac valves, lungs, renal bladder, blood vessels regeneration, regenerative medicines	[65], [70], [71]
Polymer scaffolds	Acrylic polymers, biopolymers, sodium alginate, HAP,	Renovation of traumatized tissues, bone regeneration	[65], [72]
Nanoparticle scaffolds	Polymeric, inorganic, lipid, and metal-based nanoparticle,	Stabilizing and enhancing cell adhesion, antibacterial activity without cytotoxicity forms embryonic stem cells	[73]

1.7.2.2. Scaffold fabrication technologies

For 3D scaffold fabrication, there are variety of conventional methods i.e., thermally induced phase separation, emulsion freeze-drying, solvent casting, gas foaming, fibre binding, membrane lamination modelling, and electrospinning. But these conventional scaffold fabrication techniques are not convenient for precise pore size, geometry, and interconnectivity of scaffold [61], [74]. These methods are not adequate due to lack of control porosity, architecture, and cellular attraction for complex structures production. 3D bioprinting is state-of-the-art technology for the fabrication of TE scaffolds and based on an on-demand 3D model. 3D scaffolds with micrometre scale resolution to mimic microarchitecture of tissues are designed by CAD and then sent to printer for printing [75].

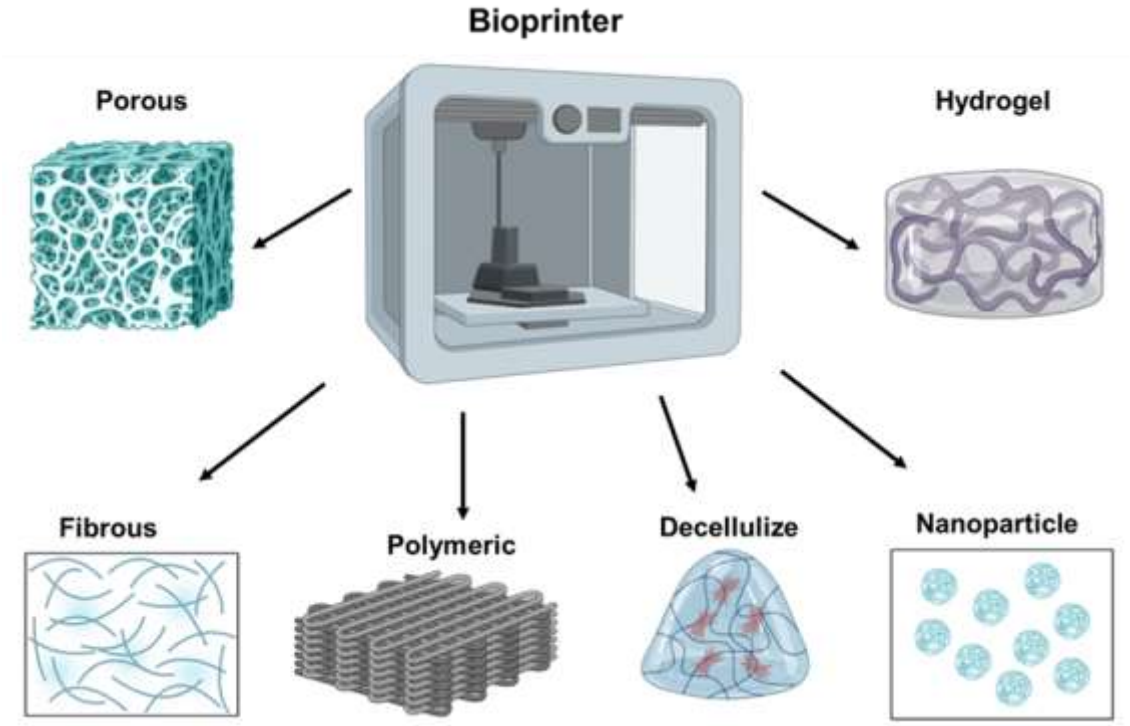

Figure 1.7: Classification of printed scaffolds used in TE according to the geometry. (This image was created using Biorender).

1.8 Types of printing technology

1.8.1 3D bioprinting techniques categories

For fabricating complex biological constructs in the field of regenerative medicines and TE, 3D bioprinting has emerged as new technique. First 3D printer was built in 1980s by an American engineer, Charles Hull for creating solid objects. Later, during 1990s3D printing had appeared in different fields of healthcare.

3D bioprinting involves printing of material called bioink contained living cells, biomaterials, and active biomolecules for layer-by-layer deposition of bioink on substrate for generating 3D structures like tissues and organs. 3D bioprinting techniques can be divided into following categories as shown in Figure 1.8 [76] [77]. Figure 1.9 shows the schematic representation of division of bioprinting technologies.

- Inkjet-based 3D bioprinting
- Laser-assisted 3D bioprinting
- Extrusion-based 3D bioprinting
- Stereolithography 3D bioprinting
- Digital light processing (DLP) bioprinting
- Two-photon polymerization (2PP)

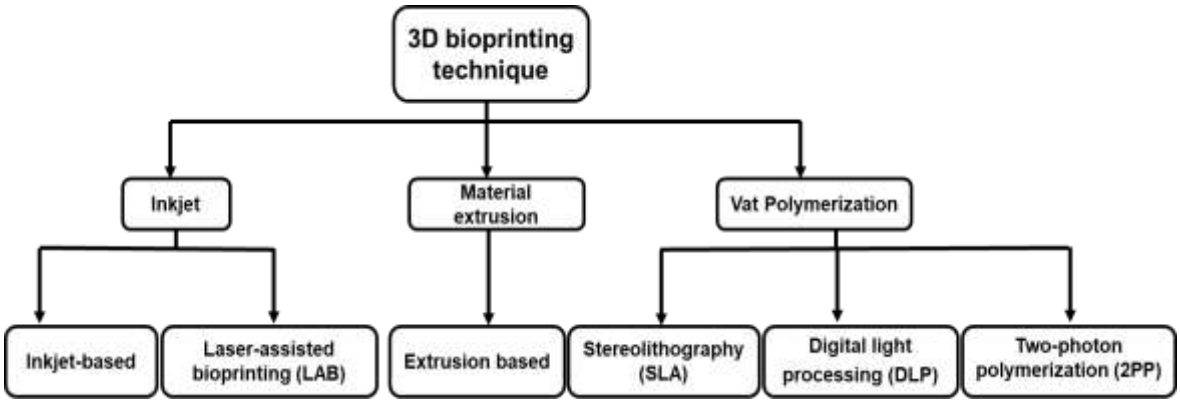

Figure 1.8: 3D based bioprinting technologies for fabrication of scaffolds.

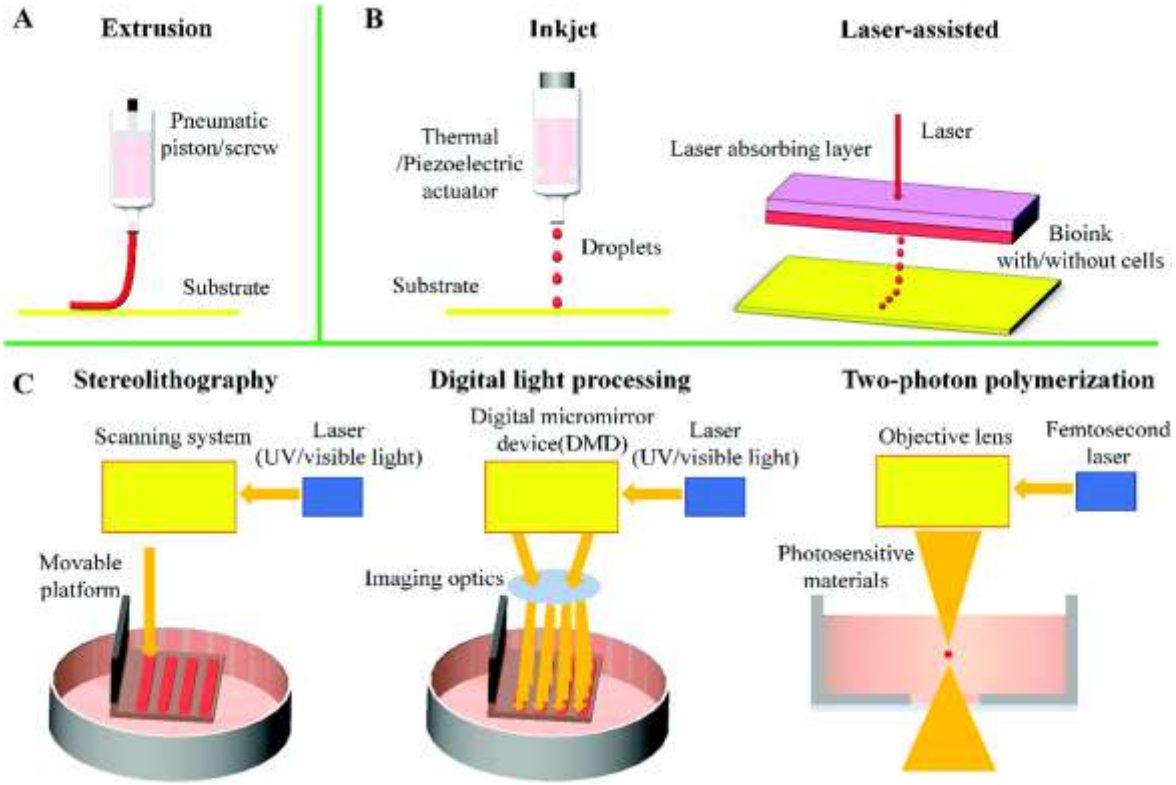

Figure 1.9: Schematic representation of 3D bioprinting technologies A) Extrusion-based B) Material extrusion: Inkjet based and Laser- assisted bioprinting C) Vat polymerization: Stereolithography (SLA), Digital Light Processing (DLP), and Two-photon polymerization (2PP) [77].

1.8.1.1 Inkjet-based 3D bioprinting

In 2003, first bioprinting technology known as Inkjet bioprinting was introduced like conventional 2D ink-jet printer. This is non-contacting bioprinting process deliver a precise and control amount of bioink on substrate controlled by computer. According to the requirements of printing, there are two strategies of ink used in bioprinting 1) continuous inkjet printing (CIJ) and 2) drop on demand printing (DOD). Usually, 103-104 cells contained by each droplet having diameter range between 10 to 150μm.

Biological solution comprised of cell-laden, stores in the ink cartridge and elevator stage is controlled electronically in Z-axis. Printer head is operated for generating droplets of ink on substrate and its function is similar as thermal or piezoelectric actuator [78], [79]. As inkjet bioprinting has high resolution up to 50μm and good survival rate. Multiple cell types can be positioned accurately with this procedure. For further advancements, this printing technique might need to be integrated with other printing methods due to constraints of restricted viscosities and vertical printing [80].

1.8.1.2. Laser-assisted 3D bioprinting

Laser-assisted bioprinting (LAB) is a headless inkjet method of printing, provide information that how laser technology is interacting with bioink. LAB technology, a layer of bioink is coated on the absorption layer on a transparent glass plate to produce a three-layer structure. A pulse laser is focused on absorption layer and small part of bioink irradiated, vaporized, and expanded. This laser printing technology is similar to LIFT [81]. For generating high resolution pattern, LIFT is becoming more ideal for transferring biological materials on the receiving substrate [82]. Numerous research has shown that LAB can precisely position different cell types, and one study even showed that it can put a single cell per droplet. But it is costly procedure with limited scalability and stability. It has demonstrated significant potential when paired with biofabrication techniques [80].

1.8.1.3. Extrusion-based 3D bioprinting

The most widely used method for 3D structures is extrusion based bioprinting. Viscose cell laden extrusion through a dosing needle is the foundation of 3D extrusion bioprinting process. Based on the CAD model, the needle location is numerically controlled like traditional 3D printing. The 3D structures are constructed layer by layer. By adopting specific nozzles with multi compartments, extrusion based bioprinters can be used to manufacture 3D structures multi-walled and core-sheath fibres. For high-precision production, bioinks must be designed with shear thinning or fast solidification properties [83]. Extrusion based

bioprinting is very versatile and feasible for vertical printing, but it has relatively low resolution that prevents cells positioning and necessities use of advanced hydrogel bioink that prevents both mechanical integrity and cell viability. This has led to the development and application of self-healing hydrogels and interpenetrating polymer networks [80].

1.8.1.4. Stereolithography 3D bioprinting

SLA is a conventional vat-polymerization (VP) process, most common printing technology for fabrication of 3D constructs. The working mechanism of SLA depends upon computer-controlled laser beam to cure photocross-linking of liquid bioink. After finishing whole printing process, additional photocuring like heating is required for extra post-polymerization [84]. It can create patterns with high resolution by using light to crosslink with photosensitive resin. SLA bioprinting is high speed and high-resolution technique but it used UV or near-UV for promote chemical reactions that is damaging for cells. To overcome this problem in 1987 by Larry J. Hornbeck, Digital Light Processing (DLP) is introduced where optimization of wavelength and curing time is achieved by introducing a series of digital micromirror devices or DMDs [72].

1.8.1.5. Digital light processing (DLP) bioprinting

DLP is an additive manufacturing technology that prints photopolymer by using a projected light ultraviolet(UV) light, blue light, near-infrared (NIR) light and other visible light to cure each layer of the product simultaneously and produce a solid 3D objects with high resolution and structural complexity [85], [86]. Like SLA, it is also another type of VP printing, but DLP based on 2D photopolymerization using DMD liquid crystal display (LCD) projection system [84]. It provided 3D product with even cell distribution due to photopolymerization and rapid printing speed [87]. It can produce layer of material with high resolution up to 50μm. Due to combination of advantages of high layer resolution and robust mechanical properties make it suitable and reliable for multi-material industrial applications [88].

1.8.1.6. Two-photon polymerization (2PP)

2PP is based on non-linear optical phenomenon and known as direct laser writing, femtosecond laser writing, dip-in laser lithography multiphoton SLA [89]. Like SLA and DLP, 2PP is another vat polymerization-based printing technology however it offers more control and better print quality. It is liquid-base prototyping method that used high power near-infrared (NIR) femtosecond (Fs) laser pulses[90]; the photo initiator simultaneously absorbs two photons. When laser pulses focused into the material, one of the photoinitiator (PI) molecule absorb two photons for the initiation of free-radical polymerization within focus volume [91]. The absorption of two photons dependent upon the intensity of incident light

[90]. In 2014, it was reported the first 3D hydrogel structure contained live cells was construct using 2PP technique [83]. Assessment between different types of 3D printing technologies, features, advantages and disadvantages are presented in table 1.3 and 1.4.

Table 1.3: A comparison between different printing technologies.

Printer Type	**Printing speed**	**Cell viability**	**Cost**	**Resolution (µm)**	**Reference**
Inkjet	Fast	>85%	Low	50	[92], [93]
Laser assisted	Medium	>95%	High	~ 1	[92], [93]
Extrusion based	Slow	40-80%	Medium	>100	[92],[93],[84]
SLA	Fast	>85%	Low	10	[61],[77],[84]
DLP	Faster	>85%	High	6	[77], [92]
2PP	Fast	>85%	High	≤1	[77],[94],[95]

Table 1.4: Summary of advantages and disadvantages of different printing technologies.

Technology	Printing Method	Advantages	Disadvantages	Ref.
Inkjet	Continuous manner, drop-on-demand (DOD) style.	Cheap and non-contact nature, low cost, easy accessibility, having capability to print multiple bioinks at same time.	Due to high cell density nozzle clogging, thermal and mechanical stress during droplet formation.	[93], [96], [97]
Laser assisted	High-energy laser pulse for direct writing.	Nozzle free and non-contact printing, High viability of cells.	Time consuming, due to nature of ribbon difficult to position cell.	[96], [97], [98]
Extrusion based	Direct ink writing (DIW) or pressure-assisted.	Deposition of high density of cells, broad range of material selection.	Shear stress occurrence in cells, effect on cell viability.	[96], [97], [98]
SLA	Projecting light on photo-sensitive heat curable bioink in plane-by-plane manner.	Fast rate of parts building, less complicated, smooth surface creation.	Limited material for printing, layer thickness depends upon exposure time and UV sources.	[93], [96], [98], [99]
DLP	Fresh photopolymer liquid film is cured by using conventional light source.	Living cells safety under UV exposure, high resolution about 1μm.	Photoinitiator does not split efficiently under UV light, limited selection of photoinitiator.	[83], [99]
2PP	Two femtosecond laser beams are focused on photopolymerizable liquid for fabrication of highly resolution parts.	Extremely high resolution to nano level up to 0.15μm, compatible for living cells and biological molecules.	Not suitable for medication with antioxidant properties, loss of drug loading and imprecise dose because of post curing steps.	[99], [100]

1.9 Commonly used Bioinks

For 3D bioprinting, biomaterials, cells, and supporting factors are important components these play significant role in terms of construction of living artificial tissues and organs. Selection of biomaterials play a very crucial role for designing tissues and are selected according to the specific physical and chemical characteristics for mimicking native ECM. Naturally driven biomaterials are considered because of their properties like the body's own ECM. These are main two types of biomaterials first natural sources for example gelatine, fibrin, collagen, silk protein, alginate and second synthetic like polylactic acid (PLA), polylactic-glycolic acid (PLGA) and PEGDA [77], [101]. Biomaterials in the form of solution or hydrogel loaded with required cell types are known as bioinks. For developing functional tissues and organ constructs, bioinks are necessary for bioprinting and selected according to the bioprinting technique. Cells can be encapsulated in bioinks for creating tissue structures [79]. In 3D bioprinting, bioink optimization e.g., material with high resolution, high-rate viability of cells, creation of appropriate cellular microenvironment for mimicking real biological tissue are the main concerns [83]. Mostly the materials used for bioprinting are hydrogels, light cross-linkable resins, composites, and polymers. In general, more comprehensive reviews are available for hydrogels and composites [102].

1.9.1 Hydrogel

Hydrogels are three dimensional networks composed of hydrophilic polymer chains bonded through covalent or non-covalent bond. They are highly porous and can have ability to capture a large amount of water mimicking the hydrate environment like real biological tissues that's the reason these are ideal for cell culturing and cell encapsulation. These are used in cell scaffolds, cartilage healing, bone regeneration, drug delivery, encapsulation of cancer cells. Hydrogel scaffolds can be fabricated by using gas foaming, photo lithography, electrospinning, 3D printing [103], [104].

1.9.2. Collagen

Collagen based scaffolds are 3D constructs composed of fibrous structural protein found in connective tissues. These are beneficial for cell growth, maintenance of tissue function and architecture. Due their excellent biocompatibility, these are broadly used in nerve, cartilage, bone, skin substitutes, and vascular grafts. It is also reported that use of collagen-based scaffolds in cancer research for spheroids formation increase the viability of cells [103], [105]. It is reported in cancer research collagen-based 3D *in-vitro* culture models can be fabricate by using various biofabrication techniques like freeze-dying, electro spinning and 3D bioprinting [106].

1.9.3. Resins

Resins are usually used as biomaterial ink for SLA, DLP and 2PP techniques, these can be crosslinked with light. The most important feature is the ability of resins to create 3D constructs adjacently for biofabrication. GelMA, PEG, PEG methacrylate (PEGMA), methacrylate poly (vinyl alcohol) (PVA-MA), DClear are most used resins for different applications in TE [102], [107], [108].

1.9.4. Composites

It comprised of blends of a polymeric matrix with specific reinforcements for adding mechanical strength or chemical identity of that particular matter [102]. These composites have abilities to develop complex structures with low cost and additional advantages. Alumina (Al), hydroxyapatite (HAp), calcium silicate bioceramics, ß-tricalcium phosphate (ß–TCP) are some reported examples of composites [85].

1.10 Examples of scaffolds-based 3D biological models

Some examples of *in vitro* developed scaffold-based 3D biological models have been discussed below.

1.10.1 Full thickness skin equivalent (FSE)

In past 25 years, great efforts are made to develop high biomimetic substitutes of the human skin. These are developed by employing tissue engineering approaches that are used for clinical applications, pharmaceutical research, healing of wounds [109]. In cosmetics, pharmacological and toxicological sciences there is also high demand in replacing animal testing with alternative methods. *In vitro* 3D human skin equivalents (SEs) constructed from human cell lines are state-of-the-art as an alternate of human skin [110]. Artificially reconstructed skin equivalents are substitutes of skin composed of epidermis and dermis layers [111]. In traditional skin constructs, dermal fibroblasts, melanocytes, and keratinocytes are major cell types. 3D skin manufacturing technology is divided into two types of scaffolds based and scaffold free.

Organotypic 3D skin culture and transwell/Boyden chamber approach are traditional scaffold-free methods. Scaffold based method is 3D bioprinting approach, by using this method multi-functional human skin model can be build [112]. In scaffold-free method, without any use of synthetic material skin equivalents are constructed from cultured fibroblasts and keratinocytes [111]. In this type of culture, dermal equivalent was composed of fibroblasts sheets those were cultured with ascorbic acid for 35 days to form a thick fibrous sheet. Keratinocytes were seeded on this fibroblasts sheet to form a stratified and

confined epidermis [113]. With the help of computer-controlled 3D bioprinter technique, tissues and organs are fabricated by using live cells, biological materials and biochemicals. The main three types of bioprinter technology are inkjet-based, microextrusion based and laser assisted printing. These technologies are using for production of multi-layered skin [111]. Kim et al. presented a new 3D cell printing strategy for 3D human skin model. A hybrid 3D bioprinting system has been developed in which extrusion-based and inkjet-based techniques are combined. By using the extrusion-dispensing module, collagen-based construct with polycaprolactone (PCL) mesh was fabricated and inkjet-based dispensing module was used for uniform distribution of keratinocytes. By using these features together, human skin is fabricated with functional transwell. The transwell system and dermal layer are fabricated by using extrusion printer while epidermis was constructed by inkjet module [114].

1.10.2 Melanoma full thickness skin equivalent (Melanoma-FSE)

To understand and characterize the interaction between melanoma and skin cell layers 2D and 3D models are established. 2D models are considered simple as compared to 3D models [115]. To understand therapeutic strategies against melanoma, experimental models are required to replicate the *in-vitro* human disease system. There are different 3D cell culture models that are cultured with different techniques for basic clinical cancer research. Organoids and spheroids are example of 3D models [116]. Spheroids are aggregate of cells that are embedded in collagen I, melanoma cells from spheroids do not invade much into collagen and present phenotype of radial growth phase [115]. These are *in-vitro* 3D model able of self- propagating. These models first expanded from embryonic stem cells, differentiated, and finally achieve fully structure for investigation. These models provide strength of using cellular material and a better replicate of melanoma in human patients [115], [116]. For early-stage investigation of human melanoma, full thickness skin equivalents with incorporation of melanoma cells have been developed in vitro. These skin constructs are valuable tool for investigation of melanoma migration, tumour-stroma interaction, an alternative to animal testing, melanoma invasion from epidermis to dermis [117], [118].

1.11 Thesis Structure

The main body of this thesis is composed to six chapter, each covering the following contents.

Chapter 1 provides literature review and an overview of light, the structure of cell, interaction of light with cells and tissue, anatomy of human skin and melanoma skin, 2D and 3D cell culturing, 3D printing technology, and the development of 3D artificial tissues.

Chapter 2 is about optical approaches for diagnostics and introduces the multi-mode optical system. In this chapter, different optical approaches have been discussed for the purpose of therapeutic applications, including Photo dynamic therapy (PDT), Photobiomodulation (PBM) and therapeutic effects of photosensitiser-free 1267nm light on cells.

Chapter 3 deals with the methodology employed throughout experimental work. It includes 2D and 3D cell culturing methods, assessment of singlet oxygen generation, cell viability analysis after laser interaction, and data analysis.

Chapter 4 presents the validation of our dual-mode device for the purpose of detection of healthy and non-healthy cells and tissues. It also about the development of 3D artificial tissue by using 3D bio-printed scaffolds. This work has been published in Biomedical Optics Express titled “Dual-mode OCT/fluorescence system for monitoring the morphology and metabolism of laser-printed 3D full-thickness skin equivalents”.

Chapter 5 is about examine the therapeutic effects of laser wavelength 1267 nm on 2D melanoma and non-melanoma models. It’s focuses on the treatment of melanoma using photosensitiser-free (PS-free) 1267 nm laser, production of singlet oxygen, and its effects on both healthy and non-healthy cells.

Chapter 6 is finally about summarizing the key findings and outlining future work for the advancing of this research. This is about the development of cancerous 3D artificial skin models and potential applications of 1267nm laser wavelength for the treatment of cancer.

Chapter 2

Optical approaches for diagnostics and therapy

Optical methods are applied for the real time and in vivo diagnosis of the cancerous cells and tissues. In diagnosis, many problems can be resolves by using non-invasive optical approaches. New optical imaging methods and spectroscopic techniques are introduced for the purpose of diagnosis. For variety of applications, optical approaches are more reliable as compared to the ordinary methods and techniques. Some of them are optical coherence tomography (OCT), THz imaging, fluorescence lifetime imaging, tissue oximetry, Raman scattering, laser doppler flowmetry (LDF), Fluorescence spectroscopy [34].

After the interaction of light with biological samples, light can be absorbed, reflected, reemitted, scattered. ATR (attenuated total reflection) or photoacoustic techniques are utilized for measuring the absorbed light. Diffuse reflectance spectroscopy, OCT, and confocal microscopy can be used for measuring reflected light. Fluorescence excitation spectroscopy, two-photon microscopy, or confocal microscopy can be utilized for measuring re-emitted light. Raman spectroscopy or scattering spectroscopy can be used for measuring scattered light [13].

2.1 Fluorescence spectroscopy

FS is type of electromagnetic spectroscopy for analysing fluorescence form samples by exciting using beam of light [119]. FS is an emerging analytical method that uses the evaluation of endogenous fluorophores from tissues and biological fluids like enzymes, amino acids, vitamins, porphyrins for disease diagnosis. It is used to observe the bio-chemical properties. FS device is used to monitor the metabolism of cells and tissues. under laser radiation in the UV or visible range of the spectrum, it is used to study the difference between intensity of spectral composition and fluorescence from healthy and cancerous tissues.

It relies on light of specific wavelength being delivered to the tissues. When this light is absorbed, it may excite endogenous molecules known as fluorophores which then reemit the light as fluorescence at the longer wavelength. The remitted light is then detected and sent to the spectrometer. The reemitted fluorescence is combination of wavelength and time resolve data [120].

Early diagnosis and variation in biochemistry of the tissues can be detected with fluorescence spectroscopic techniques. Fluorescence peaks corresponding to major

fluorophores is utilized for monitoring biochemical changes in tissues. These fluorophores include NADH, FAD, collagen, porphyrins, phospholipids [121]. NADH and FAD are two most important endogenous fluorophores for purpose of diagnostics for monitoring metabolic changes in cells and tissues [29]. Fluorescence absorption for NADH and FAD is 340nm and 450nm, while emission is about 458nm and 560nm respectively. Spectroscopic analysis reveals for both NAD+ and NADH absorption peak is about 260nm and 340 nm in UV range, while emission is detected at 440 to 465nm [25], [122]. The fluorescence diagnosis is based on the difference in spectral characteristics between normal and precancerous tissues.

2.2 Fluorescence Microscopy

To monitor cell physiology, fluorescence microscopy is major tool. The process of fluorescence involves absorption of light energy in the form of photon by an indicator and a few second later followed by emission of this light energy in the form of another photon. Its goal is to separate emitted light from excitation light by using optical filters. The underlying process of fluorescence involves the absorption of light energy (a photon) by an indicator followed by the emission of some of this light energy (as another photon) a few nanoseconds later. Because some energy is lost in this process, the emitted photon has less energy than the absorbed photon. Light with a short wavelength (toward the blue) has higher energy than light with a long wavelength (toward the red). Therefore, light emitted from an indicator usually has a longer wavelength than that of the absorbed (excitation) light. This change is called the Stokes shift [123]. For biological research and clinical studies, fluorescence imaging is a very powerful tool as it has ability to visualize and quantify biological processes [124].

2.3 Optical coherence tomography (OCT)

In the early 1990s, OCT was originated and employed for various medical applications like medical diagnosis and commercial systems as well. The working principle of OCT is same as the working principle of ultrasound imaging. The major difference between these two techniques is that in its probing mechanism it used light instead of sound[125].

OCT is based on the principle of interferometry, light wave splits into a reference beam with variable path length and a probe beam, that is focused on the sample. The backscattered light after interaction with inhomogeneities within the sample is recombined with the light reflected from the reference arm. An interference signal is generated only, if the path difference of both arms is smaller than the coherence length of the light source then [126]. Schematic image of OCT system is shown in Figure 2.1.

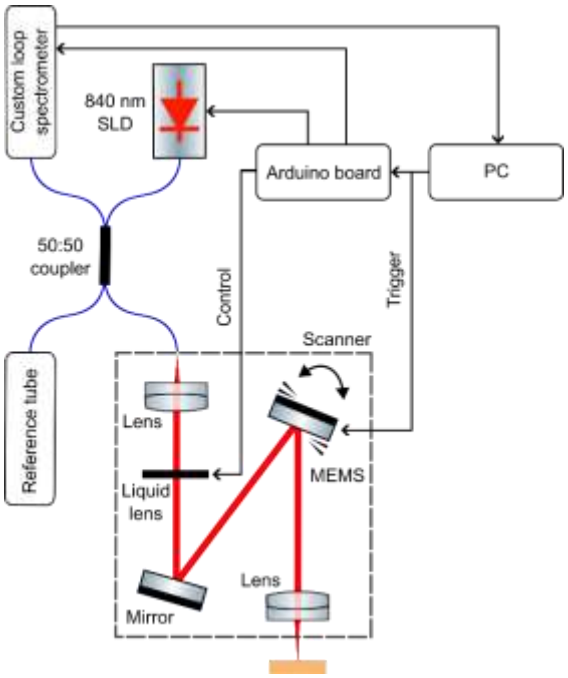

Figure 2.1: Schematic image of OCT imaging system.

This technique provides cross-sectional image of biological tissues with penetration depth 1mm to 3mm. It used low-coherence interferometry to identify regions of samples through highly backscattered signals. The image formed by OCT depend on the backscattered photons form various depths and sites from biological tissues. These backscattered photos are classified into singly reflected ballistic photons and multiple scattered photons [127].

As OCT allows non-invasive, non-contact cross-sectional imaging technique and non-invasive optical biopsies of the biological tissues. It allows the structure of skin like stratum corneum, sweat glands and junction between epidermis and dermis [126], [128]. For investigation of biochemical mechanism of skin, cultured skin equivalents (SEs) are widely used. To analyse the spatial distribution of skin mechanical properties elastography using tomographic methods such as ultrasound imaging or OCT is used [129].

2.4 Multi-modal optical systems

Multimodal molecular imaging an innovative way that combines two or more imaging technologies for attaining comprehensive real time information regarding to diagnosis and treating various diseases [130].

Table 2.1: Some examples of multimode optical imaging system.

System	Modalities	Applications	Ref.
Optical Coherence Tomography (OCT) + Fluorescence Molecular Imaging (FMI)	Combine OCT and FMI imaging system	Imaging of tissue morphology, visualization of basic molecular information at high resolution over 2-3 mm field of view	[131]
Fourier transform infrared spectra (FTIR) + Raman Spectroscopy	Combine FT-IR and Raman spectroscopy	Label-free and non-invasive in vitro studies of body fluids and cells, examine of ex-vivo tissues and biopsies	[132]
Photoacoustic + Ultrasound imaging	Combined optical and ultrasound imaging	Structural and functional information, quantitative analysis of different components within biological tissues	[133]
3D Quantitative phase imaging (QPI) + Fluorescence microscopy	Combined fluorescence and optical imaging system	Study of infectious disease, visualization of morphology and dynamics of living cells and parasites	[134]

2.5 Optical approaches for treatment (therapies)

After the diagnosis, different therapies are utilized for the treatment according to the situation and condition of disease. Many conventional methods are also utilized for the purpose of treatment. Some non-invasive optical treatment like photodynamic therapy and photobiomodulation are very promising treatment. Photodynamic therapy is a clinical therapy in which light combines with photo sensitizer and oxygen to generate reactive oxygen species (ROS) that is one of the main factors for clinical applications of PDT.

Photobiomodulation (PBM) is kind of phototherapy that used light source in the region of red to near infrared range but without any photosensitizer. It is basically used for healing, stimulating, or for regeneration of damaged or dyed tissues. This approach is totally opposite to the PDT, in which killing of cancerous cells is focused [14].

2.5.1 Photodynamic diagnosis (PDD) and Photodynamic therapy (PDT)

Photodynamic diagnosis (PDD) is an advanced method for the detection and resection of cancerous cells. The basic principle of the PDD is photochemical molecule known as photosensitizer (PSs) is absorbed by the targeted cancer cells only. Enhanced permeability retention (EPR) effect is responsible for the absorption of the PSs in the selective tumour cells as compared to the normal/ healthy cells. There are different factors that allow the more absorption of PSs in the tumour cells as compared to the normal cells. These factors are vessel permeability, poor lymphatic drainage, and leaky vasculature [135].

When these PSs are illuminated by the light of proper wavelength then light is absorbed by the PSs and remitted with different wavelength. The reported value of the wavelength for the excitation of PSs into single activated state is 330, 400, and 470 nm [136]. Photodynamic therapy (PDT) is therapeutic treatment for the different types of non-oncological and cancerous treatments.

In PDT, light is used to produce reactive oxygen species (ROS) by using photosensitizer. These ROS having cytotoxic effect for death of unwanted cells. Photosensitizers promote to high energy state either singlet or triplet by activating through single or two photons. Through internal conversion or to a different spin state through intersystem crossing, electrons reach the lower energy state from higher energy state. During this procedure, lowering of electrons of photosensitizer form triplet to ground state energy is transferred to an oxygen molecule and this cause the simultaneous promotion of promotion of electrons in molecular oxygen form ground to singlet state as presented in Figure 2.2 [137]. PDT is governed by two different mechanisms. Both mechanisms work simultaneously to produce ROS and singlet state oxygen species [138].

In first mechanism, the PSs is excited by the photons of light and then by intersystem crossing these excited electrons of PSs are moved from the first excited to third excited state. The excited triplet state electrons of PSs react directly with the surrounding cells and leading to the production of ROS. In type II reaction, the energy from the triplet state oxygen is directly transfer to the subcellular oxygen concentrations to produce singlet state oxygen. This singlet state oxygen species is responsible for phototoxic effects of PDT for killing of cells [135], [139].

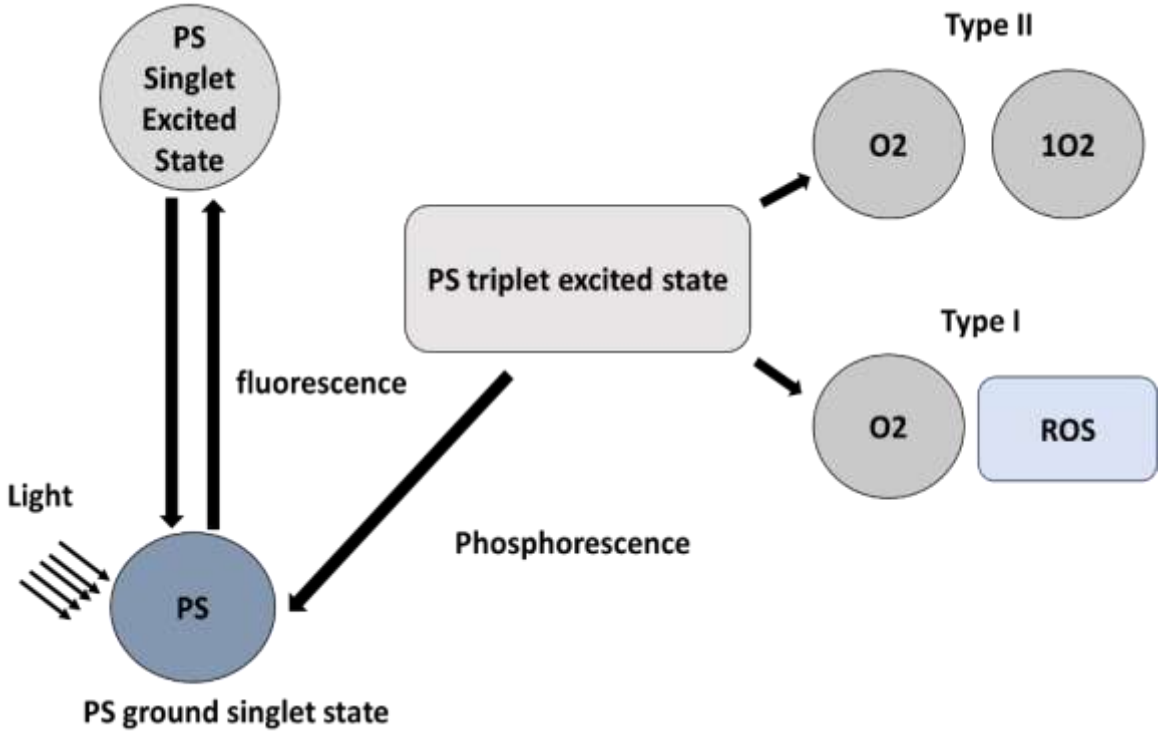

Figure 2.2: Representative image of PDT mechanism for singlet oxygen production by using photosensitiser.

2.5.2 Photobiomodulation (PBM)

A form of light therapy that used non-ionizing form of light sources like LEDs, broadband light, and lasers in the range of visible and infrared spectrum. It involves photothermal and photophysical processes of light with endogenous chromophores [140]. Photobiomodulation also known as low level laser or light therapy (LLLT). It mostly prefers to use the light in red or infra-red region with wavelength range 600 to 700 nm and 780nm to 1100nm. Laser or LEDs having continuous or pulsed light with power density in the range of 5 mW /cm^2 to 5 W /cm^2 [141]. It is proposed that PBM directly interacts on ETC in the mitochondrial membrane. Chromophores those are present in mitochondria absorb photons from PBM, specifically cytochrome c oxidase (CCO) in complex IV of ETC absorb photons from PBM and activate different molecules like nitric oxide (NO), ATP, calcium ions, reactive oxygen species (ROS) and many other signalling molecules [142].

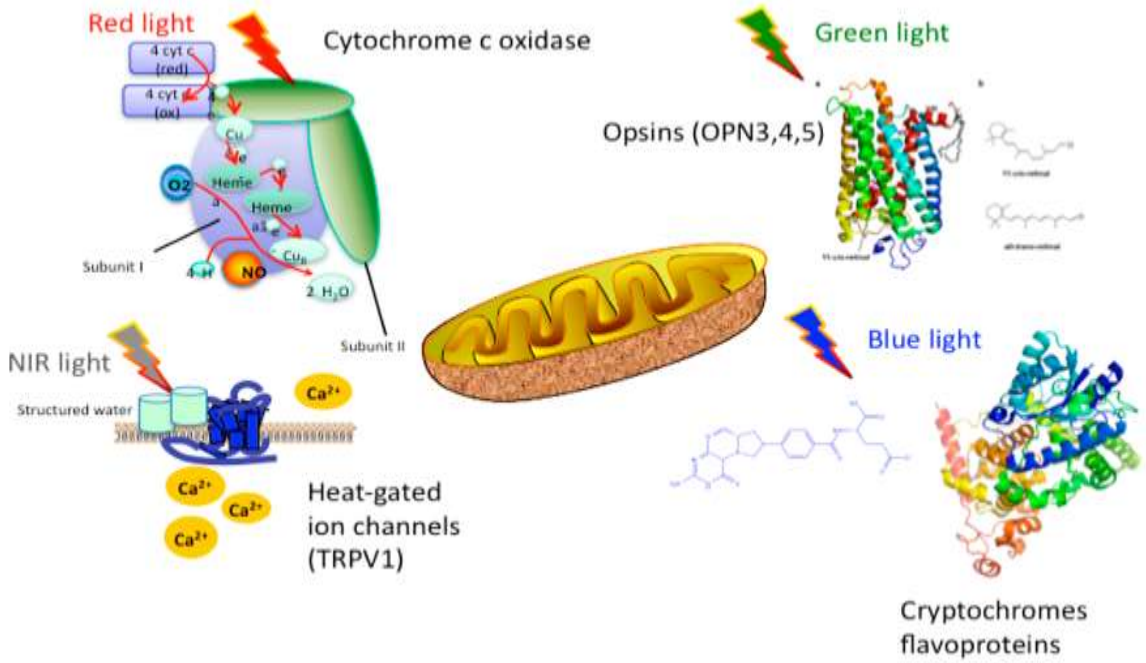

Figure 2.3: Representative image of PBM, absorption of different wavelengths of light by the chromophores in cell [143].

As the photoacceptor, mitochondrial CCO is the first step in the intracellular photo signalling pathways as shown in eq.1. CCO is a multicomponent protein, and it contains CuA and a3-CuB. The first enzymatic activity of CCO is (reduction of oxygen to water) as presented in equation no. 1.

$$4H^+ + 4e^- \rightarrow 2O_2 + H_2O \qquad \text{Eq.1}$$

During this CCO/H_2O reaction, super oxide ($O2^-$), hydrogen peroxide(H_2O_2) and hydroxyl ion (OH^-) will be produced as presented in equation no. 2. As these are collectively known as Reactive Oxygen Species (ROS). there is also release of NO and ATP production in the cells. CCO second enzymatic activity is the reduction of nitrite-to-nitrite oxide. This is called CCO/NO reaction [144].

$$NO2^- + Fe\ (II) + H^+ \rightarrow Fe\ (III) + OH^- \qquad \text{Eq. 2}$$

The nitic oxide generated by this activity is for initiating the signalling pathways. CCO acts like terminal enzymes and causes to increase the production of NO, Calcium ions, ATP, ROS, and other signalling molecules. It is presumed that glycolysis and production of ATP are promoted due to PBM stimulating electrons in chromophores and then these electrons deliver form electron carriers like CCO to electron acceptor and proton gradient is formed and it cause the increase of ATP production [142].

2.5.2.1 Production of singlet oxygen

Oxygen and ROS act a prominent function in the regulation of basic cell functions in both cases either under normal conditions or under the influence of various pathogenic factors. In the mitochondrial respiratory chain, oxygen is a strong oxidiser which makes it an excellent electron acceptor [145]. Reactive oxygen species are chemically active molecules found in living cells naturally. In may biological processes like mitochondria respiration, signal transduction and photosynthesis, these species are active participants [138]. Mitochondrial electron transport chain produces superoxide and hydrogen per oxide at different locations within mitochondria as shown in Figure 2.4.

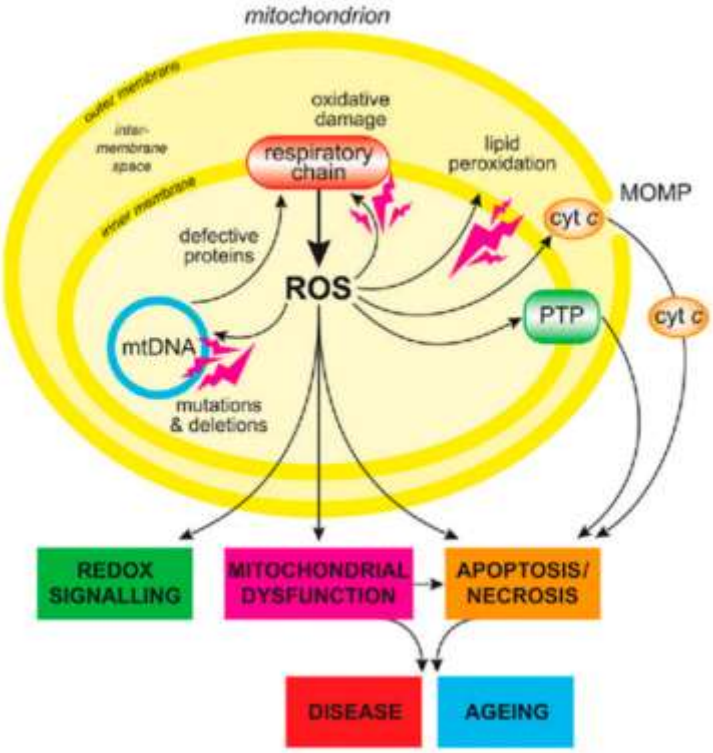

Figure 2.4: Generation of ROS in mitochondria, mtDNA damage and apoptotic cell activation is shown in Figure [146]

The term ROS refer to indicate any oxygen containing molecule radical or non-radical. ROS include superoxide anion ($O2^{\bullet-}$), hydroxyl radical (•OH), peroxyl ($RO_2^{\bullet}$) hydroperoxyl ($HO_2^{\bullet}$), alkoxyl ($RO^{\bullet}$) as radicals, hydrogen peroxide (H_2O_2), singlet oxygen ($^1O_2$) and hypochlorous acid (HOI) as nonradical molecules, [147], [148], [149]. Atmospheric oxygen (O_2) is free molecule and exists in ground state ($^3O_2$). It has two unpaired parallel spin electrons with same spin number which drop off its reactivity. The idea of direct activation and transition of $^3O_2$ to $^1O_2$ is forbidden as electric dipole transition due to even parity of ground and excited states. To get rid of spin restrictions of $^3O_2$ and for production of ROS, additional energy

from some biochemical reactions like ionizing irradiation, UV-B and electron-transport chain can help [149], [150].

Singlet oxygen is lowest excited state of molecular oxygen, production of its enough quantity in biological environment can lead to different cellular processes to cell death via apoptosis or necrosis. A very common way to produce singlet oxygen is irradiation of photosensitizer with ultraviolet or visible light. Many potential organic, inorganic photosensitizer for example metal complexes, semiconductor quantum dots (QDs), graphene (QDs), metal nanoparticles, metal nanowires have been reported [151] [152]. To produce molecular oxygen through traditional PDT is more complicated as compared to the direct irradiation. PDT required irradiation source, PS absorption, optical properties of irradiated tissues. PS has many restrictions like high chemical purity, minimal dark toxicity, and cytotoxicity in the presence of light, high quantum yield for $^1O_2$ generation, strong absorption with high extinction coefficient. But in the case of direct excitation of molecular oxygen, focused light for excitation of target tissue is required [153].

As all ROS at high concentration is very toxic. Cell is said to be in “oxidative stress” when level of ROS is exceeds a defence mechanism [148]. The source of production of ROS is mitochondria. ROS can lead to oxidative damage to mitochondrial proteins, DNA, membranes. It also impaired the ability to synthesize ATP to carry out wide range of metabolic functions, fatty acid oxidation, tricarboxylic acid cycle, urea cycle, amino acid metabolism, haem synthesis and FeS centre assembly that are necessary for normal operation of cells [154]. It is also noted that ROS are very reactive but having very short half-life, in biological system half-life of $^1O_2$ is below 0.04μs and its action radius is under 0.02μm. Therefore only substrates very close to the places of ROS generation will be affected firstly [155].

Triplet state of oxygen $^3O_2$ has absorption bands in the visible and infrared regions as shown in absorption spectrum in Figure 2.5 at which $^1O_2$ can potentially be generated [156]. To produce $^1O_2$, $^3O_2$ is excited through energy transfer from photosensitizer. However, even in the absence of photosensitizer, $^1O_2$ can be directly observed in the NIR region at 1264-1270 nm [151], [157]. It is also reported that 1268 nm matches with NIR absorption band of oxygen molecule. This leads to direct activation of molecular oxygen through photoexcitation [150].

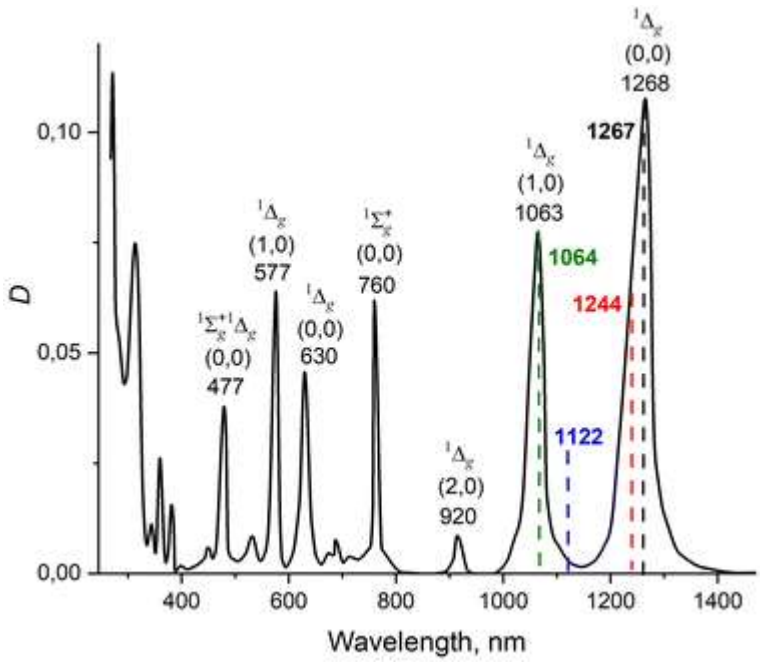

Figure 2.5: Absorption spectrum of oxygen dimers in gas compressed to 150 atm [156].

2.5.2.2 Applications and Therapeutic effects of 1267nm wavelength

Near-infrared light operating in range from 650nm to 1700nm have been enthusiastically utilized in various medical procedures. It leads to different photophysical and photochemical effects those can cause various biological effects like cellular proliferation, mitochondrial function, inflammatory signals. It exhibits deeper penetration, minimal absorption, minimum genotoxicity, and reduce scattering in biological tissues as compared to visible light. For promoting tissue healing and reducing inflammation, typically red (600-700 nm) and near-infrared(700-1100 nm) light is utilized [5], [158]. By the specific wavelength excitation in the range between 1262 to 1270nm, $^1O_2$ can be produced without any chemical compounds [156], [159]. The wavelength range of 1262-1268 nm is reported that oxygen has highest adsorption coefficient and for direct excitation of singlet state oxygen without using of photosensitizer [160], [161]. The generation of $^1O_2$ in PDT for treatment of tumours in possible by using PS but direct optical excitation (PS-free excitation) of $^1O_2$ is possible by specific wavelengths, power, and exposure time as shown in the Figure 2.6.

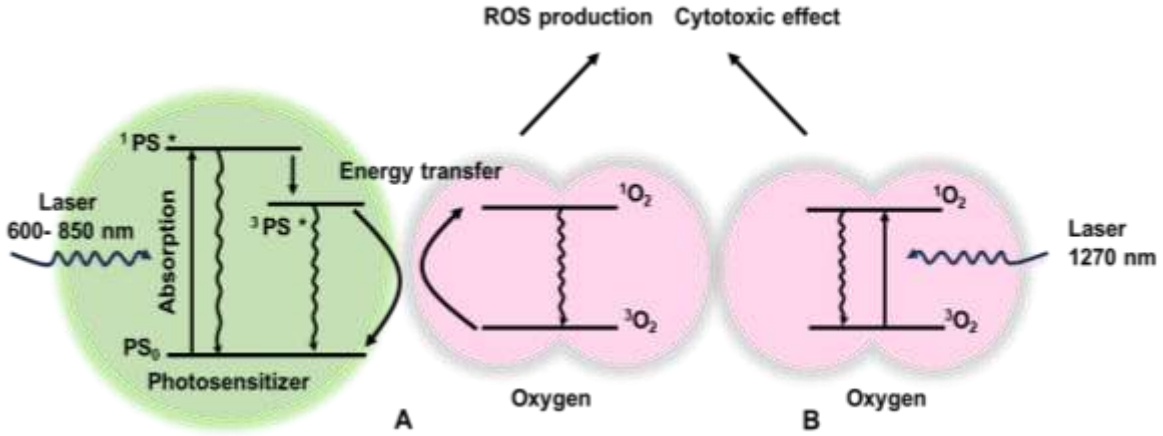

Figure 2.6: 1O2 generation by two mechanisms. (A) generation of 1O2 by photosensitiser (PS) in PDT by using 600-850 nm (B) direct optical generation of 1O2 by using 1270 nm [145], [150]. The 1064 nm, and 1267 nm are most widely used for direct optical excitation of $^1O_2$ [145], [162]. This singlet oxygen causes the production of free radicals mitochondrial dysfunction and initiation of apoptosis and necrosis in cancer cell cultures [159].

2.5.2.3 Apoptosis and necrosis

The word “Apoptosis” is originated from Greek words “apo” meaning away and “ptosis” meaning falling. It is a controlled process of cell death. It was described by Kerr et al in 1970’s[163]. Apoptosis is a form of programmed cell death and ensures that cells have died without releasing harmful substances into surrounding to avoid damaging of neighbouring cells. It is programmed cell death which involve physiological and pathological processes for the elimination of unnecessary cells during the embryonic development and for regulation of cellular homeostasis. It includes a series of morphological changes like plasma membrane blebbing, chromatin condensation, nuclear fragmentation, and formation of apoptotic bodies [164] [165] as shown in the Figure 2.7. For understating pathological conditions and for developing new drugs, detection of apoptosis is very necessary. Apoptosis is triggered by two pathways extrinsic and intrinsic. Extrinsic pathway of apoptosis is due to activation of death receptors (i.e., TNRF family) that is located on the surface of cell membrane. Intrinsic activation depends on the disruption of intracellular homeostasis (i.e., DNA damage, cellular stress) [166].

During apoptosis different biochemical changes also occur include appearing of phosphatidylserine (PS) on the outer leaflet of the plasma membrane, mitochondrial membrane permeability changing, releasing of mitochondrial proteins into intermembrane space (cytosol), caspase activation, and caspase-dependent activation of DNase and DNA fragmentation [167]. PS is involved in many biological processes like apoptosis, erythrocytes, fusion of cellular membranes, and activation of platelets. Annexin V is calcium

dependent protein having high affinity for PS confined in the inner membrane for healthy cells but during apoptosis it translocated to the outer leaflet of the membrane and available for binding of Annexin V to PS for detection of apoptosis [168]. For detection of apoptotic cells, Annexin V is binding protein is used, it is calcium dependent for binding negatively charged phospholipids labelled with fluorescein isothiocyanate (FITC) [169].

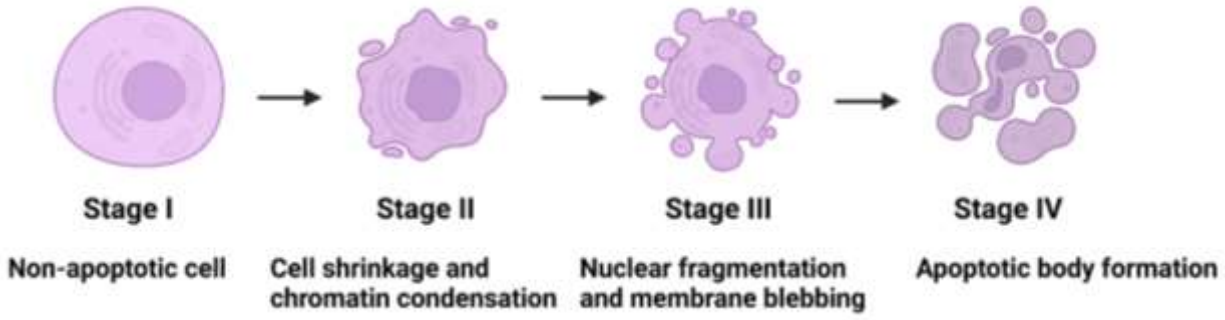

Figure 2.7: Stages of apoptosis form healthy to apoptotic cell (This image has been generated using Biorender).

Necrosis is another form of cell death; it leads to inflammation and intoxication/damage of the surrounding cells and tissues as shown in Figure 2.8. It is uncontrolled and energy independent form of cell death due to external factors like hypoxia, inflammation, chemicals, radiations, heat [170], [171].

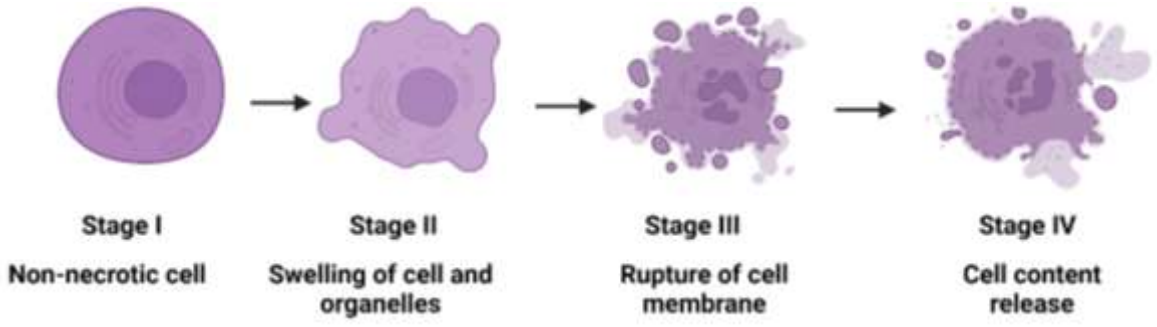

Figure 2.8: Stages of necrosis from non-necrotic to necrotic cell (This image has been generated using Biorender).

Chapter 3

2D and 3D bio-tissue model culturing methods

In vitro, for understanding the tissue morphology, drug delivery and for other biological processes tissue culturing is used widely. Usually, primary cells are obtained from the source tissues then utilized for the purpose of diagnostics and therapy [12].

3.1. HaCaT cells and primary human fibroblasts culturing protocols

The stock of primary human fibroblasts was provided from StratiCELL,SA, Belgium and immortalized keratinocytes HaCaT cells were provided by LUH. Primary human fibroblasts were grown in Dulbecco's Modified Eagle's Medium (DMEM, Thermo Fischer Scientific, UK) media with 10% of Foetal Bovine Serum (FBS, Sigma-Aldrich, UK) and 1% Penicillin/Streptomycin (Thermo Fischer Scientific, UK). Cells were seeded in T75 flask (Corning, USA), incubated in 37ºC temperature humified with 5% CO_2 [172]. Cells were seeded at 4.5 x 10^5 cells/T75. After 5 days of culturing, when cells reached 90% of confluence, Trypsin-EDTA solution (Sigma -Aldrich, UK) was added in the flask and incubate for 2 to 3 minutes at 37ºC.After trypsinization cells were centrifuged (at 800 RPM for 5 minutes) and were utilized for experimental purposes and remaining cells were stored in FBS with 10% dimethyl sulfoxide (DMSO) (VWR Chemicals BD) and stored in liquid nitrogen for further use.

The HaCaT cells were grown in Dulbecco's Modified Eagle's Medium (DMEM) media- high glucose (Sigma-Aldrich, UK) with 10% of foetal bovine serum. Cells were seeded in T75 flask, incubated in 37ºC temperature with 5% CO_2 [173]. Cells were seeded at 4.5 x 10^5 cells/T75. After 5 days of culturing, when cells reached 90% of confluence, Trypsin-EDTA solution (Sigma -Aldrich, UK) was added in the flask and incubate for 2 to 3 minutes at 37ºC. After trypsinization and sedimentation (6 g for 5 minutes) cells were collected, and one vial is utilized for experimental purposes and remaining vials were stored in fatal bovine serum with 10% DMSO and kept in liquid nitrogen for further use.

3.2 Melanoma cell culturing

Melanoma cell line SK-MEL-37 human cells were cultured in Dulbecco's Modified Eagle's Medium (DMEM, Thermo Fischer Scientific, UK) media with 10% of Foetal Bovine Serum (FBS, Sigma-Aldrich, UK) and 1% Penicillin/Streptomycin (Thermo Fischer Scientific, UK) in T/75 flask. Cell cultures are maintained in humidified atmosphere of 5% CO_2 at 37ºC [159]. After 2 days of culturing, the cells reached 90% of confluence, Trypsin-EDTA solution

(Sigma -Aldrich, UK) was added in the flask and incubate for 3 minutes at 37°C. After trypsinization and sedimentation (6 g for 5 minutes) cells were collected, and one vial is utilized for experimental purposes and remaining vials were stored in fatal bovine serum with 10% DMSO and kept in liquid nitrogen for further use.

3.3 Cell viability estimation

The viability of the cells is estimated by using improved Neubauer chamber with Trypan Blue (STEMCELL, technologies Inc.) 0.4% [174]. The viable and non-viable cells of the primary fibroblasts, HaCaT cells and melanoma cells are identified and counted by using improved Neubauer chamber and inverted microscope (Motic AE 2000, Motic, UK). For fibroblasts and HaCaT cells, viability of all cell lines cultured were 80%± 10 SD.

Table 3.1: Viability test of HaCaT cell and fibroblasts using trypan blue.

Cell Type	Concentration (cells/ml)	Viability (%) ± 10%
HaCaT	5.0×10^6	80
HaCaT	7.5×10^6	85
HaCaT	10.0×10^6	80
fibroblasts	3.0×10^6	80
fibroblasts	4.0×10^6	80
fibroblasts	5.0×10^6	80

For n=9,

3.4 3D biological models

3.4.1 Full-thickness skin equivalence (FSE) preparation protocol

PEGylated fibrinogen was prepared composed of PEG-NHS (Sigma-Aldrich) and fibrinogen (Sigma-Aldrich). Human primary fibroblasts of $1x10^5$ per ml were suspended in PEGylated fibrinogen solution along with 100 µl $CaCl_2$ (50Mm) and 100 µl thrombin (40 IU/ml in TBS) (Sigma -Aldrich). This composition was added into the scaffold inside 6-well plate. The cell culture plate put in the incubator for 1 hour for polymerization. Afterwards 4 ml media (DMEM + 10% FBS + 1% Penicillin/Streptomycin) was added to the wells and was kept at CO_2 incubator at 37^0C for 48h. The HaCaT cells of $9x10^5$ cells/ml were seeded on the top of the fibrinogen gel. Completed sets of FSEs on the scaffolds in 6-well plates were cultivated with media 4ml of DMEM+10% FBS with 10mg/ml aprotinin changed every 2 days, for final maturation of FSEs.

3.4.2 Melanoma full-thickness skin equivalence (Melanoma-FSE) preparation protocol

PEGylated fibrinogen was prepared composed of PEG-NHS (Sigma-Aldrich) and fibrinogen (Sigma-Aldrich). Human primary fibroblasts of $1x10^5$ per ml were suspended in PEGylated fibrinogen solution along with 100 µl $CaCl_2$ (50Mm) and 100 µl thrombin (40 IU/ml in TBS) (Sigma -Aldrich). This composition was added into the scaffold inside 6-well plate. The cell culture plate put in the incubator for 1 hour for polymerization. Afterwards 4 ml media (DMEM + 10% FBS + 1% Penicillin/Streptomycin) was added to the wells and was kept at CO_2 incubator at 37^0C for 48h. The HaCaT cells of $9x10^5$ cells/ml and melanoma cells of $1x\ 10^4$ cells/ml were seeded on the top of the fibrinogen gel after 4 days of culturing. Completed sets of Melanoma-FSEs on the scaffolds in 6-well plates were cultivated with media 4ml of DMEM+10% FBS with 10mg/ml aprotinin changed every 2 days, for final maturation of Melanoma-FSEs.

3.5 NAD and FAD chemical solution preparation

10 mM stock solutions of NADH and FAD (Sigma-Aldrich, USA) have been prepared in Dulbecco's phosphate-buffered saline (DPBS, Sigma Aldrich). Eight different concentrations of 1 mM, 0.6 mM, 0.3 mM, 0.1 mM, 0.03 mM, 0.01 mM, 0.003 mM, and 0.001 mM with have been prepared from the initial stock solution and kept in -20 ^{o}C. The stock solution was shielded in metal foil for prevention the effect of photobleaching due to natural room light. For all measurements of NADH and FAD, a quartz cuvette is used having a transmission optical path of 10 mm.

3.6 Laser printed 3D scaffolds FSE

Two-photon laser-printed 3D scaffolds fabricated from biocompatible commercially available material (Dental-LT-Clear) (Formlabs, Germany). 2PP with BioScaffolder system (Laser nanoFab GmbH, Germany) was used to produce 9 mm round scaffolds. The architecture of the 3D scaffold was comprised of two layers with 80 µm height, 30 µm cylinder wall thickness and an inner pore diameter of 240 µm [22]. Scaffolds were sterilized using 70% ethanol and UV light for 30 min. Polystyrene clear flat bottom TC-treated 6-well plate (Corning, Falcon, USA) was used for cell seeding.

3.7 DLP (digital light processing) printed 3D scaffolds

BIONOVA DLP printer (Cellink, Sweden) is utilized for fabrication of 3D scaffolds by using biocompatible resin DClear (Formslab, Berlin, Germany). All models are designed in (Blender 3.5) and converted into STL file for DLP printing. These scaffolds are prepared by

photopolymerization process by using UV light. For this purpose, one well of 6-well plate (BIONOVA X) filled with liquid DClear monomer and cured by using UV light. Fabrication occurred at 0.1mm/sec motion speed at 60^{o}C temperature to produce desired geometry from defined parameters.

3.8 Immunohistochemistry (IHC)

IHC is powerful and widely used technique that exploits the specific binding between an antibody and antigen. It is used to detect and localize antigens in cells of a tissue. It is less expensive and widely used method as compared to other methods in anatomical surgical pathology for cell classification in tissue sections [175]. In surgical pathology, IHC has become standard assay. It includes some sequential steps which are as follows, antigen retrieval, addition of secondary antibody. It is applied for binding primary antibody. Finally, a detection reagent is applied for visualization of localization of primary anti body [176].

3.8.1 Tissue preparation (microtome sample preparation method)

Tissues are frozen in liquid nitrogen or can be fixed in 4% formaldehyde. The FSE along with the scaffold, was taken from the scaffold holder and fixed in 4% formaldehyde at room temperature and embedded in paraffin using the RHS-2 microwave. Haematoxylin and eosin (H&E) were used for staining 6 µm sections of skin tissues using microtome [177]. The sections are then dehydrated in an ethanol bath, isopropanol bath and Ultraclean bath. Finally, the FSE sections were mounted by using an Ultra kit.

3.8.2 Tissue preparation (cryostat sample preparation method)

Cryostat sections of samples (5-µm thickness) cut at -20^{o} C on a cryostat NX70 cryostat (Thermo Fisher Scientific, USA). Samples has been embedded in OCT solution. After cutting samples are collected on glass slide[178]. For H&E staining of cryostat sectioning, samples were air dried for 15 min. Nuclei of samples are stained with haematoxylin (Sigma-Aldrich) for 30sec, then for 5 min placed in running tap water and after that placed in distilled water. Sections were then stained with eosin (Sigma-Aldrich) for 20 sec and placed in distilled water for 5 times, 15 times in 70% ethanol, 15 times in 96% ethanol, and for 10 times in 100% ethanol. After this process, sections were rinsed with xylene for 5 min for 3 times [178].

3.9 Cell culturing on glass coverslips

Primary human fibroblasts, HaCaT cells, and melanoma cells are seeded on plated poly-D-lysine coated glass coverslip in six well plate[161]. Primary human fibroblasts were grown in Dulbecco's Modified Eagle's Medium (DMEM, Thermo Fischer Scientific, UK) media with

10% of Foetal Bovine Serum (FBS, Sigma-Aldrich, UK) and 1% Penicillin/Streptomycin (Thermo Fischer Scientific, UK). The volume of cell culturing media in every well of 6-well plate (Corning, Falcon, USA) is about 500µl. Cells were seeded at 1 x 10^5 cells and incubated in 37°C temperature humified with 5% CO_2. After 2 days of culturing, cells reached 70% of confluence.

The HaCaT cells were grown in Dulbecco's Modified Eagle's Medium (DMEM) media- high glucose (Sigma-Aldrich, UK) with 10% of foetal bovine serum. Cells were seeded at concentration of 1 x 10^5 cells and incubated in 37°C temperature humified with 5% CO_2. The volume of cell culturing media in every well of 6-well plate (Corning, Falcon, USA) is about 500µl. After 2 days of culturing, cells reached 70% of confluence.

Melanoma cell line SK-MEL-37 human cells were cultured in Dulbecco's Modified Eagle's Medium (DMEM, Thermo Fischer Scientific, UK) media with 10% of Foetal Bovine Serum (FBS, Sigma-Aldrich, UK) and 1% Penicillin/Streptomycin (Thermo Fischer Scientific, UK). Cells were seeded at concentration of 1 x 10^4 cells and incubated in 37°C temperature humified with 5% CO_2. The volume of cell culturing media in every well of 6-well plate (Corning, Falcon, USA) is about 500µl. After 2 days of culturing, cells reached 70% of confluence.

3.10 Apoptosis (Annexin V-FITC and PI staining)

Annexin V/PI is commonly used for counting the apoptotic and necrotic cells stained by Annexin V and propidium Iodide solution. Glass cover slips seeded with cells are washed twice with Dulbecco's phosphate-buffered saline (DPBS, Sigma Aldrich). After laser irradiation of cells for 2 min, add 5µl of annexin V (Abcam, ab14085, UK) and 5µl of PI (Abcam, ab14085, UK) to 500µl of binding buffer to the perfusion chamber (RC-26GL, Warner Instruments, USA) containing glass cover slip seeded with cells. After adding this solution incubate cover slip in dark for 5 min at room temperature [179]. After incubation, cells are washed for 2 min with DPBS solution. Observe the cells under fluorescence microscope using dual filter FITC for Annexin V and rhodamine for PI.

3.11 Singlet oxygen production assay (Si-DMA)

Si-DMA is composed of (silicon containing rhodamine (Si-rhodamine) moieties and 9,10-dimethylanthracene (DMA)). Si-DMA is used to visualize intracellular $^1O_2$ in real time [180].

The production of mitochondrial singlet oxygen without using of photosensitizer has been evaluated by using Si-DMA (Sigma-Aldrich, UK)

Primary human fibroblasts, HaCaT cells at $1x10^5$ and melanoma cells at $1x10^4$ are cultured on glass cover slip 48 hours before the experiment in 6-well plate (Corning, Falcon, USA). The total media in the well plate is about 500µl. Discard the culture media and wash the cells twice with 200µl of Hanks HEPES buffer twice. Load cells with 1µm Si-DMA at 37°C for 30 min. Wash again cells twice with Hanks HEPES buffer of 200µl. Add Hanks HEPES buffer (200µl) and observed the cells under fluorescence microscopy at 650nm excitation wavelength [161].

3.12 Data and Statistical Analysis

The results of experiments were averaged and presented as mean ± standard deviation (SD). Data and statistical analysis were performed using OriginPro software (OriginLab Corp., USA). Data were considered significantly different if $p < 0.05$ by non-parametric Mann-Whitney *U*-test.

Chapter 4

Development and validation of customized FS-OCT system

4.1 Introduction

The concept of multi-modal optical system is introduced to enhance and improve biomedical imaging system by combining different imaging techniques [181]. For diagnosis, there are many techniques and methods but all of them has some limitations and problems. Fluorescence spectroscopy (FS) is an emerging tool for the purpose of diagnosis in the field of medical sciences because of its fast processing, high sensitivity and low cost [119].

For studying *in-vivo* human tissue pathology and functions, developing of 3D models is primary focus in tissue engineering research [182]. The reconstruction of human diseased organs is extremely limited. 3D artificial tissue models and organs can be one of the approaches in advancing treatment of diseases. It is now possible to fabricate large and complex multi-layered tissues like skin, cardiac tissue, bone tissue, liver, lung, etc. in health or pathology for research and clinical applications [79]. For decades two-dimensional cell cultures were used for in cell biology research as golden standard. To study the cellular response of 2D cell culture models being necessary but not sufficient for studying responses of 3D tissues/organs in whole complexity their interaction with biochemical and biomechanical microenvironment it has certain limitations in mimicking intra- and extracellular matrix signalling cues. 3D models are supposed to be the most realistic platform and more prominent in drug developments and reconstruction of tissue models, cosmetics testing [183] studies of the inherited genetic disorders [184], [185].

To create artificial 3D tissues the 3D bioprinting is an innovative strategy including deferent cell types, growth factors and extra cellular matrix (ECM) components [79] and 3D scaffold fabrication [186]. To provide a superior microenvironment for cell migration, proliferation and tissue generation, microporous 3D scaffolds can mimic ECM. For the fabrication of 3D scaffolds, there are numerous methods including, extrusion or laser-induced forward transfer (LIFT), DLP-based 3D printing, electrospinning using different hydrogel-based and photopolymers as bioinks[187]. For *in-vitro* cell accommodation and development of tissue with certain functionalities, 3D polymeric scaffolds could be a powerful tool. For producing high level of structural design of 3D scaffolds, two-photon polymerization technique (2PP) is employed for achieving high resolution and complex structures for nanoscale applications [188]. These 3D scaffolds can generate tissue constructs for investigating of different types of tissues like muscle, bone, cornea, and skin [189].

For fundamental research, drug testing, and clinal studies, human FSEs have been pronounced a close substitute to the true skin. FSE can be constructed by using skin cells primarily or TRET-immortalized keratinocytes and fibroblasts [190]. For this purpose, cultured cells are utilized for creating and generating 3D human organs for the purpose of replacement and grafting [191].

To obtain adequate information about 2D cell cultures and 3D tissues, optical imaging and spectroscopies are valuable tools for estimation of morphology and biochemical details [192]. For understanding cell function, diagnostics and treatment, metabolic monitoring at the cellular level is important. Among different biochemical markers, redox ratio is an approximation between oxidation and reduction reactions, particularly within the mitochondrial matrix space, provide cells metabolic rate and redox state [193]. This ratio reflects how cells regulate ROS and antioxidant defences for maintain cellular health and functions. A balanced redox ratio is crucial for normal physiological functions, as excessive oxidation can cause permanent damage to biomacromolecules such as lipids, proteins and DNA, which can lead to cellular death or development of disease [194].

A broad range of fluorophores and chromophores are co-existed in the skin tissue like lipofuscin, collagen, elastin, porphyrins, protein, haemoglobin, NADH, and FAD. For monitoring the changes in mitochondrial metabolic activity of skin tissue, two most important endogenous fluorophores were valued reduced nicotinamide adenine dinucleotide (NADH) and flavin adenine dinucleotide (FAD) [15], [17], [19], [23], [31]. These two coenzymes can also be detected in keratinocytes and fibroblasts of FSE which make them prominent indicator of the FSE metabolism [195]. Redox ratio (RR) calculated from NADH or NADPH/FAD measurements can be a hall mark of cell maturation and aging [196] [25], [34]. Besides fluorescent spectroscopy used for assessment of the cellular metabolic activity OCT can non-disruptively image the 3D FSE morphology and provide a non-invasive real-time cross section of FSE with an ideal balance between penetration depth 2 mm and resolution 10-15 μm [197].

Our aim was to print biocompatible 3D scaffolds and build dual-channel OCT/FS system capable of providing morphological and metabolic assessment of 3D constructed FSE and Melanoma-FSE model. The performance of multimodal optical system has been validated by simultaneous measurement of fluorescence spectra and OCT image of 3D developed human skin and melanoma models.

4.2 Development of combined OCT and fluorescence spectroscopy system

The FSE approach in skin molecular biology research was used to study human skin development in dynamics where H&E histology was a main visualisation technique of FSE maturation. During the preparation of the samples for H&E histology the FSEs are destroyed making this approach expensive and more labouring. Why we have chosen OCT imaging and FS for non-destructive optical interrogation of 3D FSE morphology and metabolic activity. Therefore, NADH and FAD fluorescence profiling of the FSE cell metabolism with FS and its structural integrity OCT imaging together will give practically full information on FSE developmental state.

That why we developed the experimental setup including FS system with OCT Figure 4.1. The FS system with fiber optical probe containing emitting and collecting fibers was developed for recording fluorescence intensity (FI) spectrum after 365 and 455 nm excitation. The choice of emitter wavelengths was depended on NADH and FAD fluorescence excitation features. To reduce the photobleaching effect, the radiation power of the 365 nm LED excitation source (M365FP1, Thorlabs, USA) did not exceed 0.35 mW. The output power for the 455 nm LED excitation source (M455F3, Thorlabs, USA) was even lower, 0.1 mW. Fluorescence radiation in the range of 350-1000 nm were analyzed using a FLAME-T-VIS-NIR-ES spectrometer (Ocean Insight, USA). To attenuate the backscattered radiations of the LED sources, Ø12.5 mm long-pass filters (Edmund Optics, USA) were used. Fiber-coupled INLINE-SFH accessory (Ocean Insight, USA) was used as a filter holder. The R400-7-UV-VIS optical probe (Ocean Insight, USA) has 6 illumination fibers around 1 read fiber. All fibers have 400 μm core size. The numerical aperture of the fibers is 0.22.

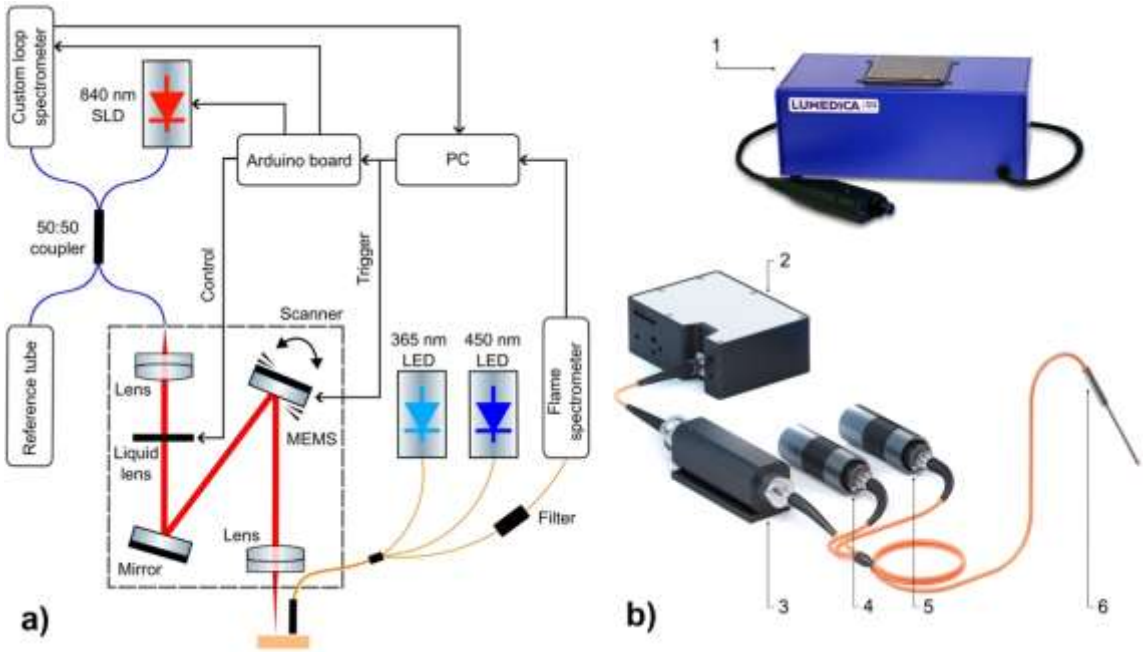

Figure 4.1: (a) General scheme of the experimental setup and (b) overview of channels: 1- Lumedica OCT imaging system, 2- spectrometer, 3-filter holder with long-pass filters, 4- LED 365 nm, 5- LED 455 nm, 6- optical probe.

We studied the spectroscopic intensities of NADH/NADPH and FAD before performing non-invasive fluorescence spectroscopy of HaCaT cells and primary fibroblasts in suspension and FSE model for its metabolism assessment on 3D scaffolds. Our investigation revealed that human full thickness skin equivalent model can be developed successfully within 14 days for therapeutical purposes. FS together with OCT imaging provides metabolic and morphological information of constructed 3D skin model at the same time.

For non-invasive visualization of morphological features of FSEs, the compact, reliable, and easy to use Lumedica OCT imaging system was selected (Lumedica Inc., USA). Light source is provided by super luminescent diode (SLD) with centre wavelength 840nm, that is coupled with interferometer and high-resolution spectrometer. A scanner is also mounted with the system for scanning samples. Resolution depth is 5 microns in tissue, transverse resolution 15 microns, linear scan range 7 mm. These parameters are influenced on choosing of this specific system.

4.3 Assessing FS module sensitivity to NADH and FAD concentration range

The sensitivity of built FS module to NADH and FAD fluorescence was assessed with range of the chemicals dissolved in DPBS. We performed experiments for NADH and FAD with different experimental strategies.

The fluorescence spectra (insertions) of NADH solution at 365nm and FAD solution at 365 nm and 455 nm and their normalised fluorescence intensity (nFI) at different concentrations are shown in Figure 4.2. nFI values demonstrated strong correlation with concentration of NADH and FAD in the solution, the higher nFI value corresponds to coenzymes higher concentration Figure 4.2 (a, b, c).

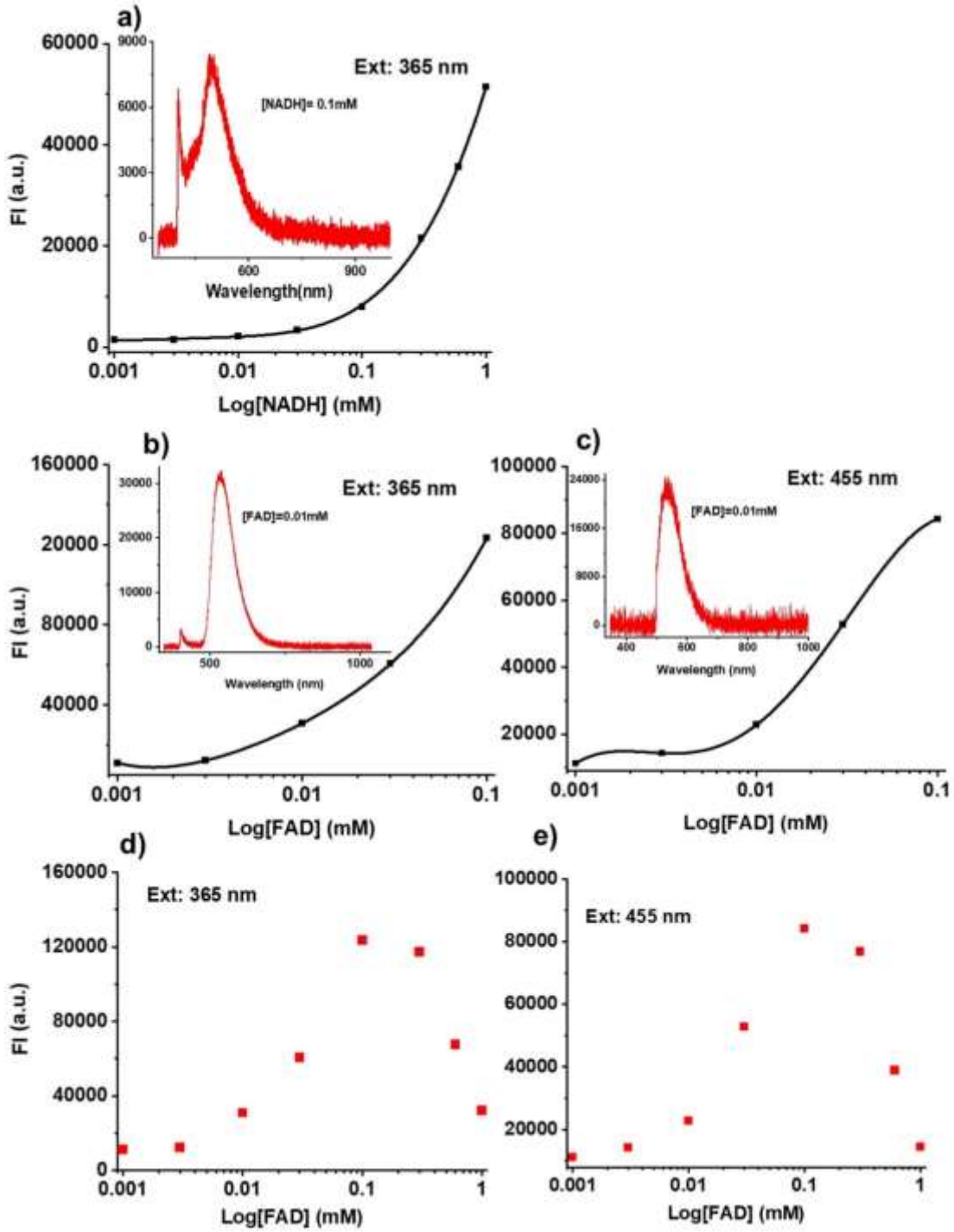

Figure 4.2: Normalised fluorescence intensity to correspond LED power, 0.35 mW for LED 365nm and 0.1 mW for 455nm of (a) NADH and (b-e) FAD of different concentrations measured with custom-

built FS module. Insertions: representative fluorescence spectra of NADH (0.1 mM) and FAD for different concentrations of coenzymes for UV (365 nm) and blue (455 nm) excitation lights. Each measurement was repeated n=3, experimental data from a, b, c were fitted with 4-order Polynomial function utilising OriginPro program.

Data shown at Figure 4. 2 (a) represent NADH nFI excited with 365 nm. Even at highest 1 mM NADH concentration FI saturation wasn't indicated. nFI data shown at Figure 4.2 (b) represent FAD nFIs excited with 365 nm. Results displayed at Figure 4.2 (c) represent FAD nFI data by 455 nm excitation, which demonstrated a significant increasing trend. at 0.3 mM and higher quenching effect can be observed starting from and higher FAD concentrations. Due to quenching effect of FAD molecules at high than 0.1 mM concentrations, the irradiation of 365 and 455 nm starts absorbing by FAD molecular complexes and actual nFI readouts proportionally declined Figure 4.2 (d, e) [198]. These experimental results confirmed that FS module demonstrated sensitivity thresholds for both main coenzymes of mitochondria ATP anabolism within their nominal values as they were measured in the mouse spleen tissue for NADH in the range of 90-520 μM and for FAD of 80 – 400 μM [199]. After the validation of FS mode sensitivity with different concentrations of NADH and FAD, we validated it by using HaCaT cell and fibroblast suspensions.

4.4 NADH/NADPH and FAD levels in HaCaT cell and fibroblast suspensions and optical redox ratio

The selectivity and sensitivity of the FS module in detecting NADH and FAD contents in living cells were evaluated on immortalized keratinocyte (HaCaT) and human primary fibroblast suspensions on the background fluorescence from other cellular endogenous chromophores Figure 4.3. These coenzymes, NADH and FAD, are directly involved in production of adenosine triphosphate (ATP) and exist in reduced form ($NADH/FADH_2$) or in oxidized form (NAD^+ or FAD) [200]. It is reported that NADH shows high fluorescence compering with FAD within cells culture too [192]. In cellular and tissue measurements, the fluorescence emissions of NADH and its phosphorylated form NADPH are indistinguishable [196], so NADH/NADPH is used to represent combined signals for NADH and NADPH. In this case, comparing $_{max}FI^{NADH/NADPH}$ and $_{max}FI^{FAD}$ for both cell lines NADH/NADPH has higher values than FAD for 455nm excitation.

Data displayed on the Figure 4.3 (a, b) represent fluorescence spectra for both cell types and wavelength excitations. NADH/NADPH and FAD numerical data were taken at 492 nm and 535 nm maxima of the coenzyme FI. As it can be seen FIs simultaneously emitting from both biomarkers had higher contribution from NADH/NADPH than from FAD. Data on Figure 4.3 (b, d) graphs represent maximum FI ($_{max}FI$) related to metabolic activities of viable cells

at three different concentrations $5x10^6$, $7.5x10^6$ and $10x10^6$ cells/ml. We collected FI of emission spectra for HaCaT cell and fibroblast suspensions at 492 nm and 535 nm correspondent to emission maximum FI of NADH/NADPH and FAD respectively. It should be noted that other cell fluorophores., collagen, elastin, emissions contribute to readings from NADH/NADPH and FAD maximum FI ($_{max}FI^{NADH/NADPH}$ and $_{max}FI^{FAD}$) of cells increasing actual $_{max}FI^{NADH/NADPH}$ and $_{max}FI^{FAD}$ values. Since $_{max}FI$ values of NADH/NADPH and FAD were compared in different cell concentrations the additive effect of other cellular fluorophores can be ignored.

For NADH/NADPH, with the increasing cell concentration the $_{max}FI$ is also increased. In detecting FAD after excited at 455nm, highest FI is detected for concentration at $7.5x10^6$ cells/ml, further increase in cell concentration didn't reduce $_{max}FI^{FAD}$.

For label free detection of changes in cell and tissue metabolism type [200], optical redox ratio (ORR) is often calculated. The cell or living tissue ORR can potentially demonstrate integrity of the cellular energetic metabolism and in the turn indicate the state of the cell/tissue development/maturation. There are many ways how to calculate ORR [196]. The ORR is calculated using following formula $ORR=_{max}FI^{NADH/NADPH}/(_{max}FI^{NADH/NADPH} + _{max}FI^{FAD})$. The use of $_{max}FI^{NADH/NADPH}$ and $_{max}FI^{FAD}$ in calculating the ORR can be ascribed to alterations whether glycolitic and oxidative phosphorylation metabolism acquired [201]. If ORR increased, it indicates that metabolism rather shifted to glycolytic type due to prevalent decrease of FAD generation or increase of NADH/NADPH concentration due to glycolysis. Contra versa an increase in oxidative phosphorylation reduces NADH/NADPH while FAD is increased [196].

Figure 4.3 (e) shows ORR of HaCaT cells and fibroblasts after UV exposure. It is revealed that change in ORR of both cell types is not significantly different. The increase of $_{max}FI^{NADH/NADPH}$ and $_{max}FI^{FAD}$ following 365nm exposure, leads to increase in ORR for both cells type. The change in ORR usually indicates relative changes in oxidation phosphorylation in cell mitochondria [33].

4.5 NADH/NADPH, FAD, and ORR in aging of HaCaT cells and fibroblasts cultures

For the validation of FS device, HaCaT cells and fibroblasts cultured for different time periods (5, 7, and 9 days) were assessed for $_{max}FI^{NADH/NADPH}$ and $_{max}FI^{FAD}$ with FS system and results are shown Figure 4.4.

Figures 4.4 (a) and 4.4 (b) correspondingly represent the dependence of $_{max}FI$ of main coenzymes of mitochondria metabolism HaCaT cells and fibroblasts for 5, 7 and 9 days.

The shift of $_{max}$FI for both NADH/NADPH and FAD towards their decline was prominent for both of cell types at both excitation wavelengths. The decline in both coenzyme FIs but not ORRs with aging both cell cultures was identified pointing at that type of metabolism was not changed staying balanced between glycolysis and oxidative phosphorylation. However gradual decreasing both $_{max}FI^{FAD}$ and $_{max}FI^{NADH/NADPH}$ values due to course of culture aging could point on declining of general metabolic activity which usually happens when 2D culture reached certain state of and confluency or maturation in 3D models [55]. Figure 4.4 (c) represents the comparison between ORR of both cell types cultured for 5, 7, and 9 days respectively. there were no significant changes in ORR values calculated from $_{max}FI^{FAD}$ and $_{max}FI^{NADH/NADPH}$ acquired from UV excitation of cell suspension.

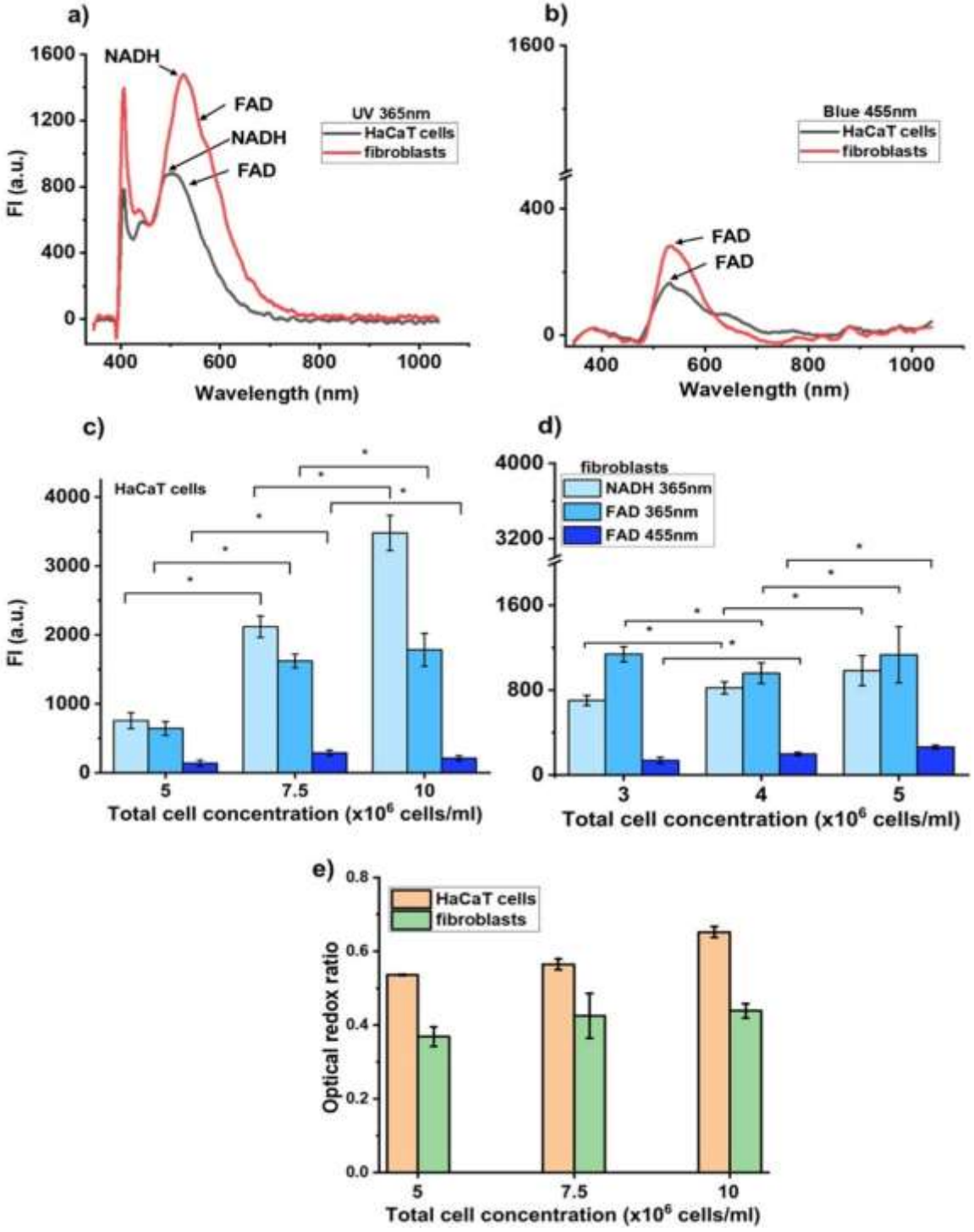

Figure 4.3: FS selectivity and sensitivity valuation on HaCaT cell and fibroblast suspension at concentration of 5 x106 cells/ml for both excitation (a) UV 365 nm (b) blue 455 nm. NADH/NADPH and FAD FI measured at their maxima (492 nm and 535 nm correspondently) of cell spectra; (c) FI measured in HaCaT cells and (d) fibroblasts of three different concentrations (n=3, * – indicates $p<0.05$ between different cell concentrations); (e) comparison of optical redox ratio of HaCat cells and fibroblasts after exposure at 365nm.$p<0.5$, Data is presented as mean±SD.

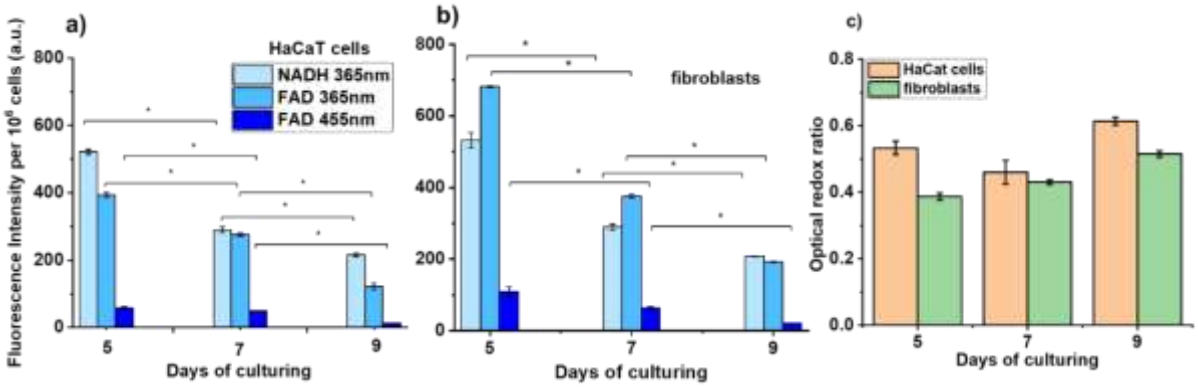

Figure 4.4: The maxFI gained from of NADH/NADPH and FAD fluorescence spectrum maxima for (a) HaCaT cell and (b) fibroblast suspensions at the different culturing intervals. Data are presented as mean±S.D (n=3, * - p<0.05). c) comparison between cellular redox ratio of HaCat cells and fibroblasts after exposure at 365nm for different days of culturing, p<0.5, Data are presented as mean±S.D.

This reflects gradual decrease in both NADH/NADPH and FAD FI, which underpins glycolysis/oxidative phosphorylation balance during cell culture development till they reached maturation (full confluency) [196],[202]. With increasing days of culturing for both cell types, ORR stayed unchanged indicating the reduction in metabolism activity, that reflects gradual decrease of both coenzymes fluorescence maxima Figure 4.4 (a, b).

The relationship between cells maturation and metabolic activity revealed with FS module that NADH/NADPH and FAD and general fluorescence levels gradually decreased due to decreasing of energy demands for maintaining high cell proliferation. Insignificant changes in ORR reveals that at longer term culturing both cell types begun equally using glycolysis and oxidative phosphorylation for keeping optimal energy production (NADH/ATP) utilising both anaerobic and aerobic metabolic pathways [200].

4.6 Culturing FSE on two photon printed 3D scaffolds with customised architecture

There are some limitations in using 2D skin cell monolayer cultured on a solid surface under certain physio-chemical conditions the 3D skin models undeniably became valuable approach for studying pathologies and new drugs and cosmetics [203] testing. These 3D models allow unmixing co-culturing of layers of different cells (fibroblasts, keratinocytes, melanocytes) to proliferate and interact vertically and horizontally all cell components within an extracellular matrix developing highly comprised artificial tissue [204]. Therefore, human full thickness skin equivalents have multiple use and benefits in examining not only how newly developed drugs/cosmetics with epidermal and dermal cells, but epidermal gene

expression and understanding the roles these two layers in disease modelling and wound healing. It is also promising tool for significantly decrease of animal testing [36], [205].

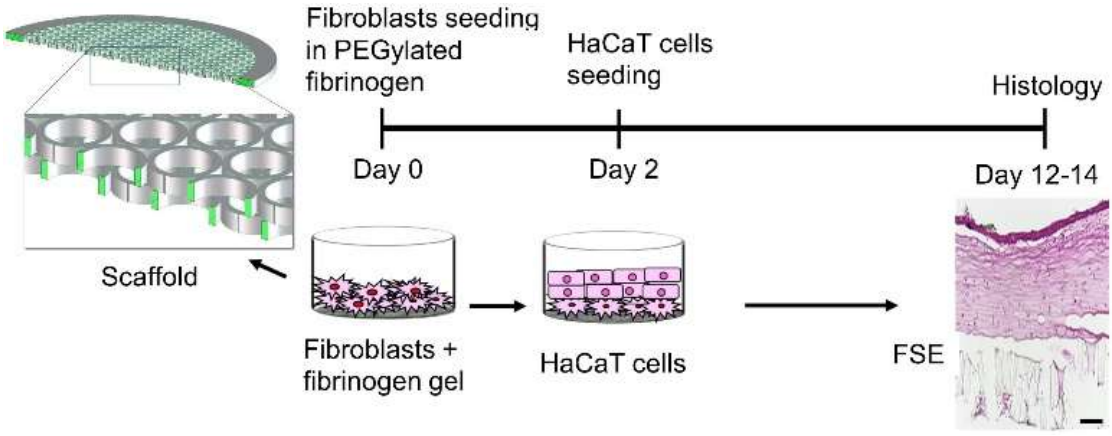

Figure 4.5: Schematic representation of FSE developing on the 2PP printed 3D scaffolds, including scaffold structure, cell seeding, and FSE histology. Scale bar: 200 µm. The development of FSE on 3D photo-printed polymeric scaffold and its histology is depicted in this Figure 4.5.

To generate biomimetic human skin model for more predictive and relevant human skin research, 3D FSE has been developed by using primary human fibroblasts and HaCaT cells on 3D scaffolds printed with two photon printing laser system as shown in Figure 4.5. The mixture of human primary fibroblasts in fibrinogen gel laid on two-layer scaffold as shown in Figure 4.5 was capable to support HaCaT cell layer seeded on the top to develop FSE. The resultant FSE is highly differentiated and closely mimic architecture of human skin as shown in Figure 4.5 [206]. 3D polymeric scaffold provides instructive template for *in-vitro* cell placement for tissue development with certain functional properties [207]. Histological analysis of FSE on 12th day of growth represented HaCaT cell layer on fibroblast fibrinogen gel layer on top of porous scaffold supporting required exchange of the nutrients between growth medium and FSE. After 12 days HaCaT cell-based layer has been developed at air-liquid interface to mimic native human skin morphology epidermis [206].

4.7 FS and OCT imaging of 3D tissues in maturation dynamics

Well-known methods of metabolic and morphological evaluation of tissue and 3D in vitro models like FSE are based on the immunoassay of the NADH/NADPH and FAD or other energy storing molecules from crude cell or tissue extracts and H&E-stained biopsies. Both approaches are damaging and lead to full destruction of expensive samples. To avoid this, we developed dual-mode OCT-FS system allowing contactless monitoring Fb+FG and FSE morphology and metabolism in the real time. Here we compared the morphology and metabolic activity at 7 to 14 day-olds of Fb+FG and FSEs. First, OCT imaging was deployed for non-invasive morphology assessment of 7- and 14-day old artificial dermis models [208].

Second, the metabolic activity of FSE, mitochondrial oxidative phosphorylation key cofactors, NADH/NADPH and FAD, were estimated with contactless FS system [209]. OCT images of 7 and 14 day-old demonstrate certain similarity of Fb+FG on scaffolds to FSE histology stained with H&E see in Figure 4.6 (a-c) and 4.7 (a-e), proving that OCT imaging has high potential in representing accurate dimensions of artificial tissues. First, with the help of OCT, we obtained images of the scaffold in the well plate without and with PBS Figure 4.6 (a,b). Next, we examined the Fb+FG morphology on days 7 and 14. Figure 4.6 (c,d) demonstrate the meniscus formation. In general, it can be concluded that Fb+FG is a low-scattering and weakly absorbing medium, which is emphasized by the presence of a scaffold on the image's bottom side. Figure 4.6 (e,f) also show NADH/NADPH and FAD fluorescence spectra measured from 7- and 14-day-old Fb+FG grown on the scaffold. The measurement results show that tissue growth leads to an increase in the level of NADH/NADPH fluorescence and a decrease in the level of FAD (up to 50-60%) (see also Figure 4.6 (g,h).

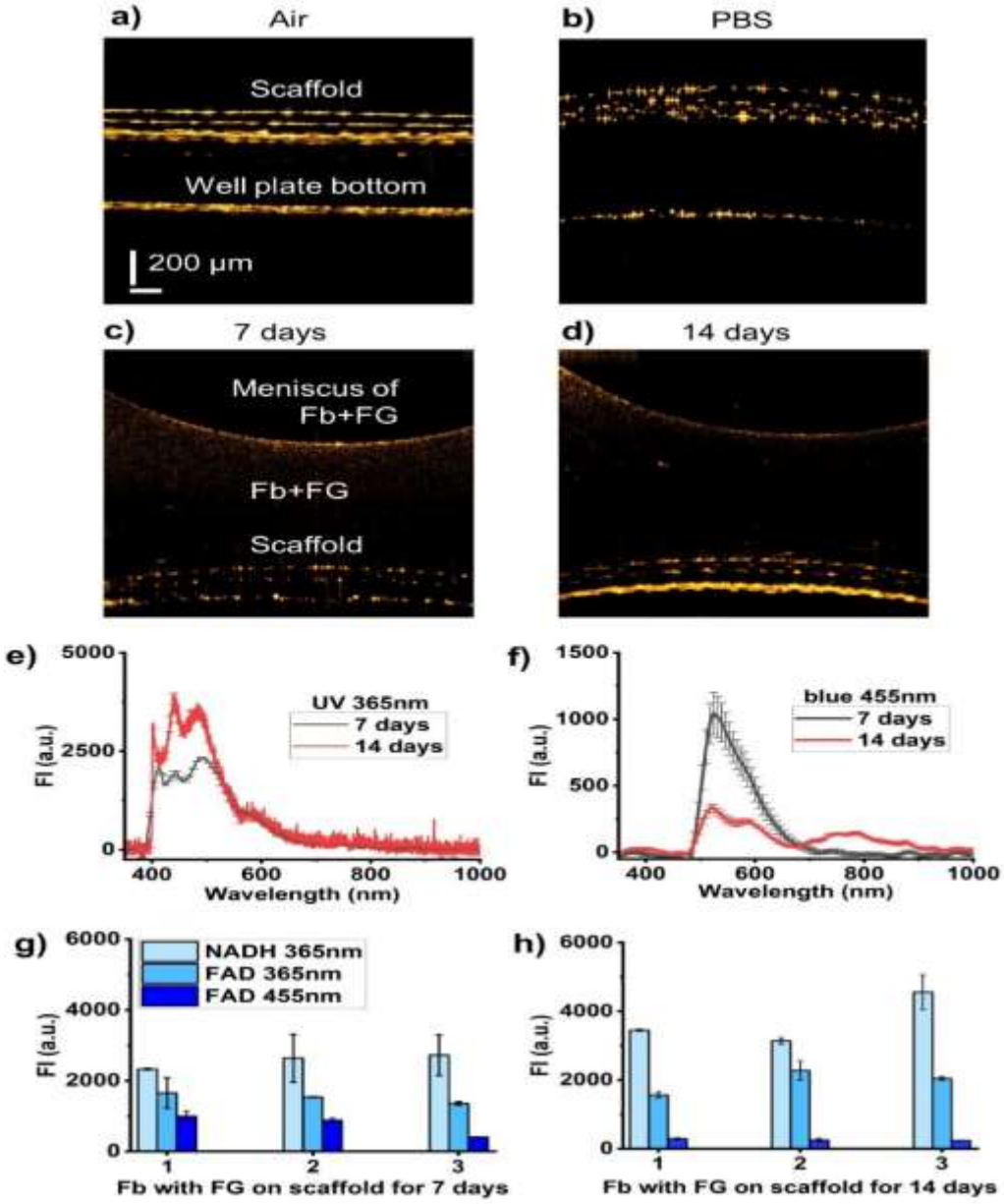

Figure 4.6: The FS-OCT system evaluated the metabolism and morphology of 3D Fb+FG on scaffolds. Representative OCT image of scaffold in the well plate (a) without and (b) with PBS, (c) 7-days-old Fb+FG and (d) 14-days-old Fb+FG. Scale bar: 200 µm. (e,f) Fluorescence spectra of 7 and 14 days of culturing of Fb+FG at 365 nm and 455 nm excitation, correspondingly. (g,h) Maximum FI of 7 and 14 days of culturing of Fb+FG at different excitation wavelengths. Data are presented as mean±SD (n=3,3D samples).

Based on our modelling data for real skin, it is assumed that the depth of light penetration into printed tissue may differ between 365 nm and 455 nm. The penetration depths for these wavelengths could be 300 µm and 500 µm, respectively [18]. Printed tissues are likely to exhibit deeper penetration while maintaining the same proportional relationship.

Morphological evaluation of fully developed FSE cultured for 7 and 14 days on different scaffolds (S1, S2, S3) showed a noticeable difference in the thickness of the layers of in

vitro-developed HaCaT cells (see Figure 4.7). In the first 7 days of cultivation, the HaCaT cells layer is practically undeveloped (Figure 4.7a, b). An additional 7 days of cultivation leads to a significant increase in the thickness of the top layer (Figure 4.7c-d).

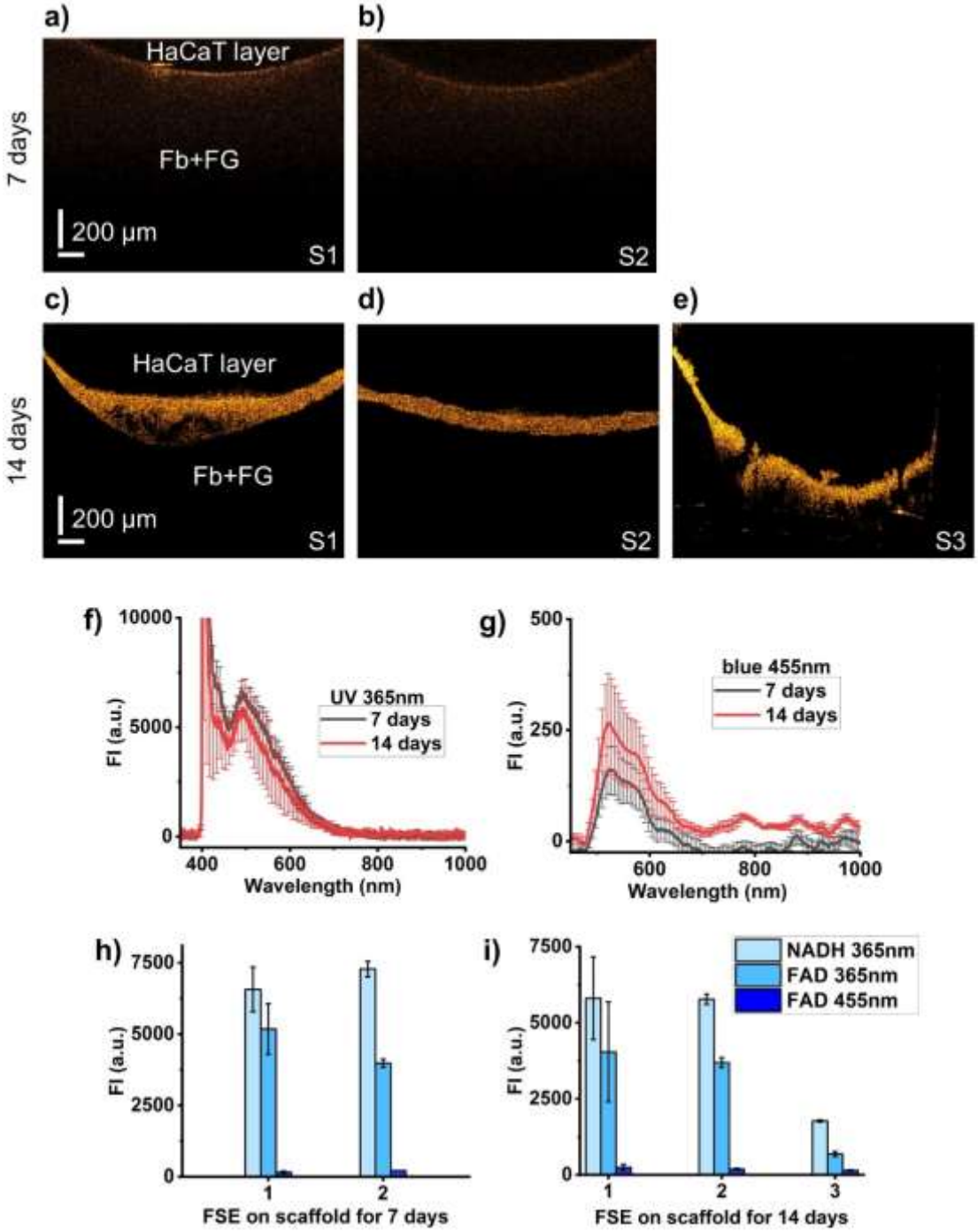

Figure 4.7: Metabolic and morphological evaluation of completed FSE after 7 and 14 days of culturing. (a, b) Representative OCT images of 7-day-old two FSEs (S1, S2). (c-e) Representative OCT images of 14-day-old three FSEs (S1, S2, S3). Scale bar: 200 µm. (f,g) Fluorescence spectra

of 7 and 14 days of culturing of FSE at 365 nm and 455 nm excitation, correspondingly. (h,i) Maximum FI of 7 and 14 days of culturing of FSE at different excitation wavelengths. Data are presented as mean±SD (n=3).

The layer of fibroblasts incorporated into the fibrinogen gel is located on the top of the scaffold and provides a base for the growth of HaCaT cells, like the epidermis of real skin. The layer of HaCaT cells has been detected through a highly backscattered area of the constructed FSE. According to H&E histology (Figure 4.5), the thickness of the HaCaT layer is ~150 μm. This corresponds to the values of the thickness of the HaCaT layer obtained from OCT measurements. The thickness of the layer developed from HaCaT cells for S1 (Figure 4.7c) is ~200 μm. In S1, the diffuseness and some defects of the HaCaT cell layer can be observed. In Figure 7d (S2), the developed FSE model is more stratified and cultured homogeneously as compared to the thickness of cells developed in S1 and S3 (Figure 4.7e). In S3, raptures and inconsistency of the HaCaT layer are observed. The thickness of the model developed in S2 is ~90 μm and in S3 ~180 μm.

The most remarkable observation was that OCT clearly revealed differences in HaCaT cell layer shapes on individual FSE samples Figure 4.7 (a-e), proving that morphology OCT imaging is a powerful approach to evaluating deviations in the development of FSE.

The difference between Figures 4.6(a) and 4.6(b) arises from the presence of PBS in sample 4.6 b. The variation between Figures 4.6(c) and 4.6(d) can be attributed to changes in system focus that often happens during OCT imaging. Despite this, all images were processed using consistent intensity thresholds. It is important to note that the post-fixation dehydration process inherent in the H&E staining protocol leads to a reduction in FSE tissues. The thickness of the FSE dermis can decrease by 68% due to the fixation procedure [23]. This contrasts with OCT imaging, which uses fresh, non-dehydrated FSE samples. Thus, our approach provides true information about sample sizes.

We also assessed cellular metabolic activity in FSEs after exposure to UV and blue light. The ORR for both 7- and 14-day-old FSE is not significantly different. Based on NADH/NADPH and FAD fluorescence measurements Figure 4.7 (f-i) the HaCaT cell layer in FSE is metabolically more active compared to the FI of Fb+FG. Insignificant fluctuations in ORR parameters (around 0.6 a.u.) for 7- to 14-day-old Fb+FG compared to FSE Figure 4.8

indicate that glycolysis, but not oxidative phosphorylation is dominant for the metabolism of both derma models [32].

Therefore, we think that the most reliable clues about the level of FSE development and maturation can be OCT morphology imaging demonstrating dimensions of the artificial epidermis and dermis layers and changes in the FI of NADH/NADPH and FAD.

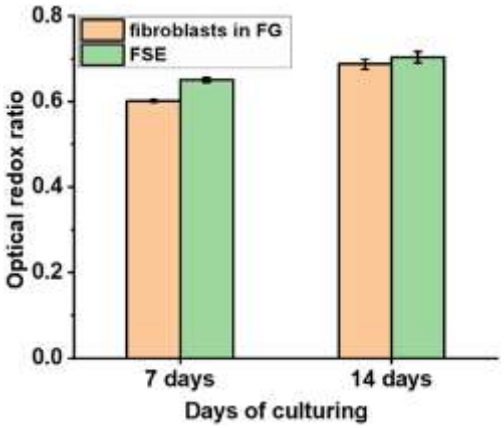

Figure 4.8: Optical redox ratio of Fb+FG and FSE for 7 and 14 days of culturing. Data is presented as mean±SD (n=3).

4.8 Melanoma-FSE development

After successfully developed FSE on 3D scaffolds, we tried to develop Melanoma-FSE by using the same technology to more accurately understand the early-stage human melanoma. After the completely populating the scaffolds with primary human fibroblasts in fibrinogen gel for 4 days, HaCaT cells and melanoma cells are grown on the top of the fibroblasts for 5 days. Histological analysis of the melanoma 3D skin equivalents demonstrates the morphology of the developed Melanoma-FSE after 9 days of culturing.

For the examination of skin cancer, specialists commonly use dermoscope but OCT magnifies the surface of skin lesion using infrared light [210]. For the detection of melanoma OCT is a promising technique. OCT provides architecture of skin at the depth of 0.5mm to 1.5mm and resolution 3μm to 15μm [211]. The depth of developed Melanoma-FSE is about 600μm, according to the Clark's level its level I melanoma where malignant melanocytes are confined in the epidermis and depth of invasion is less than or equal to 7500μm [52].

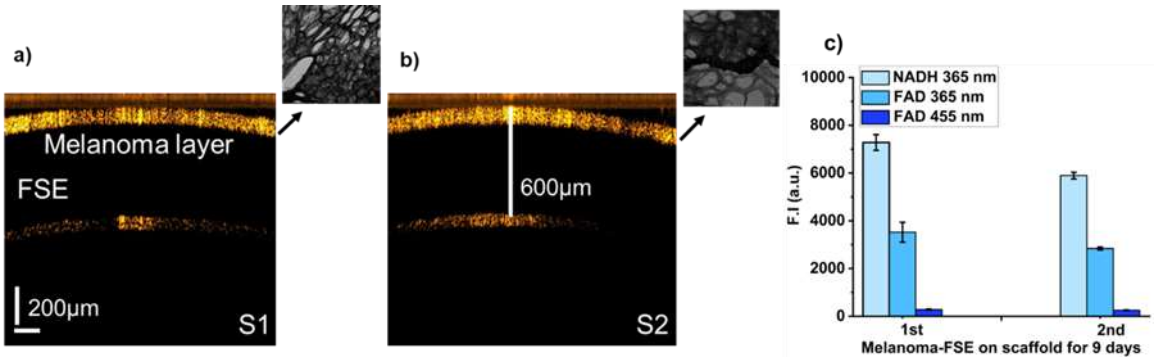

Figure 4.9: Metabolic and morphological evaluation of Melanoma-FSE after 9 days of culturing (a, b) Representative OCT images of 9 days old Melanoma-FSE (S1, S2). (c) Fluorescence spectra of Melanoma-FSE after 9 days of culturing at 365nm and 455nm excitation. Horizontal histopathological evaluation (H&E staining of melanoma skin), Scale bar 200µm.

The classification of melanoma on basis of histopathology, anatomical site, and degree of sun damage is divided into four sub types which are Superficial spreading melanoma (SSM), Lentigo Malinga Melanoma (LMM), Acral Lentiginous Melanoma (ALM) and Nodular Melanoma (NM). In histopathology, SSM is characterized by presence of enlarged melanocytes, often small aggregates or nests and usually scatter in epidermis and migrate upward abnormally called pagetoid(upward) spread [212]. Our histopathological results present superficially spreading pattern of melanocytes with notable enlargement and nests formation and these changes covered the HaCaTs and underlying Fb+FG as well. OCT provides information about the development of stage I melanoma in FSE, and histological analysis reveals the cytological features and superficial spreading of melanoma in FSE. We also assessed cellular metabolic activity in Melanoma-FSEs after exposure to UV and blue light based on NADH/NADPH and FAD fluorescence measurements in (Figure c). It is assumed that fluorescence spectra are mostly form melanocytes as it spread and covered HaCaTs and Fb+FG.

4.9 Discussion

The optical pattern of skin depends upon the interaction of light wavelength with different layers of cells produced by cellular matrixes. OCT provides real shapes and dimensions of developed artificial skin models. OCT imaging can provide a measurable thickness of the developed epidermis layer formed by the HaCaT cell layer in FSE and reflect its structural defects of the scaffold, Fb+FG, and HaCaT cell layers [23], [41]. Since this research fucuses on assessment of the morphology not real human skin but FSEs which mostly consists of fibrinogen gel highly light transferable we used short wavelength OCT system with 840 nm laser.

The fluorescence spectra analysis revealed distinct patterns of FI shifts between UV- and

blue-excited emissions across the Fb+FG and FSE models. Specifically, the Fb+FG model demonstrated a notable sensitivity to UV excitation, which we attribute to its relatively simplistic structure and the inherent properties of the fibrin gel matrix. In contrast, the FSE model, which closely mimics the full thickness and complexity of human skin, exhibited a pronounced response to blue light excitation. These findings suggest that the structural composition and thickness of these two models significantly influence their metabolic fluorescence signatures. The FI shifts offer insights into the metabolic dynamics and biochemical composition of the models, reflecting their physiological relevance and potential applications in dermatological research. In the present study, it is assumed that HaCaT cells, fibrin-based dermal matrix and primary fibroblasts absorb incoming incident light. Since the penetration depth for UV and blue is about 200 μm and 400 μm respectively [42], [43] and the thickness of developed FSE is about 2 mm, it can be considered that fluorescence spectra are combined spectra from fibrinogen gel with fibroblasts and HaCaT cells. Our results show that FAD decreases with increasing the culturing time of fibrinogen gel while NADH/NADPH increases. For FSE, a low concentration of FAD was detected as compared to NADH/NADPH. The maximum fluorescence intensity of the S2 scaffold (FI^{S2}, Figure 7g) has the lowest SD values compared to FI^{S1} and FI^{S3}, where representative OCT images (Figure 7a-c) demonstrated high inconsistency and even raptures (S3) of HaCaT layers. HaCaT layer developed on scaffolds S1, S2, and S3 has distinguishingly different OCT shapes, and their corresponding FI values are also different. Therefore, the variation of FI^{S1} is more prominent than that of S2 and S3. This indicates that our OCT-FS system is sensitive enough to detect the peculiarity in the morphology and corresponding changes in metabolic activities of the artificially developed 3D scaffold FSE.

This optical characterization is not only helpful for the detection of healthy and unhealthy developed skin but also is a non-destructive and reliable method for metabolic assessment of 3D tissue models. For evaluation of our developed OCT system, OCT images of in vitro developed FSE are compared with H&E-stained histology along with developed FSE in a 3D scaffold. The dimensions of the fully developed FSE can trustfully be evaluated with OCT since its OCT image demonstrates a high similarity to the histological image of H&E-stained FSE.

This study has demonstrated the validity of our customized FS device combined with OCT imaging for non-damaging assessment of human HaCaT cells and fibroblasts metabolic. Maturation and morphology of FSE and Melanoma-FSE models grown on architecturally customised laser-printed 3D scaffolds. OCT also provides morphological images of the development of the fibroblasts within fibrinogen gel when growing on 3D scaffolds. Therefore, the dual-mode optical system can be considered highly verifying and sensitive

and can be used in the future for a full-profile assessment of the maturation and viability of 3D in vitro developed models of biological tissues. Second, the OCT module used for contactless evaluation of dimensions and morphological patterns of developing and developed FSEs demonstrated (i) high alikeness to H&E histology patterns, (ii) real skin dimensions, (iii) with the advantage of keeping growing FSEs intact from the first day of culturing to its full maturation. Thus, the dual mode FS/OCT system is an excellent way to study and monitor the metabolism and morphology of developing a 3D scaffolded tissue model *in-vitro*.

Chapter 5

Direct laser-induced treatment on human 2D and 3D melanoma tissue models

5.1 Introduction

Malignant melanoma is an aggressive form of skin cancer that originates form pigmentary cells called melanocytes present in skin and deaths related to skin cancer is about 79%. If melanoma is diagnosed at the early stage, then it can be cured by surgical resection. According to National Comprehensive Cancer Network (NCCN) the recommended treatment for local recurrence and stage III of melanoma are intralesional injection, radiation therapy, high-dose bolus interleukin-2 alone or with chemotherapy, biological therapy, immunotherapy and photodynamic therapy (PDT) [213], [214].

PDT is from of therapy in which light is absorbed by photosensitiser (PS) to produce reactive oxygen species (ROS) more specifically singlet oxygen ($^1O_2$) that are sufficient for killing the tumour cells. PS is not only absorbed by cancer cells but also absorbed by healthy cells and causes multiple concerns like sensitivity to intensive light to patients, high costs of PSs, low tissue penetration by activation light, high intrinsic toxicity. $^1O_2$ is less stable and electronically excited state of molecular oxygen ($^3O_2$). It can be produced by various ways like enzymatic, thermal, and photochemical activation of $^3O_2$ [145].

The recent development of quantum-dot (QD) laser diodes (LDs) emitting in near infrared (NIR) with emission wavelength around 1268 nm matches with absorption band of molecular oxygen. For generation of $^1O_2$ in tissues, 1262-1270 nm laser wavelengths are used. $^1O_2$ is electronically excited state of molecular oxygen and it is less stable as compared to molecular oxygen in ground state. This can cause production of free radicals, initiation of apoptosis, mitochondrial dysfunction in cancer cells through direct photoexcitation of molecular oxygen [150], [159], [161], [215].

Detection of intracellular $^1O_2$ is challenging due to short lifetime from few tens of nanosecond to microseconds and low concentration in mammalian cells. By using fluorescent probe 9,10-dimethylanthracene (DMA) and silicon-containing rhodamine (Si-rhodamine) moieties, called Si-DMA with high sensitivity, high spatial resolution and fast timing of response has been reported for purpose of detection of $^1O_2$ in living cells. Si-DMA can provide instantaneous response to intracellular $^1O_2$ by residing inside the mitochondria of cell [216], [217].

High spatial resolution refers to the ability of fluorescent probe Si-DMA to precise localization within subcellular structures [216], [218]. It is reported the production of $^1O_2$ in sufficient amount by laser irradiation at 1267nm and 1270nm that can cause induction of apoptosis in cancer cells [138], [159].

In multicellular organisms, homeostatic cell death, called apoptosis, is balancing by regulating the rates of cell division and death. For orderly removing of dead cells, apoptosis is the preferred form of cell death, while necrosis is unregulated form of cell death [219]. In cancer, balance between cell apoptosis and proliferation shifts in favour of proliferation of cells and this activates the uncontrolled growth of tumour. For promotion of apoptosis in cancer cells, it is urgent need to develop anticancer therapies selectively for killing of cancer cells and safe for healthy cells. For monitoring apoptosis and assessment of anticancer drugs efficacy, various non-invasive sensing and imaging techniques are utilized [166].

Apoptosis is triggered by main pathways intrinsic and extrinsic. During extrinsic pathway also known as death receptor pathway, TNRF (Tumour necrosis Factor Receptor) is activated and located on the outer membrane of cell while intrinsic pathway also known as mitochondrial pathway is initiated by internal disturbance like DNA damage, cellular stress, mitochondrial dysfunction. During the early stages of apoptosis, PS flipped out form the inner layer to the outer layer of cell membrane. To study apoptotic events different methods are used, detection of PS on the extracellular plasma membrane by using PS binding proteins called annexin V [163], [166].

In the initiation of intrinsic apoptosis also known as mitochondrial apoptosis pathway ROS play a critical role. ROS play an important role in cell signalling and regulate apoptosis in cells mediated by mitochondria, death receptors and endoplasmic reticulum. During apoptosis increment of ROS has been reported for cancer cells and this increment of ROS is triggered by therapies [220] [221].

Here we studied direct optical excitation of $^1O_2$ through 1267 nm laser wavelength without photosensitizer and its effect on cancerous and non-cancerous human skin cells. To minimize the thermal damage on cells caused by laser irradiation, we have used perfusion chamber for performing temperature-controlled experiments. We investigated real time monitoring of production $^1O_2$ and its effects on cancer and healthy cells 2D models. We found it caused the initiation of apoptosis in melanoma cancer cell line as compared to the primary human fibroblasts and HaCaT cells. Additionally, we tried to be optimized optical dose to induce apoptosis in cancer cells while minimize effects on healthy cells.

5.2 Temperature control system during laser irradiation for 2D cell culture

It consists of three major parts which are as follows.

- Laser setup
- Perfusion system for laser illumination
- Pump

5.2.1 Laser setup

Temperature control system during the laser irradiation for 2D cell culture is shown in Figure 5.1. Laser diodes are used as source of irradiation at wavelength1267 nm. A specially made quartz optic fibre cable is used to carry out the laser energy from source to the object. In 400-2000nm spectral range, the cable transmits light with little signal attenuation and numerical aperture of NA=0.22 ± 0.02. After fibre optic cable, a collimator (F280FC-C, Thor labs Inc., Molandal, Sweden) is installed to create a parallel laser beam. The laser beam diameter at the collimator output is 3.4 mm. The laser irradiation absorbed by the biological tissue known as surface dose (energy density) is calculated by the following formula.

$E = P \times t/S$

P= average power output (Watt)

T= exposure time (sec)

S= laser spot area (cm^2) [222]

5.2.2 Perfusion system for laser illumination

Perfusion chambers have great importance in cell biology research for real time monitoring of cellular responses through live cell imaging [223]. For performance of experiments at constant temperature during laser irradiation, we have used perfusion system RC-26G (Warner instruments) and its water flow channel related to pump so that a constant flow of DPBS at 24^{o}C flowed through the chamber for maintenance of temperature and reduce the thermal effects during laser illumination.

5.2.3 Laser irradiation and imaging of skin cells

Fluorescence measurements were taken using fluorescence microscope (Leica DMi8, Germany). Cell viability is evaluated after 2 min of laser irradiation with Annexin V (FITC) and propidium iodide (PI). After 2 min of laser irradiation, cells on are incubated with fluorescent dye for 5 min and then wash with DPBS and taking image of apoptotic and dead cells. Singlet oxygen produced by laser irradiation is determined by using Si-DMA.

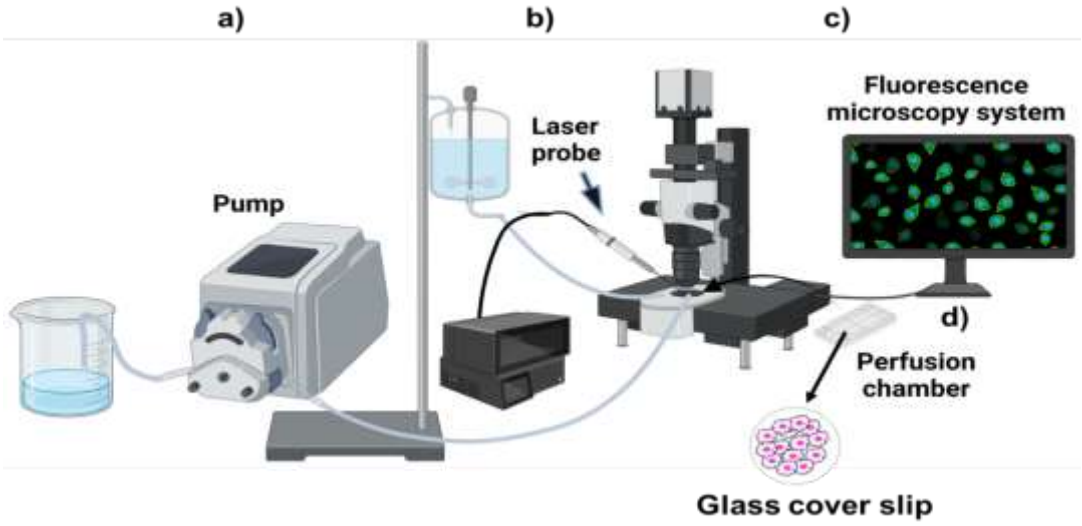

Figure 5.1: Overview of experimental setup a– pump, b – 1267nm laser irradiation system with probe, c – fluorescence microscopy system, d– cell culture chamber for laser irradiation.

5.3 Measurement of temperature inside perfusion chamber

The measurement of the temperature of perfusion chamber before during and after the laser interaction at the different intensities with DPBS flowing at the rate of 12 ml/min in perfusion chamber is shown in this Figure 5.1. The temperature is measured with TC-08 thermocouple data logger-Pico Tech. The Figure 5.2 represents the maximum increase of temperature of the cell culture chamber containing DPBS after interaction with laser light at different intensities from 50 mW to 300 mW. After 2 minutes of laser interaction at different intensities, temperature of chamber is increased 1°C for the highest intensity 300mW of laser interaction with continuous flow of DPBS inside the chamber.

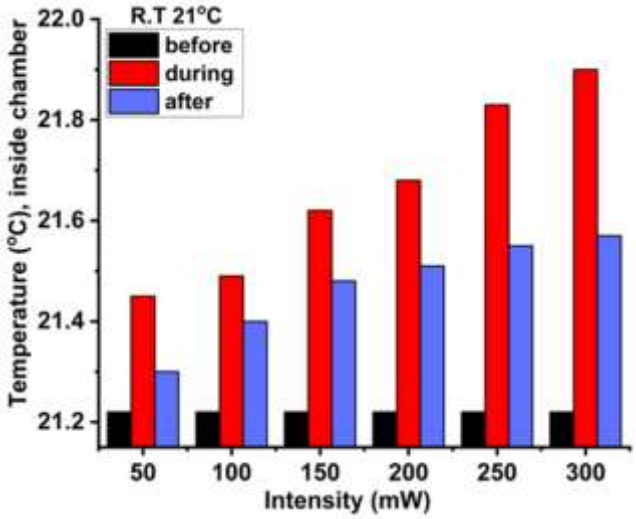

Figure 5.2: Measurement of temperature of cell culture chamber before, during and after laser irradiation(n=3).

5.4 Singlet oxygen production by 1267nm laser irradiation

We used Si-DMA as indicator for detection of singlet oxygen by 1267 nm laser irradiation at 200mW after 2 min in melanoma, primary fibroblasts, and HaCaT cells as shown in Figure 5.3. It is reported that phosphorescence signals at 1270 nm for $^1O_2$ are weak due to low emission intensity, therefore its necessary to choose fluorescence probe with high sensitivity, fast response time, high spatial resolution. One of the advantages of Si-DMA as compared to other real-time probes is that it allows detection of mitochondrial $^1O_2$ more specifically at subcellular level. This is due to Si-rhodamine component in Si-DMA selectively accumulates in mitochondria and this can react with the $^1O_2$ generated in mitochondria [216]. From our results, we observed that melanoma cells exhibited the highest fluorescence intensity for singlet oxygen detected by Si-DMA as compared to primary fibroblasts and HaCaT cells after 1267 nm laser irradiation.

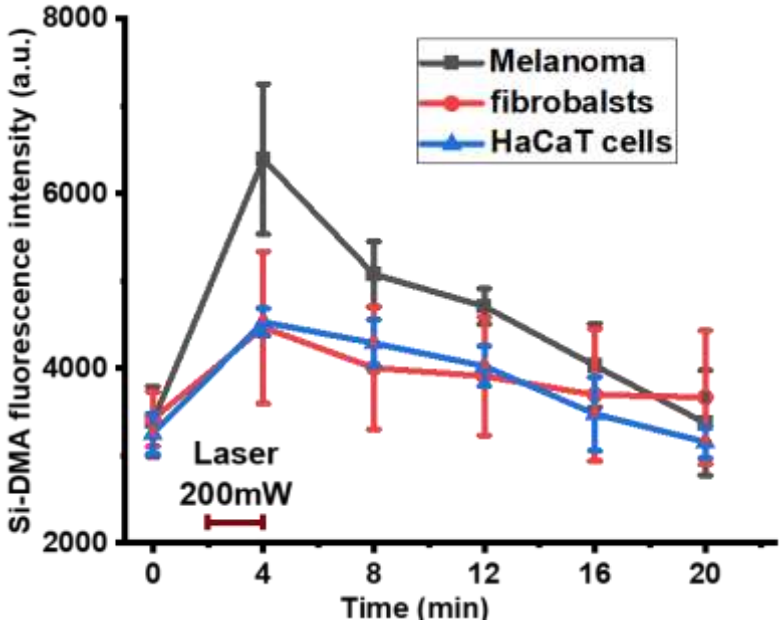

Figure 5.3: Singlet oxygen production by 1267 nm laser irradiation in melanoma, primary fibroblasts, and HaCaT cells. Intensity profile of Si-DMA (as singlet oxygen detection probe) in melanoma cells, primary fibroblasts, and HaCaT cells upon 1267nm illumination for 2 minutes at energy 200mW (n=5).

From Figure 5.3 it is revealed that highest fluorescence intensity for Si-DMA has been detected for melanoma cells as compared to primary fibroblasts and HaCaT cells after laser interaction for 2 min at 200mW. The fluorescence intensity for Si-DMA in melanoma cells reached approximately 6200 a.u., whereas in HaCaT and fibroblasts, it was around 4200 a.u. immediately after laser interaction with cells for 2 minutes. The generation of $^1O_2$ in melanoma cells after laser interaction at 1267 nm is detected by Si-DMA as shown in the

following Figure 5.4, cells are first swelled immediate after laser interaction at 4 min and then start shrinking after 16 min.

The size of cell is changing from 233.3 μm^2 to 156.5 μm^2 after laser interaction. Swelling of cells immediately after laser interaction and then followed shrinkage can be due to photoinduced disruption in cell membrane, it caused changes in membrane permeability due to generation of membrane defects and pores and then shrinkage accompanied by membrane blebbing and indication of apoptosis [163], [224].

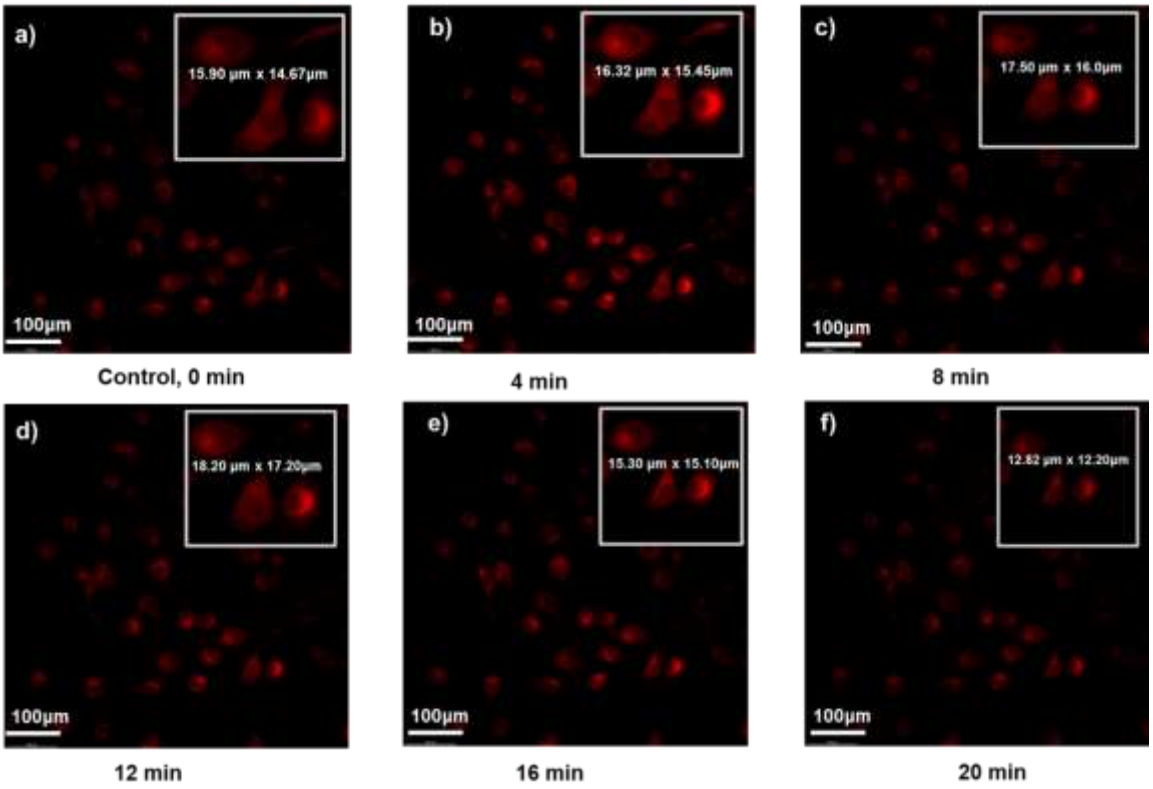

Figure 5.4: Representative fluorescence images of 2D melanoma cell culture illustrating the effect of singlet oxygen produced by 1267nm laser irradiation for 2-min at 200mW detected by Si-DMA a) control without laser irradiation b) after 4 minutes, c) after 8 minutes, d) after 12 minutes e) after 16 minutes, and f) after 20 minutes of laser irradiation.

5.5 1267nm laser irradiation induction of apoptosis and necrosis

The detection of singlet oxygen production during the 1267 nm laser irradiation has significant effects on cells. These results demonstrate that 1267nm laser at 200 mW for 2 minutes of interaction with non-melanoma and melanoma cells can induce apoptosis in cancer cells while spare healthy cells. To prevent apoptotic thermal damage, the temperature in the perfusion chamber was controlled with flow of DPBS during the NIR 1267nmlaser irradiation. The Figure 5.5 represents clear image of apoptotic and necrotic cells after interaction of 2D culture melanoma cells with laser light and incubation with

annexin V and PI. In Figure (a) represents the bright filed image of melanoma cells without laser interaction and incubation. In Figure (b)10 minutes of after laser interaction and incubation with annexin V and PI, cells are shrinking, and their shapes change into round shape.

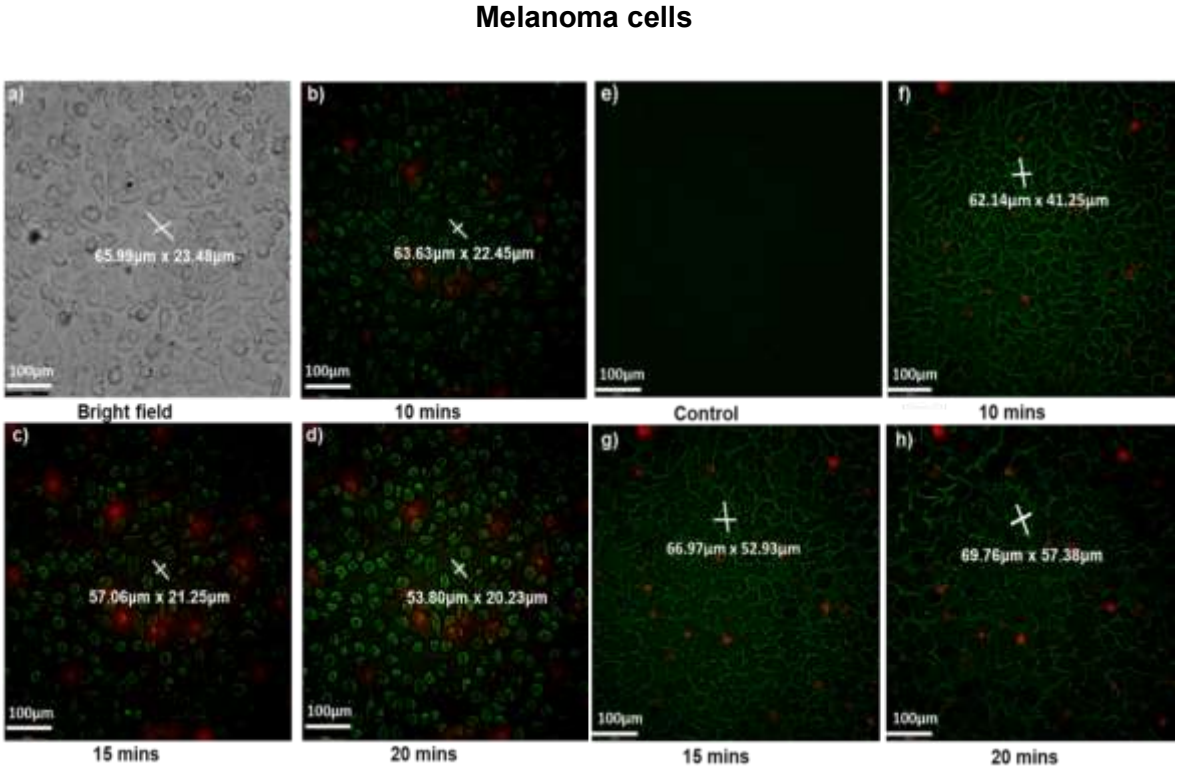

Figure 5.5: Representative fluorescence images of 2D cell culture illustrating the effect of 1267nm laser-induced apoptosis and necrosis at different stages in human melanoma cells, stained with Annexin V-FITC and Propidium Iodide a) bright field b) after 10 minutes, c) after 15 minutes, d) after 20 minutes, e) control without laser irradiation, f) after 10 minutes , g) after 15 minutes, h) after 20 minutes of laser irradiation.

Morphological changes in cells during apoptosis are due to chromatin condensation and nuclear fragmentation in nucleus caused rounding up of cells and reduction in cellular volume [163]. Apoptotic cells are identified based on their morphology including retraction and rounding of cells, plasma membrane blebbing, nuclear fragmentation, cytoskeleton disintegration and formation of apoptotic bodies [219], [225]. From Figure 5.5 (a) to Figure (d) size of the cell is shrinking form 4867.73 μm^2 to 3419.23 μm^2. Figure 5.5 (e) represents the control without laser illumination but incubated with annexin V and PI. Figure 5.5 (f), (g), and (h) presented the apoptotic effect of cells after 10, 15 and 20 minutes of laser interaction. The cells are becoming round, and size of cell is increasing form 8052.77 μm^2 to 12575.26 μm^2. As necrotic cells are attributed as leakage of cellular contents due to

integrity of cell membrane are indicated by the red signs as PI is absorbed by the cellular fragments, which are considered as late apoptotic cells [226].

We used Annexin V-FITC and propidium iodide to detect the apoptotic and necrotic human melanoma cells, HaCaT cells, and primary human fibroblasts after laser irradiation at 1267nm with 200mW for 2 minutes. It is revealed form the Figure 5.6 that, HaCaT cells after the interaction with laser did not have any apoptotic effect while some cells died and indicated as red sign as PI is absorbed by the nucleus of dead cells.

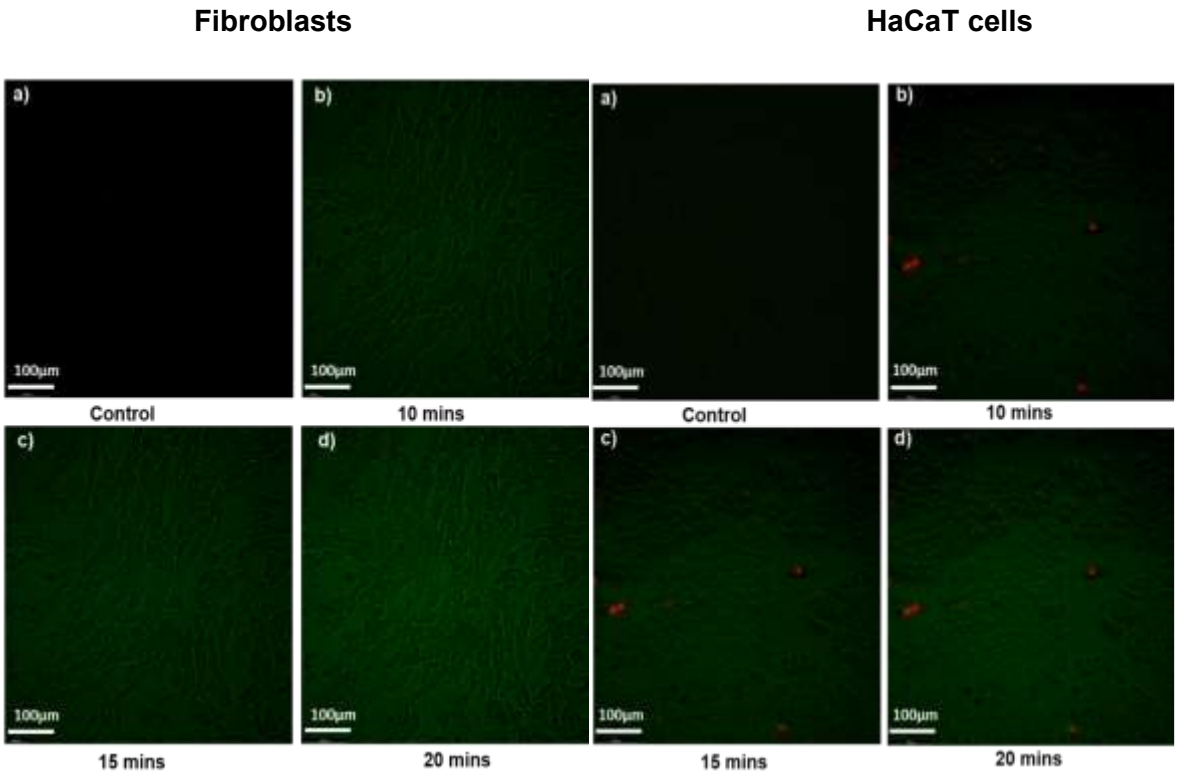

Figure 5.6: Representative fluorescence images of 2D cell culture illustrating the effect of 1267nm laser-induced apoptosis and necrosis in fibroblasts and HaCaT cells, by using Annexin V-FITC and PI a) control without laser irradiation b) after 10 minutes, c) after 15 minutes, d) after 20 minutes of laser irradiation.

Fibroblasts after laser interaction and incubation with annexin V and PI presented no effect of laser on cells there are no dead cells but apoptotic cells few appeared after 20 minutes of laser illumination as shown in Figure (d).

The fluorescence intensity of apoptotic and necrotic cells in the Figure 5.7, represents that (a) melanoma cells exhibit high fluorescence intensity as compared to (b) HaCaT cells and (c) fibroblasts. Fluorescence intensity for apoptotic cells for fibroblasts is low as compared to melanoma and HaCaT cells.

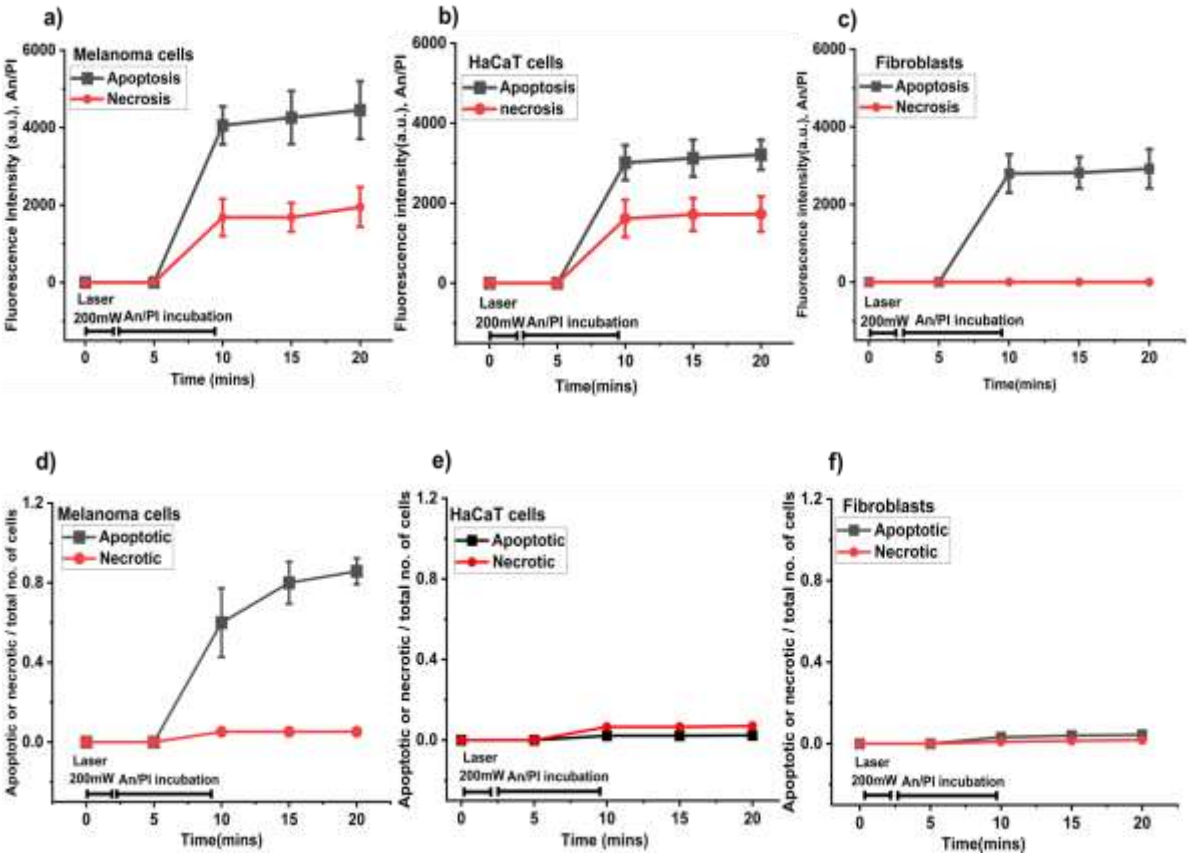

Figure 5.7: Fluorescence and quantification of apoptotic and necrotic cell fractions to total cell number. Fluorescence intensity from apoptotic and necrotic (a) melanoma cells, (b) HaCaT cells and (c) fibroblasts upon 1267nm illumination for 2 minutes at energy 200mW and after 5 min of annexin V/PI incubation. Statistical analysis of apoptotic and necrotic cells to total number of cell count is presented for (d) melanoma cells, (e) HaCaT cells, and (f) fibroblasts. (n=5)

It presents the binding of Annexin V-FITC to PS exposed on the cell surface after laser interaction or to DNA in apoptotic cells [166]. The results indicate that apoptotic and necrotic melanoma cells exhibit very prominent response after laser exposure, while for the fibroblasts the response for necrotic cells after laser illumination is almost negligible. Form statistical analysis it is further revealed that number of apoptotic and necrotic cells for melanoma samples is significantly higher as compared to the HaCaT and fibroblasts under same laser illumination including time and power as shown in Figure (d). Form Figure (e) and (f), it is revealed that number of apoptotic and necrotic cells following laser irradiation is minimal for both healthy cell types, HaCaT and fibroblasts.

5.6 Discussion

In the current study, we have studied the photochemical effect of laser after interaction with human non-melanoma and melanoma skin 2D cultures. This work presented the effect of

1267 nm laser illumination on 2D cultures of human melanoma, fibroblasts and HaCaT cells. 1267nm laser has been chosen because of its highly selective production of $^1O_2$ as compared to other ROS such as superoxide anion, hydrogen peroxide [159]. 1267nm laser wavelength can induce photothermal and photochemical effect after interaction with cells and tissues. Thermal effects can induce reversible and irreversible changes in tissues and cause reduction in viability of cells [153]. It is also reported that NIR cannot only cause the increase in ATP production in primary fibroblasts but also it can interact with the ultra-thin layer of water and deliver small amount of vibrational energy to water molecules without raising temperature [227]. To minimize the photothermal effect after laser interaction with cells, perfusion chamber for laser interaction with cells seeded on glass cover slips is utilized.

First, we detected the singlet oxygen by using Si-DMA in human melanoma, primary fibroblasts and HaCaT cell culture after laser interaction at 1267nm. Si-DMA is a red fluorescent probe having good cell permeability, contained rhodamine as chromophore and anthracene moieties as $^1O_2$ reactive site with selective localization in mitochondria and having negligible self-oxidation due to photoirradiation. The fluorescence of this dye enhances 17 times in the presence of $^1O_2$ due to formation of endoperoxide at the anthracene moiety [217].

Increase in Si-DMA fluorescence intensity for melanoma cells after laser interaction as compared to its control at 0 min is clear indication of singlet oxygen as it is reported that fluorescence of this dye is increased 17 times due to presence of $^1O_2$. Due to effect of $^1O_2$ the size of melanoma cells started to increase after the NIR laser interaction and then after a few minutes cells were shrinking. It was the clear indication of classic cell apoptosis due to $^1O_2$ oxidative effect in the melanoma cells as shown in Figure 5.3.

The increased non-enzymatic production of singlet oxygen in melanoma cells compared to non-cancerous cells may result from their elevated metabolic activity and higher mitochondrial respiration that leads to compromise antioxidant defence system [215], [228]. Additionally, melanoma cells exhibit alter mitochondrial membrane potential ($\Delta\Psi m$) that is associated with capacity of ATP production. It is reported that 1267 nm laser interaction can cause changes in ($\Delta\Psi m$) of melanoma cells as compared to healthy cells via the opening of mitochondrial permeability transition pore (PTP). This mitochondrial stress can cause the generation of ROS including singlet oxygen in melanoma cells [159].

In cells, when formation of ROS is dysregulated and exceeds the capacity of protective glutathione pool, oxidative stress exceeds the capacity of cell repair mechanisms, leading to biomolecules oxidation including lipids, proteins, and DNA, then general oxidative damage occurs. Elevated ROS induce oxidative cell death in cancer cells, and it provide promising possibilities to target and destroy cancer cells through various pathways like ferroptosis, apoptosis, necrosis, oxeiptosis and pyroptosis. while preserving healthy cells [229], [230].

It is observed from Figures 5.5 that production of $^1O_2$ by 1267 nm laser irradiation in melanoma induced oxidative stress that caused apoptosis in melanoma cells but not in non-melanoma cells. It is assumed that this triggering of apoptosis in melanoma cells is due to mitochondrial permeability transition pore (PTP) opening only in cancer cells [159], [161], [231]. It is reported that direct generation of $^1O_2$ can increase the mitochondrial membrane potential, activation of NADH and FADH-dependent respiration in primary neurons and astrocytes. The cellular mitochondrial respiration further stimulated the production of adenosine triphosphate (ATP) in the cells [145], [161]. The effect of $^1O_2$ on primary fibroblasts and HaCaT cells aligns from previous findings, which illustrated that $^1O_2$ can cause the increase in ATP production in non-cancer cells.

It is clear from Figure 5.5, 5.6 and 5.7, the generation of $^1O_2$ induced apoptosis in melanoma cells but not in healthy cells. In healthy cells, phosphatidylserine (PS) is located on the inner leaflet of plasma membrane. The NIR laser irradiation induced the significant increase of the cytosolic Ca^{2+}[215], due to calcium leak from damaged mitochondria. This elevated cytosolic Ca^{2+} led to PS moving from inner to outer leaflet of plasma membrane and this process is called phospholipid scrambling [232] indicated with Annexin V-FITC.

From Figure 5.6, it is assumed that fibroblasts and HaCaT cells are not apoptotic but still exhibit low fluorescence for Annexin V/PI as compared to melanoma cells after 1267nm laser interaction, it can be due to changes in membrane. Cells start repairing and PS transfer to the outer leaflet of cells and captured by Annexin V. So, the fluorescence for non-cancerous cell lines is assumed due to membrane dynamics instead of apoptosis.

The real time monitoring of $^1O_2$ and its positive effect on healthy cells as compared to its effect on melanoma cancer cells, can be used as potential treatment to optimize dosage for skin cancer. This approach can minimize the cytotoxic effect produced because of photosensitizing agents in conventional PDT.

Chapter 6

Conclusions and future work

In the first part of our research, we validate a reliable OCT/FS system for the purpose of detection between non- and cancerous cells and tissue samples. We also developed 3D tissue models on 2PP 3D printed scaffolds with high biomimetic features of the non- and Melanoma FSEs for minimizing the need of animal testing as in pre-clinical studies.

In this part, we have demonstrated the validity of our customized FS device combined with OCT imaging for non-damaging metabolic assessment of human HaCaT cells, fibroblasts and morphology of fibroblasts within fibrinogen gel, FSE and Melanoma-FSE models grown on laser printed 3D scaffolds. We provide a non-damaging method for evaluating 3D models maturation with our custom- build OCT-FS system. First, we demonstrated that FS module sensitivity estimated on NADH/NADPH and FAD fluorescence in solutions corresponded to the endogenous concentrations of these coenzymes measured in living tissues. Our system provides changes in metabolic assessment of cell types in 3D models by using both UV and blue light excitation. Thus, dual mode FS/OCT system is an excellent devise to study and monitor metabolism and morphology of developing 3D model in vitro without any preparation and fixation of sample and it can be useful for testing new cosmetics and drugs on human cell based. It is an affordable photonics approach for detection of healthy and unhealthy tissue samples.

In the second part of our research work, our aim is to develop PS-free technology having deep tissue penetration by 1267nm irradiation, reduction of cytotoxic effect on healthy cells and tissues due to use of photosensitizers as very common in PDT and more specifically in our case, to resolve the issue of high melanin absorption in melanoma cells associated with visible light in PDT.

In this study, we have designed temperature-controlled experiments to minimize the thermal effects of 1267 nm laser irradiation on cells. We demonstrated the direct optical excitation of singlet oxygen through 1267 nm laser irradiation in skin cancerous and non-cancerous cells without any using of photosensitizer and detected through Si-DMA. Our results reveal that highest Si-DMA based fluorescence intensity of singlet oxygen has been detected for melanoma cells as compared to the human HaCaT cells and primary fibroblasts 2D models. Various studies illustrated about selective cytotoxic effects of $^1O_2$ more specifically for cancer cells as compared to healthy cells. Our results revealed the induction of apoptosis and necrosis of human non-cancerous and cancerous 2D models detected by using

Annexin V and PI induced due to PS-free produced $^1O_2$. It is shown form our results that $^1O_2$ can induce apoptosis in cancer cells while sparing the healthy cells. It is a key tool for specifically generation of $^1O_2$ without PS and can be implemented in phototherapy for inducing apoptosis in tumour specific cells.

Preliminary results for future work

It's our main target that $^1O_2$ can lead the induction of apoptosis in cells and tissues. In 2D cell cultures effects of laser is more uniform but less representative as compared to effect on 3D tissues models. For comprehensive analysis of $^1O_2$ effect on 3D tissues, we have developed cancerous tissue models by using 3D printed scaffolds through two different culturing methods as shown in Figure 6.1.

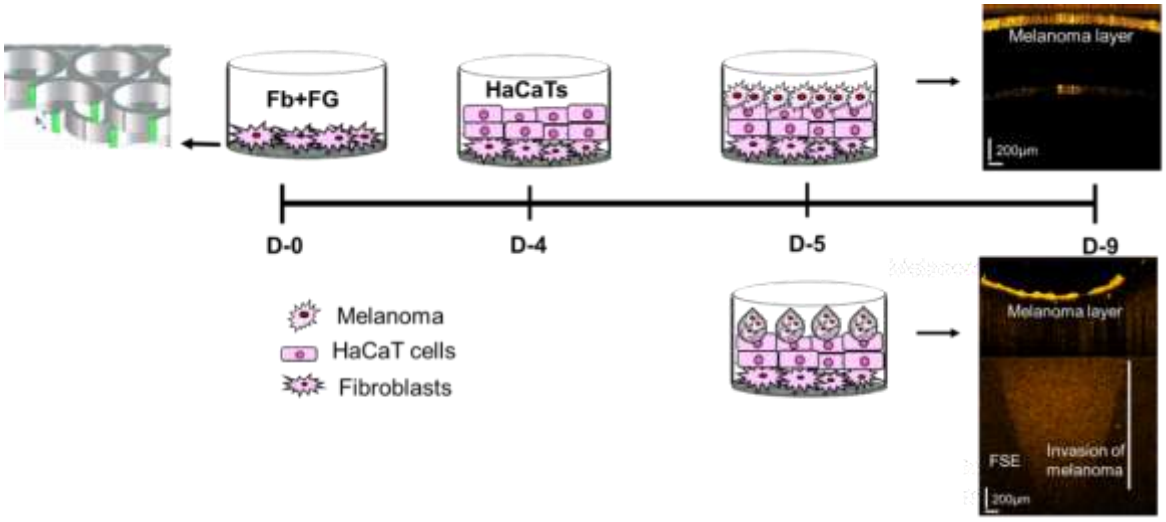

Figure 6.1: Schematic representation of Melanoma-FSE developing on the 2PP printed 3D scaffolds, including scaffold structure, cell seeding, and OCT images of Melanoma-FSE. Scale bar: 200 µm.

In first method, after the completely populating the scaffolds with primary human fibroblasts in fibrinogen gel laid on two-layer scaffold for 4 days, melanoma cells are grown on the top of the fb+FG for 5 days prior to incorporation of HaCaT cells. In 2nd method, melanoma cells are grown on the top of fb+FG for 5 days in the form of droplets Prior to incorporation of HaCaT cells. OCT images revealed the difference between thickness of melanoma layer developed by different methods of culturin

Laser irradiation and temperature control system for 3D models

3D tissue models have been developed in scaffold in 6-well plate and treated by using NIR laser 1267 nm from the top of the lid to keep the samples contaminated free. In Figure 6.2

(c), optical absorption spectra of 6-well plate lid have been measured with Lambda 1050 UV/VIS/NIR (Perkin Elmer) spectrometer.

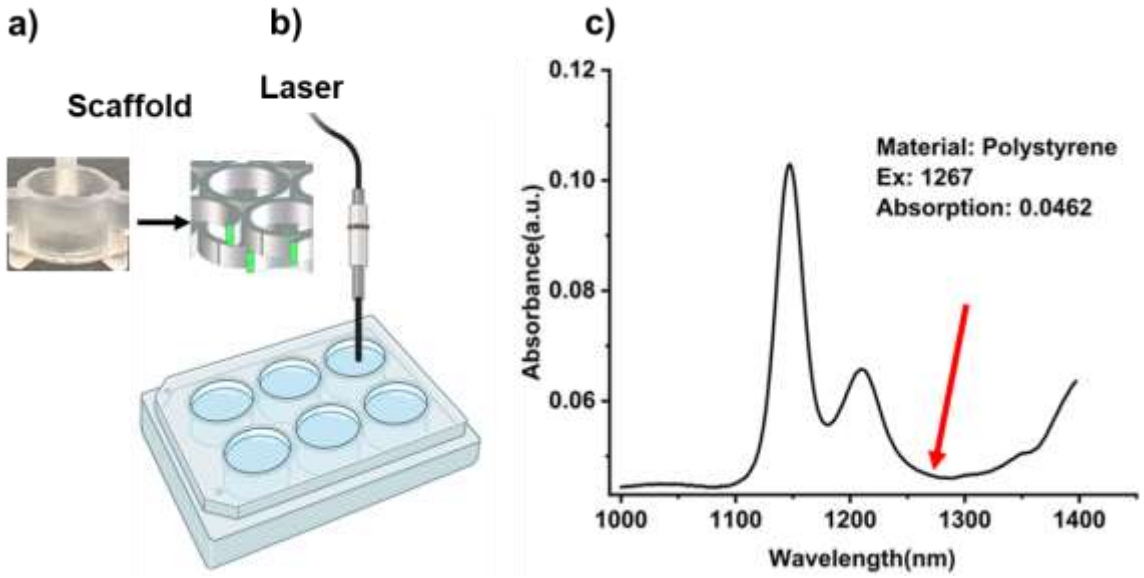

Figure 6.2: Overview of experimental setup a– scaffold, b – 1267nm laser irradiation probe, c – absorbance spectra of Polystyrene.

Table 6.1 : Accumulated doses of 1267nm laser irradiation for Melanoma-FSE samples.

Samples	Sample 1	Sample 2	Sample 3
Exposure Time	2 minutes	4 minutes	6 minutes
Dose	237.6 J/cm^2	475.3 J/cm^2	712.9 J/cm^2

Temperature measurement of fb+FG inside scaffold

The measurement of the temperature fb+FG in scaffold inside 6-well plate before during and after the laser interaction at the different intensities with DPBS inside well of 6-well plate is shown in this Figure 6.2. The temperature is measured with TC-08 thermocouple data logger-Pico Tech. This Figure represents the maximum increase of temperature of fb+FG in scaffold inside well of 6-well plate containing DPBS after interaction with laser light at different intensities from 50 mW to 300 mW. After 2 minutes of laser interaction at different intensities, temperature of chamber is increased 2^{o}C for the highest intensity 300mW. Then wait for 2 minutes and temperature goes down as shown in Figure 6.3 after laser interaction.

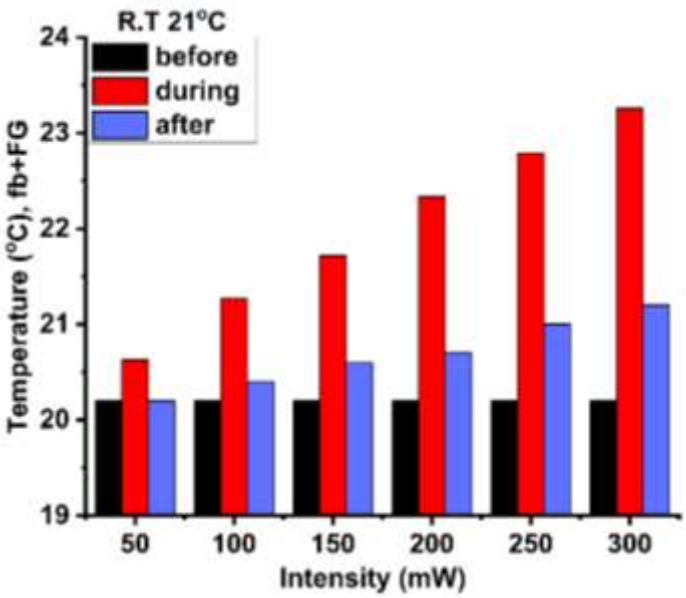

Figure 6.3: Measurement of temperature of fb+FG in scaffold inside 6-well plate before, during and after laser irradiation (n=3).

FS and OCT imaging of 3D Melanoma-FSE of 9 days before and after 1267nm laser irradiation

Metabolic and morphological evaluation of the developed Melanoma-FSE for 9 days on different scaffolds (S1, S2, S3) is shown in Figure 6.4.

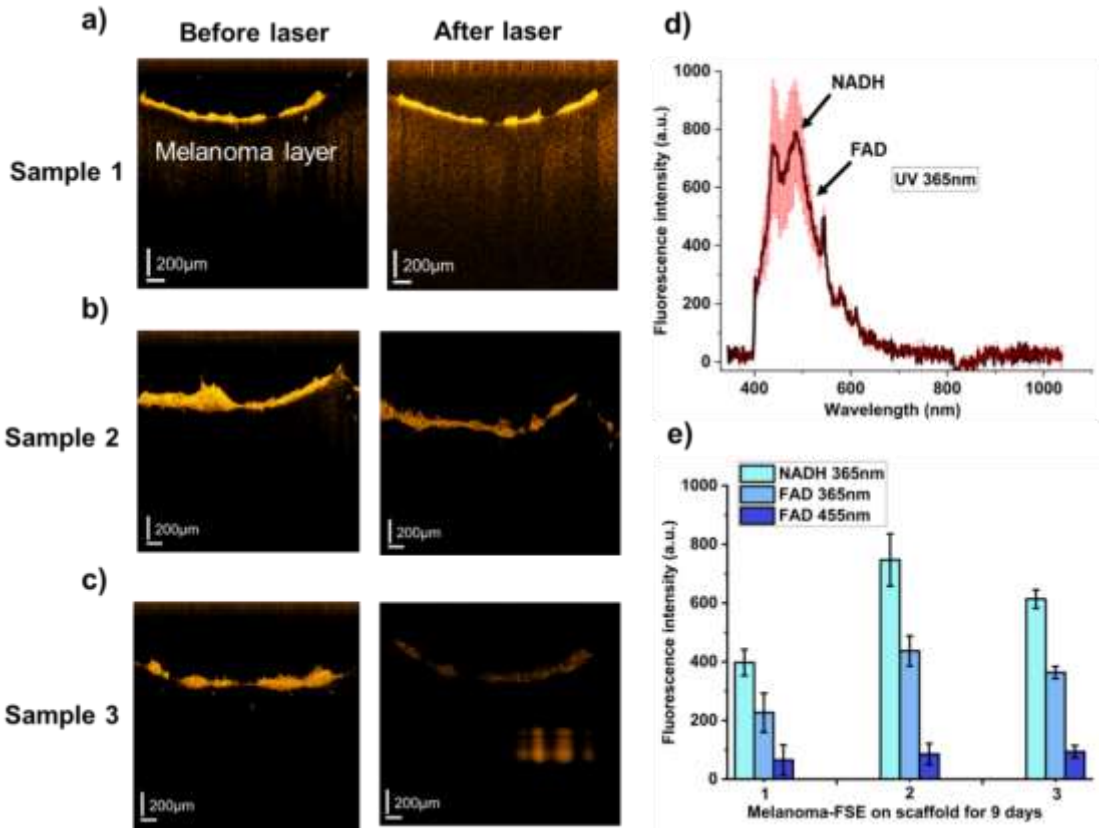

Figure 6.4: The FS-OCT system evaluated the metabolism and morphology of 3D Melanoma-FSE on scaffolds. Representative OCT images of scaffold in the 6-well plate before and after laser interaction for sample 1,2, and 3 (a) at 237.6 J/cm2 (b) 475.3 J/cm2 (c) 712.9 J/cm2 respectively. Scale bar: 200 μm. (d) Fluorescence spectra of 9 days of culturing of Melanoma-FSE at 365 nm and 455 nm excitation, correspondingly. (e) Maximum fluorescence intensity of 9 days of culturing of Melanoma-FSE at different excitation wavelengths. Data are presented as mean±SD (n=3).

References

[1] C. S. Enwemeka, “Therapeutic light,” *Rehab Manag*, vol. 17, no. 1, pp. 20–25, 56–57, 2004.

[2] A. Cios *et al.*, “Effect of Different Wavelengths of Laser Irradiation on the Skin Cells,” *Int J Mol Sci*, vol. 22, no. 5, p. 2437, Feb. 2021, doi: 10.3390/ijms22052437.

[3] J. J. Bernard, R. L. Gallo, and J. Krutmann, “Photoimmunology: how ultraviolet radiation affects the immune system,” *Nat Rev Immunol*, vol. 19, no. 11, Art. no. 11, Nov. 2019, doi: 10.1038/s41577-019-0185-9.

[4] E. Sutterby, C. Chheang, P. Thurgood, K. Khoshmanesh, S. Baratchi, and E. Pirogova, “Investigating the effects of low intensity visible light on human keratinocytes using a customized LED exposure system,” *Sci Rep*, vol. 12, no. 1, Art. no. 1, Nov. 2022, doi: 10.1038/s41598-022-23751-3.

[5] W. Katagiri, G. Lee, A. Tanushi, K. Tsukada, H. S. Choi, and S. Kashiwagi, “High-throughput single-cell live imaging of photobiomodulation with multispectral near-infrared lasers in cultured T cells,” *J Biomed Opt*, vol. 25, no. 3, pp. 1–18, Mar. 2020, doi: 10.1117/1.JBO.25.3.036003.

[6] Z. Wu, W. S. Ho, and R. Lu, “Targeting Mitochondrial Oxidative Phosphorylation in Glioblastoma Therapy,” *Neuromol Med*, vol. 24, no. 1, pp. 18–22, Mar. 2022, doi: 10.1007/s12017-021-08678-8.

[7] D. Nolfi-Donegan, A. Braganza, and S. Shiva, “Mitochondrial electron transport chain: Oxidative phosphorylation, oxidant production, and methods of measurement,” *Redox Biol*, vol. 37, p. 101674, Oct. 2020, doi: 10.1016/j.redox.2020.101674.

[8] M. R. Hamblin and T. N. Demidova-Rice, “Cellular chromophores and signaling in low level light therapy,” vol. 6428, p. 642802, Feb. 2007, doi: 10.1117/12.712885.

[9] Y. Liu, G. Fiskum, and D. Schubert, “Generation of reactive oxygen species by the mitochondrial electron transport chain,” *J Neurochem*, vol. 80, no. 5, pp. 780–787, Mar. 2002, doi: 10.1046/j.0022-3042.2002.00744.x.

[10] L. Stryer and J. M. Berg, *Biochemistry*, 4th ed. New York: W.H. Freeman, 1995.

[11] A. Solhaug, M. Gjessing, M. Sandvik, and G. S. Eriksen, “The gill epithelial cell lines RTgill-W1, from Rainbow trout and ASG-10, from Atlantic salmon, exert different toxicity profiles towards rotenone,” *Cytotechnology*, vol. 75, no. 1, pp. 63–75, Feb. 2023, doi: 10.1007/s10616-022-00560-0.

[12] D. G. Nicholls and S. L. Budd, “Mitochondria and neuronal survival,” *Physiol Rev*, vol. 80, no. 1, pp. 315–360, Jan. 2000, doi: 10.1152/physrev.2000.80.1.315.

[13] X. Gao and D. Xing, “Molecular mechanisms of cell proliferation induced by low power laser irradiation,” *Journal of Biomedical Science*, vol. 16, no. 1, p. 4, Jan. 2009, doi: 10.1186/1423-0127-16-4.

[14] M. Hamblin and T. Demidova, “Mechanisms of low level light therapy,” *Proc SPIE*, vol. 6140, pp. 1–12, Mar. 2006, doi: 10.1117/12.646294.

[15] N. Ramanujam, “Fluorescence Spectroscopy of Neoplastic and Non-Neoplastic Tissues,” *Neoplasia*, vol. 2, no. 1–2, pp. 89–117, Jan. 2000.

[16] R. Gillies, G. Zonios, R. R. Anderson, and N. Kollias, “Fluorescence excitation spectroscopy provides information about human skin in vivo,” *J Invest Dermatol*, vol. 115, no. 4, pp. 704–707, Oct. 2000, doi: 10.1046/j.1523-1747.2000.00091.x.

[17] A. R. Young, “Chromophores in human skin,” *Phys Med Biol*, vol. 42, no. 5, pp. 789–802, May 1997, doi: 10.1088/0031-9155/42/5/004.

[18] M. Motta, Y. Haik, A. Gandhari, and C. J. Chen, “High magnetic field effects on human deoxygenated hemoglobin light absorption,” *Bioelectrochemistry and Bioenergetics*, vol. 47, no. 2, pp. 297–300, Dec. 1998, doi: 10.1016/S0302-4598(98)00165-2.

[19] S. H. Yun and S. J. J. Kwok, “Light in diagnosis, therapy and surgery,” *Nat Biomed Eng*, vol. 1, p. 0008, 2017, doi: 10.1038/s41551-016-0008.

[20] H. Michel, J. Behr, A. Harrenga, and A. Kannt, “Cytochrome c oxidase: structure and spectroscopy,” *Annu Rev Biophys Biomol Struct*, vol. 27, pp. 329–356, 1998, doi: 10.1146/annurev.biophys.27.1.329.

[21] M. Boulton, M. Rózanowska, B. Rózanowski, and T. Wess, “The photoreactivity of ocular lipofuscin,” *Photochem Photobiol Sci*, vol. 3, no. 8, pp. 759–764, Aug. 2004, doi: 10.1039/b400108g.

[22] Y. Pu, W. Wang, G. Tang, and R. R. Alfano, “Changes of collagen and nicotinamide adenine dinucleotide in human cancerous and normal prostate tissues studied using native fluorescence spectroscopy with selective excitation wavelength,” *J Biomed Opt*, vol. 15, no. 4, p. 047008, 2010, doi: 10.1117/1.3463479.

[23] G. Papayan, N. Petrishchev, and M. Galagudza, “Autofluorescence spectroscopy for NADH and flavoproteins redox state monitoring in the isolated rat heart subjected to ischemia-reperfusion,” *Photodiagnosis Photodyn Ther*, vol. 11, no. 3, pp. 400–408, Sep. 2014, doi: 10.1016/j.pdpdt.2014.05.003.

[24] N. D. Kirkpatrick, C. Zou, M. A. Brewer, W. R. Brands, R. A. Drezek, and U. Utzinger, “Endogenous fluorescence spectroscopy of cell suspensions for chemopreventive drug monitoring,” *Photochem Photobiol*, vol. 81, no. 1, pp. 125–134, 2005, doi: 10.1562/2004-08-09-RA-267.

[25] A. A. Heikal, “Intracellular coenzymes as natural biomarkers for metabolic activities and mitochondrial anomalies,” *Biomark Med*, vol. 4, no. 2, pp. 241–263, Apr. 2010, doi: 10.2217/bmm.10.1.

[26] A. U. Rehman, A. G. Anwer, M. E. Gosnell, S. B. Mahbub, G. Liu, and E. M. Goldys, “Fluorescence quenching of free and bound NADH in HeLa cells determined by hyperspectral imaging and unmixing of cell autofluorescence,” *Biomed Opt Express*, vol. 8, no. 3, pp. 1488–1498, Mar. 2017, doi: 10.1364/BOE.8.001488.

[27] S. Kalinina *et al.*, “Bioenergetic Alterations of Metabolic Redox Coenzymes as NADH, FAD and FMN by Means of Fluorescence Lifetime Imaging Techniques,” *Int J Mol Sci*, vol. 22, no. 11, p. 5952, May 2021, doi: 10.3390/ijms22115952.

[28] Q. Yu and A. A. Heikal, “Two-photon autofluorescence dynamics imaging reveals sensitivity of intracellular NADH concentration and conformation to cell physiology at the single-cell level,” *J Photochem Photobiol B*, vol. 95, no. 1, pp. 46–57, Apr. 2009, doi: 10.1016/j.jphotobiol.2008.12.010.

[29] V. Dremin, E. Potapova, A. Mamoshin, A. Dunaev, and E. Rafailov, “Monitoring oxidative metabolism while modeling pancreatic ischemia in mice using a multimodal spectroscopy technique,” *Laser Phys. Lett.*, vol. 17, no. 11, p. 115605, Oct. 2020, doi: 10.1088/1612-202X/abbefa.

[30] V. Dremin *et al.*, “Optical percutaneous needle biopsy of the liver: a pilot animal and clinical study,” *Sci Rep*, vol. 10, p. 14200, Aug. 2020, doi: 10.1038/s41598-020-71089-5.

[31] S. Palmer, K. Litvinova, E. U. Rafailov, and G. Nabi, “Detection of urinary bladder cancer cells using redox ratio and double excitation wavelengths autofluorescence,” *Biomed Opt Express*, vol. 6, no. 3, pp. 977–986, Feb. 2015, doi: 10.1364/BOE.6.000977.

[32] N. N. Houreld, “Shedding Light on a New Treatment for Diabetic Wound Healing: A Review on Phototherapy,” *ScientificWorldJournal*, vol. 2014, p. 398412, Jan. 2014, doi: 10.1155/2014/398412.

[33] M. C. Skala *et al.*, “In vivo multiphoton microscopy of NADH and FAD redox states, fluorescence lifetimes, and cellular morphology in precancerous epithelia,” *Proceedings of the National Academy of Sciences*, vol. 104, no. 49, pp. 19494–19499, Dec. 2007, doi: 10.1073/pnas.0708425104.

[34] K. S. Litvinova, I. E. Rafailov, A. V. Dunaev, S. G. Sokolovski, and E. U. Rafailov, “Non-invasive biomedical research and diagnostics enabled by innovative compact lasers,” *Progress in Quantum Electronics*, vol. 56, pp. 1–14, Oct. 2017, doi: 10.1016/j.pquantelec.2017.10.001.

[35] V. V. Tuchin, “Tissue Optics and Photonics: Light-Tissue Interaction II,” *Journal of Biomedical Photonics & Engineering*, vol. 2, no. 3, Art. no. 3, Sep. 2016, doi: 10.18287/JBPE16.02.030201.

[36] M. Roger *et al.*, “Bioengineering the microanatomy of human skin,” *J Anat*, vol. 234, no. 4, pp. 438–455, Apr. 2019, doi: 10.1111/joa.12942.

[37] S. Tavakoli and A. Klar, “Advanced Hydrogels as Wound Dressings,” *Biomolecules*, vol. 10, p. 1169, Aug. 2020, doi: 10.3390/biom10081169.

[38] C. L. Simpson, D. M. Patel, and K. J. Green, “Deconstructing the skin: cytoarchitectural determinants of epidermal morphogenesis,” *Nat Rev Mol Cell Biol*, vol. 12, no. 9, Art. no. 9, Sep. 2011, doi: 10.1038/nrm3175.

[39] R. Fleischmajer *et al.*, “Initiation of skin basement membrane formation at the epidermo-dermal interface involves assembly of laminins through binding to cell membrane receptors,” *Journal of Cell Science*, vol. 111, no. 14, pp. 1929–1940, Jul. 1998, doi: 10.1242/jcs.111.14.1929.

[40] A. Uong and L. I. Zon, “Melanocytes in development and cancer,” *J Cell Physiol*, vol. 222, no. 1, pp. 38–41, Jan. 2010, doi: 10.1002/jcp.21935.

[41] P. Haridas, J. A. McGovern, S. D. L. McElwain, and M. J. Simpson, “Quantitative comparison of the spreading and invasion of radial growth phase and metastatic melanoma cells in a three-dimensional human skin equivalent model,” *PeerJ*, vol. 5, p. e3754, 2017, doi: 10.7717/peerj.3754.

[42] H. Vörsmann *et al.*, “Development of a human three-dimensional organotypic skin-melanoma spheroid model for in vitro drug testing,” *Cell Death Dis*, vol. 4, no. 7, p. e719, Jul. 2013, doi: 10.1038/cddis.2013.249.

[43] F. S, V. C, L. P, P. Rf, V. A, and B. P, “3D Bioprinting: An Enabling Technology to Understand Melanoma,” *Cancers*, vol. 14, no. 14, Jul. 2022, doi: 10.3390/cancers14143535.

[44] M. Arnold *et al.*, “Global Burden of Cutaneous Melanoma in 2020 and Projections to 2040,” *JAMA Dermatology*, vol. 158, no. 5, pp. 495–503, May 2022, doi: 10.1001/jamadermatol.2022.0160.

[45] K. Urban, S. Mehrmal, P. Uppal, R. L. Giesey, and G. R. Delost, “The global burden of skin cancer: A longitudinal analysis from the Global Burden of Disease Study, 1990–2017,” *JAAD International*, vol. 2, p. 98, Mar. 2021, doi: 10.1016/j.jdin.2020.10.013.

[46] Z. Apalla, D. Nashan, R. B. Weller, and X. Castellsagué, “Skin Cancer: Epidemiology, Disease Burden, Pathophysiology, Diagnosis, and Therapeutic

Approaches," *Dermatol Ther (Heidelb)*, vol. 7, no. Suppl 1, pp. 5–19, Feb. 2017, doi: 10.1007/s13555-016-0165-y.

[47] N. H. Matthews, W.-Q. Li, A. A. Qureshi, M. A. Weinstock, and E. Cho, "Epidemiology of Melanoma," in *Cutaneous Melanoma: Etiology and Therapy*, W. H. Ward and J. M. Farma, Eds., Brisbane (AU): Codon Publications, 2017. Accessed: Nov. 20, 2023. [Online]. Available: http://www.ncbi.nlm.nih.gov/books/NBK481862/

[48] T. H. Ryu, H. Kye, J. E. Choi, H. H. Ahn, Y. C. Kye, and S. H. Seo, "Features Causing Confusion between Basal Cell Carcinoma and Squamous Cell Carcinoma in Clinical Diagnosis," *Ann Dermatol*, vol. 30, no. 1, pp. 64–70, Feb. 2018, doi: 10.5021/ad.2018.30.1.64.

[49] L. E. Davis, S. C. Shalin, and A. J. Tackett, "Current state of melanoma diagnosis and treatment," *Cancer Biol Ther*, vol. 20, no. 11, pp. 1366–1379, Aug. 2019, doi: 10.1080/15384047.2019.1640032.

[50] M. D *et al.*, "An ultraviolet-radiation-independent pathway to melanoma carcinogenesis in the red hair/fair skin background," *Nature*, vol. 491, no. 7424, Nov. 2012, doi: 10.1038/nature11624.

[51] A. Breslow, "Tumor thickness, level of invasion and node dissection in stage I cutaneous melanoma.," *Ann Surg*, vol. 182, no. 5, pp. 572–575, Nov. 1975.

[52] A. N. Crowson, C. M. Magro, and M. C. Mihm, "Prognosticators of melanoma, the melanoma report, and the sentinel lymph node," *Mod Pathol*, vol. 19 Suppl 2, pp. S71-87, Feb. 2006, doi: 10.1038/modpathol.3800517.

[53] G. Baranoski and A. Krishnaswamy, "An Introduction to Light Interaction with Human Skin," *Revista de Informática Teórica e Aplicada; Vol. 11, No 1 (2004); 33-62*, vol. 11, Jun. 2004, doi: 10.22456/2175-2745.5961.

[54] C. Ash, M. Dubec, K. Donne, and T. Bashford, "Effect of wavelength and beam width on penetration in light-tissue interaction using computational methods," *Lasers Med Sci*, vol. 32, no. 8, pp. 1909–1918, Nov. 2017, doi: 10.1007/s10103-017-2317-4.

[55] M. Kapałczyńska *et al.*, "2D and 3D cell cultures – a comparison of different types of cancer cell cultures," *Arch Med Sci*, vol. 14, no. 4, pp. 910–919, Jun. 2018, doi: 10.5114/aoms.2016.63743.

[56] D. Huh, G. A. Hamilton, and D. E. Ingber, "From 3D cell culture to organs-on-chips," *Trends Cell Biol*, vol. 21, no. 12, pp. 745–754, Dec. 2011, doi: 10.1016/j.tcb.2011.09.005.

[57] V. van Duinen, S. J. Trietsch, J. Joore, P. Vulto, and T. Hankemeier, "Microfluidic 3D cell culture: from tools to tissue models," *Current Opinion in Biotechnology*, vol. 35, pp. 118–126, Dec. 2015, doi: 10.1016/j.copbio.2015.05.002.

[58] N. Chaicharoenaudomrung, P. Kunhorm, and P. Noisa, “Three-dimensional cell culture systems as an in vitro platform for cancer and stem cell modeling,” *World J Stem Cells*, vol. 11, no. 12, pp. 1065–1083, Dec. 2019, doi: 10.4252/wjsc.v11.i12.1065.

[59] A. Alghuwainem, A. T. Alshareeda, and B. Alsowayan, “Scaffold-Free 3-D Cell Sheet Technique Bridges the Gap between 2-D Cell Culture and Animal Models,” *Int J Mol Sci*, vol. 20, no. 19, p. 4926, Oct. 2019, doi: 10.3390/ijms20194926.

[60] “Polymeric Scaffolds in Tissue Engineering Application: A Review - Dhandayuthapani - 2011 - International Journal of Polymer Science - Wiley Online Library.” Accessed: Sep. 17, 2024. [Online]. Available: https://onlinelibrary.wiley.com/doi/10.1155/2011/290602

[61] J. An, J. E. M. Teoh, R. Suntornnond, and C. K. Chua, “Design and 3D Printing of Scaffolds and Tissues,” *Engineering*, vol. 1, no. 2, pp. 261–268, Jun. 2015, doi: 10.15302/J-ENG-2015061.

[62] B. P. Chan and K. W. Leong, “Scaffolding in tissue engineering: general approaches and tissue-specific considerations,” *European Spine Journal*, vol. 17, no. Suppl 4, p. 467, Dec. 2008, doi: 10.1007/s00586-008-0745-3.

[63] X. Chen *et al.*, “Scaffold Structural Microenvironmental Cues to Guide Tissue Regeneration in Bone Tissue Applications,” *Nanomaterials (Basel)*, vol. 8, no. 11, p. 960, Nov. 2018, doi: 10.3390/nano8110960.

[64] J.-N. Fu *et al.*, “Scaffold-Based Tissue Engineering Strategies for Osteochondral Repair,” *Front. Bioeng. Biotechnol.*, vol. 9, Jan. 2022, doi: 10.3389/fbioe.2021.812383.

[65] M. P. Nikolova and M. S. Chavali, “Recent advances in biomaterials for 3D scaffolds: A review,” *Bioact Mater*, vol. 4, pp. 271–292, Dec. 2019, doi: 10.1016/j.bioactmat.2019.10.005.

[66] J. Wang *et al.*, “Fabrication and biological evaluation of 3D-printed calcium phosphate ceramic scaffolds with distinct macroporous geometries through digital light processing technology,” *Regenerative Biomaterials*, vol. 9, p. rbac005, Jan. 2022, doi: 10.1093/rb/rbac005.

[67] H. Jodati, B. Yılmaz, and Z. Evis, “A review of bioceramic porous scaffolds for hard tissue applications: Effects of structural features,” *Ceramics International*, vol. 46, no. 10, Part B, pp. 15725–15739, Jul. 2020, doi: 10.1016/j.ceramint.2020.03.192.

[68] “Fabrication of Silk Fibroin-Derived Fibrous Scaffold for Biomedical Frontiers - Rahman - 2024 - Macromolecular Materials and Engineering - Wiley Online Library.”

Accessed: May 28, 2024. [Online]. Available: https://onlinelibrary.wiley.com/doi/10.1002/mame.202300422?af=R

[69] J. L. Drury and D. J. Mooney, “Hydrogels for tissue engineering: scaffold design variables and applications,” *Biomaterials*, vol. 24, no. 24, pp. 4337–4351, Nov. 2003, doi: 10.1016/s0142-9612(03)00340-5.

[70] Y. Yu, A. Alkhawaji, Y. Ding, and J. Mei, “Decellularized scaffolds in regenerative medicine,” *Oncotarget*, vol. 7, no. 36, pp. 58671–58683, Jul. 2016, doi: 10.18632/oncotarget.10945.

[71] K. H. Hussein, K.-M. Park, K.-S. Kang, and H.-M. Woo, “Biocompatibility evaluation of tissue-engineered decellularized scaffolds for biomedical application,” *Materials Science and Engineering: C*, vol. 67, pp. 766–778, Oct. 2016, doi: 10.1016/j.msec.2016.05.068.

[72] S. Bhushan *et al.*, “Scaffold Fabrication Techniques of Biomaterials for Bone Tissue Engineering: A Critical Review,” *Bioengineering*, vol. 9, p. 728, Nov. 2022, doi: 10.3390/bioengineering9120728.

[73] A. Zielińska *et al.*, “Scaffolds for drug delivery and tissue engineering: The role of genetics,” *J Control Release*, vol. 359, pp. 207–223, Jul. 2023, doi: 10.1016/j.jconrel.2023.05.042.

[74] J.-W. Jang, K.-E. Min, C. Kim, J. Shin, J. Lee, and S. Yi, “Review: Scaffold Characteristics, Fabrication Methods, and Biomaterials for the Bone Tissue Engineering,” *Int. J. Precis. Eng. Manuf.*, vol. 24, no. 3, pp. 511–529, Mar. 2023, doi: 10.1007/s12541-022-00755-7.

[75] R. Gauvin *et al.*, “Microfabrication of complex porous tissue engineering scaffolds using 3D projection stereolithography,” *Biomaterials*, vol. 33, no. 15, pp. 3824–3834, May 2012, doi: 10.1016/j.biomaterials.2012.01.048.

[76] M. Dey and I. T. Ozbolat, “3D bioprinting of cells, tissues and organs,” *Sci Rep*, vol. 10, no. 1, Art. no. 1, Aug. 2020, doi: 10.1038/s41598-020-70086-y.

[77] B. Tan, S. Gan, X. Wang, W. Liu, and X. Li, “Applications of 3D bioprinting in tissue engineering: advantages, deficiencies, improvements, and future perspectives,” *Journal of Materials Chemistry B*, vol. 9, no. 27, pp. 5385–5413, 2021, doi: 10.1039/D1TB00172H.

[78] J. Zhang, E. Wehrle, M. Rubert, and R. Müller, “3D Bioprinting of Human Tissues: Biofabrication, Bioinks, and Bioreactors,” *Int J Mol Sci*, vol. 22, no. 8, p. 3971, Apr. 2021, doi: 10.3390/ijms22083971.

[79] I. Matai, G. Kaur, A. Seyedsalehi, A. McClinton, and C. T. Laurencin, “Progress in 3D bioprinting technology for tissue/organ regenerative engineering,” *Biomaterials*, vol. 226, p. 119536, Jan. 2020, doi: 10.1016/j.biomaterials.2019.119536.

[80] Ž. P. Kačarević *et al.*, “An Introduction to 3D Bioprinting: Possibilities, Challenges and Future Aspects,” *Materials (Basel)*, vol. 11, no. 11, p. 2199, Nov. 2018, doi: 10.3390/ma11112199.

[81] S. Zhang *et al.*, “Convergence of 3D Bioprinting and Nanotechnology in Tissue Engineering Scaffolds,” *Biomimetics (Basel)*, vol. 8, no. 1, p. 94, Feb. 2023, doi: 10.3390/biomimetics8010094.

[82] C. B. Arnold, P. Serra, and A. Piqué, “Laser Direct-Write Techniques for Printing of Complex Materials,” *MRS Bull.*, vol. 32, no. 1, pp. 23–31, Jan. 2007, doi: 10.1557/mrs2007.11.

[83] B. Yilmaz, A. Al Rashid, Y. Mou, Z. Evis, and M. Koç, “Bioprinting: A review of processes, materials and applications,” *Bioprinting*, vol. 23, 2021, doi: 10.1016/j.bprint.2021.e00148.

[84] W. Li, M. Wang, H. Ma, F. A. Chapa-Villarreal, A. O. Lobo, and Y. S. Zhang, “Stereolithography apparatus and digital light processing-based 3D bioprinting for tissue fabrication,” *iScience*, vol. 26, no. 2, p. 106039, Feb. 2023, doi: 10.1016/j.isci.2023.106039.

[85] K. Prem Ananth and N. D. Jayram, “A comprehensive review of 3D printing techniques for biomaterial-based scaffold fabrication in bone tissue engineering,” *Annals of 3D Printed Medicine*, vol. 13, p. 100141, Feb. 2024, doi: 10.1016/j.stlm.2023.100141.

[86] H. Li *et al.*, “Digital light processing (DLP)-based (bio)printing strategies for tissue modeling and regeneration,” *Aggregate*, vol. 4, no. 2, p. e270, 2023, doi: 10.1002/agt2.270.

[87] H. Hong *et al.*, “Digital light processing 3D printed silk fibroin hydrogel for cartilage tissue engineering,” *Biomaterials*, vol. 232, p. 119679, Feb. 2020, doi: 10.1016/j.biomaterials.2019.119679.

[88] H. Hwangbo and S.-J. Jeon, “Digital light processing 3D printing of multi-materials with improved adhesion using resins containing low functional acrylates,” *Korean J. Chem. Eng.*, vol. 39, no. 2, pp. 451–459, Feb. 2022, doi: 10.1007/s11814-021-0934-x.

[89] Z. Faraji Rad, P. Prewett, and G. Davies, “High-resolution two-photon polymerization: the most versatile technique for the fabrication of microneedle

arrays," *Microsystems and Nanoengineering*, vol. 7, no. 1, Art. no. 1, Jan. 2021, doi: 10.1038/s41378-021-00298-3.

[90] A. I. Ciuciu and P. J. Cywiński, "Two-photon polymerization of hydrogels – versatile solutions to fabricate well-defined 3D structures," *RSC Adv.*, vol. 4, no. 85, pp. 45504–45516, Sep. 2014, doi: 10.1039/C4RA06892K.

[91] X. Jing, H. Fu, B. Yu, M. Sun, and L. Wang, "Two-photon polymerization for 3D biomedical scaffolds: Overview and updates," *Front Bioeng Biotechnol*, vol. 10, p. 994355, 2022, doi: 10.3389/fbioe.2022.994355.

[92] J. Zhang, Q. Hu, S. Wang, J. Tao, and M. Gou, "Digital Light Processing Based Three-dimensional Printing for Medical Applications," *Int J Bioprint*, vol. 6, no. 1, p. 242, Nov. 2019, doi: 10.18063/ijb.v6i1.242.

[93] R. Khoeini *et al.*, "Natural and Synthetic Bioinks for 3D Bioprinting," *Advanced NanoBiomed Research*, vol. 1, no. 8, p. 2000097, 2021, doi: 10.1002/anbr.202000097.

[94] A. Koroleva *et al.*, "Osteogenic differentiation of human mesenchymal stem cells in 3-D Zr-Si organic-inorganic scaffolds produced by two-photon polymerization technique," *PLoS One*, vol. 10, no. 2, p. e0118164, 2015, doi: 10.1371/journal.pone.0118164.

[95] F. Matheuse, K. Vanmol, J. Van Erps, W. De Malsche, H. Ottevaere, and G. Desmet, "On the potential use of two-photon polymerization to 3D print chromatographic packed bed supports," *Journal of Chromatography A*, vol. 1663, p. 462763, Jan. 2022, doi: 10.1016/j.chroma.2021.462763.

[96] S. Agarwal, S. Saha, V. K. Balla, A. Pal, A. Barui, and S. Bodhak, "Current Developments in 3D Bioprinting for Tissue and Organ Regeneration–A Review," *Front. Mech. Eng.*, vol. 6, Oct. 2020, doi: 10.3389/fmech.2020.589171.

[97] Z. Xie, M. Gao, A. O. Lobo, and T. J. Webster, "3D Bioprinting in Tissue Engineering for Medical Applications: The Classic and the Hybrid," *Polymers (Basel)*, vol. 12, no. 8, p. 1717, Jul. 2020, doi: 10.3390/polym12081717.

[98] Muskan, D. Gupta, and N. P. Negi, "3D bioprinting: Printing the future and recent advances," *Bioprinting*, vol. 27, p. e00211, Aug. 2022, doi: 10.1016/j.bprint.2022.e00211.

[99] S. Barui, "3D inkjet printing of biomaterials: Principles and applications," *MEDICAL DEVICES & SENSORS*, vol. 4, no. 1, p. e10143, 2021, doi: 10.1002/mds3.10143.

[100] J. Mancilla-De-la-Cruz, M. Rodriguez-Salvador, J. An, and C. K. Chua, "Three-Dimensional Printing Technologies for Drug Delivery Applications: Processes,

Materials, and Effects," *Int J Bioprint*, vol. 8, no. 4, p. 622, 2022, doi: 10.18063/ijb.v8i4.622.

[101]R. Xie *et al.*, "A comprehensive review on 3D tissue models: Biofabrication technologies and preclinical applications," *Biomaterials*, vol. 304, p. 122408, Jan. 2024, doi: 10.1016/j.biomaterials.2023.122408.

[102]"Bioprinting: From Tissue and Organ Development to in Vitro Models | Chemical Reviews." Accessed: Apr. 10, 2024. [Online]. Available: https://pubs.acs.org/doi/10.1021/acs.chemrev.9b00789

[103]K. Unnikrishnan, L. V. Thomas, and R. M. Ram Kumar, "Advancement of Scaffold-Based 3D Cellular Models in Cancer Tissue Engineering: An Update," *Front. Oncol.*, vol. 11, Oct. 2021, doi: 10.3389/fonc.2021.733652.

[104]M. P. Nikolova and M. S. Chavali, "Recent advances in biomaterials for 3D scaffolds: A review," *Bioactive Materials*, vol. 4, pp. 271–292, Dec. 2019, doi: 10.1016/j.bioactmat.2019.10.005.

[105]C. Dong and Y. Lv, "Application of Collagen Scaffold in Tissue Engineering: Recent Advances and New Perspectives," *Polymers (Basel)*, vol. 8, no. 2, p. 42, Feb. 2016, doi: 10.3390/polym8020042.

[106]J. Redmond, H. McCarthy, P. Buchanan, T. J. Levingstone, and N. J. Dunne, "Advances in biofabrication techniques for collagen-based 3D *in vitro* culture models for breast cancer research," *Materials Science and Engineering: C*, vol. 122, p. 111944, Mar. 2021, doi: 10.1016/j.msec.2021.111944.

[107]J. Gong *et al.*, "Digital light processing (DLP) in tissue engineering: from promise to reality, and perspectives," *Biomed. Mater.*, vol. 17, no. 6, p. 062004, Oct. 2022, doi: 10.1088/1748-605X/ac96ba.

[108]A. Koroleva *et al.*, "In Vitro Development of Human iPSC-Derived Functional Neuronal Networks on Laser-Fabricated 3D Scaffolds," *ACS Appl. Mater. Interfaces*, vol. 13, no. 7, pp. 7839–7853, Feb. 2021, doi: 10.1021/acsami.0c16616.

[109]F. Groeber, M. Holeiter, M. Hampel, S. Hinderer, and K. Schenke-Layland, "Skin tissue engineering--in vivo and in vitro applications," *Adv Drug Deliv Rev*, vol. 63, no. 4–5, pp. 352–366, Apr. 2011, doi: 10.1016/j.addr.2011.01.005.

[110]G. Sriram *et al.*, "Full-thickness human skin-on-chip with enhanced epidermal morphogenesis and barrier function," *Materials Today*, vol. 21, no. 4, pp. 326–340, May 2018, doi: 10.1016/j.mattod.2017.11.002.

[111]S. Choudhury and A. Das, "Advances in generation of three-dimensional skin equivalents: pre-clinical studies to clinical therapies," *Cytotherapy*, vol. 23, no. 1, pp. 1–9, Jan. 2021, doi: 10.1016/j.jcyt.2020.10.001.

[112]R. Cai, N. Gimenez-Camino, M. Xiao, S. Bi, and K. A. DiVito, “Technological advances in three-dimensional skin tissue engineering,” *REVIEWS ON ADVANCED MATERIALS SCIENCE*, vol. 62, no. 1, Jan. 2023, doi: 10.1515/rams-2022-0289.

[113]M. Michel, N. L’Heureux, R. Pouliot, W. Xu, F. A. Auger, and L. Germain, “Characterization of a New Tissue-Engineered Human Skin Equivalent with Hair,” *In Vitro Cellular & Developmental Biology. Animal*, vol. 35, no. 6, pp. 318–326, 1999.

[114]B. S. Kim, J.-S. Lee, G. Gao, and D.-W. Cho, “Direct 3D cell-printing of human skin with functional transwell system,” *Biofabrication*, vol. 9, no. 2, p. 025034, Jun. 2017, doi: 10.1088/1758-5090/aa71c8.

[115]V. W. Rebecca, R. Somasundaram, and M. Herlyn, “Pre-clinical modeling of cutaneous melanoma,” *Nat Commun*, vol. 11, no. 1, Art. no. 1, Jun. 2020, doi: 10.1038/s41467-020-15546-9.

[116]S. Gunti, A. T. K. Hoke, K. P. Vu, and N. R. London, “Organoid and Spheroid Tumor Models: Techniques and Applications,” *Cancers (Basel)*, vol. 13, no. 4, p. 874, Feb. 2021, doi: 10.3390/cancers13040874.

[117]F. Meier *et al.*, “Human Melanoma Progression in Skin Reconstructs: Biological Significance of bFGF,” *The American Journal of Pathology*, vol. 156, no. 1, pp. 193–200, Jan. 2000, doi: 10.1016/S0002-9440(10)64719-0.

[118]D. S. Hill *et al.*, “A Novel Fully Humanized 3D Skin Equivalent to Model Early Melanoma Invasion,” *Mol Cancer Ther*, vol. 14, no. 11, pp. 2665–2673, Nov. 2015, doi: 10.1158/1535-7163.MCT-15-0394.

[119]A. Shahzad, G. Koehler, M. Knapp, E. Gaubitzer, M. Puchinger, and M. Edetsberger, “Emerging applications of fluorescence spectroscopy in medical microbiology field,” *Journal of translational medicine*, vol. 7, p. 99, Nov. 2009, doi: 10.1186/1479-5876-7-99.

[120]L. Bachmann, D. Zezell, A. Ribeiro, L. Gomes, and A. Ito, “Fluorescence Spectroscopy of Biological Tissues—A Review,” *Applied Spectroscopy Reviews*, vol. 41, pp. 575–590, Dec. 2006, doi: 10.1080/05704920600929498.

[121]S. S. Nazeer, A. Saraswathy, A. K. Gupta, and R. S. Jayasree, “Fluorescence spectroscopy as a highly potential single-entity tool to identify chromophores and fluorophores: study on neoplastic human brain lesions,” *J Biomed Opt*, vol. 18, no. 6, p. 067002, Jun. 2013, doi: 10.1117/1.JBO.18.6.067002.

[122]M. Gooz and E. Maldonado, “Fluorescence microscopy imaging of mitochondrial metabolism in cancer cells,” *Frontiers in Oncology*, vol. 13, Jun. 2023, doi: 10.3389/fonc.2023.1152553.

[123]M. J. Sanderson, I. Smith, I. Parker, and M. D. Bootman, “Fluorescence Microscopy,” *Cold Spring Harbor protocols*, vol. 2014, no. 10, p. pdb.top071795, Oct. 2014, doi: 10.1101/pdb.top071795.

[124]“Strategy for Fluorescence/Photoacoustic Signal Maximization Using Dual-Wavelength-Independent Excitation | Analytical Chemistry.” Accessed: Sep. 19, 2024. [Online]. Available: https://pubs.acs.org/doi/full/10.1021/acs.analchem.3c02372

[125]W. Goth, J. Lesicko, M. S. Sacks, and J. W. Tunnell, “Optical-Based Analysis of Soft Tissue Structures,” *Annu Rev Biomed Eng*, vol. 18, pp. 357–385, Jul. 2016, doi: 10.1146/annurev-bioeng-071114-040625.

[126]F. Spöler *et al.*, “High-resolution optical coherence tomography as a non-destructive monitoring tool for the engineering of skin equivalents,” *Skin Res Technol*, vol. 12, no. 4, pp. 261–267, Nov. 2006, doi: 10.1111/j.0909-752X.2006.00163.x.

[127]U. Sharma, E. W. Chang, and S. H. Yun, “Long-wavelength optical coherence tomography at 1.7 μm for enhanced imaging depth,” *Opt Express*, vol. 16, no. 24, pp. 19712–19723, Nov. 2008.

[128]A. Mcheik, C. Tauber, H. Batatia, J. George, and J.-M. Lagarde, “Speckle Modelization in OCT Images for Skin Layers Segmentation.,” Jan. 2008, pp. 347–350.

[129]Y. Hara, Y. Ogura, T. Yamashita, D. Furukawa, and S. Saeki, “Visualization of viscoelastic behavior in skin equivalent using optical coherence tomography-based straingraphy,” *Skin Res Technol*, vol. 24, no. 2, pp. 334–339, May 2018, doi: 10.1111/srt.12435.

[130]Z. Hosseinaee, J. Simmons, and P. Hajireza, “Dual-Modal Photoacoustic Imaging and Optical Coherence Tomography [Review],” *Frontiers in Physics*, vol. 8, Jan. 2021, doi: 10.3389/fphy.2020.616618.

[131]S. Yuan *et al.*, “Combining Optical Coherence Tomography with Fluorescence Molecular Imaging: Towards Simultaneous Morphology and Molecular Imaging,” *Phys Med Biol*, vol. 55, no. 1, pp. 191–206, Jan. 2010, doi: 10.1088/0031-9155/55/1/011.

[132]C. F. G. C. Geraldes, “Introduction to Infrared and Raman-Based Biomedical Molecular Imaging and Comparison with Other Modalities,” *Molecules*, vol. 25, no. 23, Art. no. 23, Jan. 2020, doi: 10.3390/molecules25235547.

[133]Y. Yu *et al.*, “Simultaneous photoacoustic and ultrasound imaging: A review,” *Ultrasonics*, vol. 139, p. 107277, Apr. 2024, doi: 10.1016/j.ultras.2024.107277.

[134]Y. S. Kim *et al.*, “Combining Three-Dimensional Quantitative Phase Imaging and Fluorescence Microscopy for the Study of Cell Pathophysiology,” *Yale J Biol Med*, vol. 91, no. 3, pp. 267–277, Sep. 2018.

[135]N. W. N. Simelane, C. A. Kruger, and H. Abrahamse, “Photodynamic diagnosis and photodynamic therapy of colorectal cancer in vitro and in vivo,” *RSC Adv.*, vol. 10, no. 68, pp. 41560–41576, Nov. 2020, doi: 10.1039/D0RA08617G.

[136]G. Mowatt *et al.*, “Photodynamic diagnosis of bladder cancer compared with white light cystoscopy: Systematic review and meta-analysis,” *International journal of technology assessment in health care*, vol. 27, pp. 3–10, Jan. 2011, doi: 10.1017/S0266462310001364.

[137]P. S. Maharjan and H. K. Bhattarai, “Singlet Oxygen, Photodynamic Therapy, and Mechanisms of Cancer Cell Death,” *J Oncol*, vol. 2022, p. 7211485, Jun. 2022, doi: 10.1155/2022/7211485.

[138]F. Anquez, I. El Yazidi-Belkoura, S. Randoux, P. Suret, and E. Courtade, “Cancerous cell death from sensitizer free photoactivation of singlet oxygen,” *Photochem Photobiol*, vol. 88, no. 1, pp. 167–174, 2012, doi: 10.1111/j.1751-1097.2011.01028.x.

[139]G. M. F. Calixto, J. Bernegossi, L. M. de Freitas, C. R. Fontana, and M. Chorilli, “Nanotechnology-Based Drug Delivery Systems for Photodynamic Therapy of Cancer: A Review,” *Molecules*, vol. 21, no. 3, p. 342, Mar. 2016, doi: 10.3390/molecules21030342.

[140]S.-R. T. Michael R. Hamblin, “Biological effects and medical applications of infrared radiation,” vol. 170, pp. 197–207, 2017.

[141]L. F. de Freitas and M. R. Hamblin, “Proposed Mechanisms of Photobiomodulation or Low-Level Light Therapy,” *IEEE J Sel Top Quantum Electron*, vol. 22, no. 3, p. 7000417, 2016, doi: 10.1109/JSTQE.2016.2561201.

[142]C. Dompe *et al.*, “Photobiomodulation-Underlying Mechanism and Clinical Applications,” *J Clin Med*, vol. 9, no. 6, p. 1724, Jun. 2020, doi: 10.3390/jcm9061724.

[143]M. R. Hamblin, “Photobiomodulation for Alzheimer’s Disease: Has the Light Dawned?,” *Photonics*, vol. 6, no. 3, p. 77, Sep. 2019, doi: 10.3390/photonics6030077.

[144]R. O. Poyton and K. A. Ball, “Therapeutic photobiomodulation: nitric oxide and a novel function of mitochondrial cytochrome c oxidase,” *Discov Med*, vol. 11, no. 57, pp. 154–159, Feb. 2011.

[145]V. Dremin, O. Semyachkina-Glushkovskaya, and E. Rafailov, “Direct Laser-Induced Singlet Oxygen in Biological Systems: Application From in Vitro to in Vivo,” *IEEE*

Journal of Selected Topics in Quantum Electronics, vol. 29, no. 4: Biophotonics, pp. 1–11, Jul. 2023, doi: 10.1109/JSTQE.2023.3246587.

[146] S. V. Bs, A. Ag, and A. A, "Redox Responsive Copolyoxalate Smart Polymers for Inflammation and Other Aging-Associated Diseases," *International journal of molecular sciences*, vol. 22, no. 11, May 2021, doi: 10.3390/ijms22115607.

[147] A. J. Lambert and M. D. Brand, "Reactive oxygen species production by mitochondria," *Methods Mol Biol*, vol. 554, pp. 165–181, 2009, doi: 10.1007/978-1-59745-521-3_11.

[148] P. Sharma, A. B. Jha, R. S. Dubey, and M. Pessarakli, "Reactive Oxygen Species, Oxidative Damage, and Antioxidative Defense Mechanism in Plants under Stressful Conditions," *Journal of Botany*, vol. 2012, pp. 1–26, Apr. 2012, doi: 10.1155/2012/217037.

[149] M. Hasanuzzaman *et al.*, "Reactive Oxygen Species and Antioxidant Defense in Plants under Abiotic Stress: Revisiting the Crucial Role of a Universal Defense Regulator," *Antioxidants (Basel)*, vol. 9, no. 8, p. 681, Jul. 2020, doi: 10.3390/antiox9080681.

[150] O. V. Semyachkina-Glushkovskaya *et al.*, "Laser-induced generation of singlet oxygen and its role in the cerebrovascular physiology," *Progress in Quantum Electronics*, vol. 55, pp. 112–128, Sep. 2017, doi: 10.1016/j.pquantelec.2017.05.001.

[151] M. K. Kuimova, G. Yahioglu, and P. R. Ogilby, "Singlet Oxygen in a Cell: Spatially Dependent Lifetimes and Quenching Rate Constants," *J. Am. Chem. Soc.*, vol. 131, no. 1, pp. 332–340, Jan. 2009, doi: 10.1021/ja807484b.

[152] D. Beri, M. Jakoby, D. Busko, B. S. Richards, and A. Turshatov, "Enhancing Singlet Oxygen Generation in Conjugates of Silicon Nanocrystals and Organic Photosensitizers," *Front Chem*, vol. 8, p. 567, Jul. 2020, doi: 10.3389/fchem.2020.00567.

[153] M. R. Detty, "Direct 1270 nm irradiation as an alternative to photosensitized generation of singlet oxygen to induce cell death," *Photochem Photobiol*, vol. 88, no. 1, pp. 2–4, 2012, doi: 10.1111/j.1751-1097.2011.01047.x.

[154] M. P. Murphy, "How mitochondria produce reactive oxygen species," *Biochem J*, vol. 417, no. Pt 1, pp. 1–13, Jan. 2009, doi: 10.1042/BJ20081386.

[155] A. Juarranz, P. Jaén, F. Sanz-Rodríguez, J. Cuevas, and S. González, "Photodynamic therapy of cancer. Basic principles and applications," *Clin Transl Oncol*, vol. 10, no. 3, pp. 148–154, Mar. 2008, doi: 10.1007/s12094-008-0172-2.

[156] I. Makovik, A. Vinokurov, A. Dunaev, E. Rafailov, and V. Dremin, "Efficiency of direct photoinduced generation of singlet oxygen at different wavelengths, power density

and exposure time of laser irradiation," *Analyst*, vol. 148, no. 15, pp. 3559–3564, Jul. 2023, doi: 10.1039/D3AN00587A.

[157]A. V. Khokhlova *et al.*, "Effects of Laser Irradiation at 1265 nm in Melanoma Cells," *J. Phys.: Conf. Ser.*, vol. 2494, no. 1, p. 012007, May 2023, doi: 10.1088/1742-6596/2494/1/012007.

[158]hannah serrage, *et al.*, "Under the sportlight: mechanism of photobiomodulation concentrating on blue and green light," vol. 18, pp. 1877–1909, 2019.

[159]I. N. Novikova, E. V. Potapova, V. V. Dremin, A. V. Dunaev, and A. Y. Abramov, "Laser-induced singlet oxygen selectively triggers oscillatory mitochondrial permeability transition and apoptosis in melanoma cell lines," *Life Sciences*, vol. 304, p. 120720, Sep. 2022, doi: 10.1016/j.lfs.2022.120720.

[160]S. D. Zakharov and A. V. Ivanov, "Light-oxygen effect in cells and its potential applications in tumour therapy (review)," *Quantum Electron.*, vol. 29, no. 12, p. 1031, Dec. 1999, doi: 10.1070/QE1999v029n12ABEH001629.

[161]S. G. Sokolovski, E. U. Rafailov, A. Y. Abramov, and P. R. Angelova, "Singlet oxygen stimulates mitochondrial bioenergetics in brain cells," *Free Radic Biol Med*, vol. 163, pp. 306–313, Feb. 2021, doi: 10.1016/j.freeradbiomed.2020.12.022.

[162]Z. Pilát, J. Ježek, M. Šerý, M. Trtílek, L. Nedbal, and P. Zemánek, "Optical trapping of microalgae at 735–1064 nm: Photodamage assessment," *Journal of Photochemistry and Photobiology B: Biology*, vol. 121, pp. 27–31, Apr. 2013, doi: 10.1016/j.jphotobiol.2013.02.006.

[163]R. S. Wong, "Apoptosis in cancer: from pathogenesis to treatment," *Journal of Experimental & Clinical Cancer Research*, vol. 30, no. 1, p. 87, Sep. 2011, doi: 10.1186/1756-9966-30-87.

[164]T. Timmer, E. G. E. de Vries, and S. de Jong, "Fas receptor-mediated apoptosis: a clinical application?," *The Journal of Pathology*, vol. 196, no. 2, pp. 125–134, 2002, doi: 10.1002/path.1028.

[165]W. Zeng, X. Wang, P. Xu, G. Liu, H. S. Eden, and X. Chen, "Molecular Imaging of Apoptosis: From Micro to Macro," *Theranostics*, vol. 5, no. 6, pp. 559–582, Feb. 2015, doi: 10.7150/thno.11548.

[166]A. P. Demchenko, "Beyond annexin V: fluorescence response of cellular membranes to apoptosis," *Cytotechnology*, vol. 65, no. 2, pp. 157–172, Mar. 2013, doi: 10.1007/s10616-012-9481-y.

[167]D. V. Krysko, T. Vanden Berghe, K. D'Herde, and P. Vandenabeele, "Apoptosis and necrosis: detection, discrimination and phagocytosis," *Methods*, vol. 44, no. 3, pp. 205–221, Mar. 2008, doi: 10.1016/j.ymeth.2007.12.001.

[168]X. Zhang *et al.*, “Anti-cancer activity of Annexin V in murine melanoma model by suppressing tumor angiogenesis,” *Oncotarget*, vol. 8, no. 26, p. 42602, Jun. 2017, doi: 10.18632/oncotarget.16645.

[169]M. Mourdjeva, D. Kyurkchiev, A. Mandinova, I. Altankova, I. Kehayov, and S. Kyurkchiev, “Dynamics of membrane translocation of phosphatidylserine during apoptosis detected by a monoclonal antibody,” *Apoptosis*, vol. 10, no. 1, pp. 209–217, Jan. 2005, doi: 10.1007/s10495-005-6076-5.

[170]M. S. D’Arcy, “Cell death: a review of the major forms of apoptosis, necrosis and autophagy,” *Cell Biology International*, vol. 43, no. 6, pp. 582–592, 2019, doi: 10.1002/cbin.11137.

[171]E. Brauchle, S. Thude, S. Y. Brucker, and K. Schenke-Layland, “Cell death stages in single apoptotic and necrotic cells monitored by Raman microspectroscopy,” *Sci Rep*, vol. 4, no. 1, p. 4698, Apr. 2014, doi: 10.1038/srep04698.

[172]G. Pal *et al.*, “Effect of low intensity laser interaction with human skin fibroblast cells using fiber-optic nano-probes,” *Journal of Photochemistry and Photobiology B: Biology*, vol. 86, no. 3, pp. 252–261, Mar. 2007, doi: 10.1016/j.jphotobiol.2006.12.001.

[173]K. Kehe, M. Abend, K. Kehe, R. Ridi, R. U. Peter, and D. van Beuningen, “Tissue engineering with HaCaT cells and a fibroblast cell line,” *Arch Dermatol Res*, vol. 291, no. 11, pp. 600–605, Nov. 1999, doi: 10.1007/s004030050461.

[174]“Piccinini F, Tesei A, Arienti C, Bevilacqua A. Cell Counting and Viability Assessment of 2D and 3D Cell Cultures: Expected Reliability of the Trypan Blue Assay. Biol Proced Online. 2017 Jul 20;19:8. doi: 10.1186/s12575-017-0056-3. PMID: 28814944; PMCID: PMC5518102.”.

[175]S. Magaki, S. A. Hojat, B. Wei, A. So, and W. H. Yong, “An Introduction to the Performance of Immunohistochemistry,” *Methods Mol Biol*, vol. 1897, pp. 289–298, 2019, doi: 10.1007/978-1-4939-8935-5_25.

[176]M. Cregger, A. J. Berger, and D. L. Rimm, “Immunohistochemistry and quantitative analysis of protein expression,” *Arch Pathol Lab Med*, vol. 130, no. 7, pp. 1026–1030, Jul. 2006, doi: 10.5858/2006-130-1026-IAQAOP.

[177]S. Heraud *et al.*, “Structural and Biomechanical Characterization of a Scaffold-Free Skin Equivalent Model via Biophysical Methods,” *SPP*, vol. 33, no. 1, pp. 17–29, 2020, doi: 10.1159/000503154.

[178]V. V. V. Hira, A. L. de Jong, K. Ferro, M. Khurshed, R. J. Molenaar, and C. J. F. Van Noorden, “Comparison of different methodologies and cryostat versus paraffin

sections for chromogenic immunohistochemistry," *Acta Histochem*, vol. 121, no. 2, pp. 125–134, Feb. 2019, doi: 10.1016/j.acthis.2018.10.011.

[179]A. M. Rieger, K. L. Nelson, J. D. Konowalchuk, and D. R. Barreda, "Modified annexin V/propidium iodide apoptosis assay for accurate assessment of cell death," *J Vis Exp*, no. 50, p. 2597, Apr. 2011, doi: 10.3791/2597.

[180]S. Kim, T. Tachikawa, M. Fujitsuka, and T. Majima, "Far-red fluorescence probe for monitoring singlet oxygen during photodynamic therapy," *J Am Chem Soc*, vol. 136, no. 33, pp. 11707–11715, Aug. 2014, doi: 10.1021/ja504279r.

[181]N. Zhu, S. Mondal, S. Gao, S. Achilefu, V. Gruev, and R. Liang, "Dual-mode optical imaging system for fluorescence image-guided surgery," *Opt. Lett., OL*, vol. 39, no. 13, pp. 3830–3832, Jul. 2014, doi: 10.1364/OL.39.003830.

[182]M. Abbasi, A. Zarei-Hanzaki, K. Baghaei, H. R. Abedi, and N. Haghighipour, "Compression-induced apoptosis of fibroblasts and myofibroblasts in an in vitro model of pulmonary fibrosis by alginate/gelatin scaffold," *Int J Biol Macromol*, vol. 280, no. Pt 3, p. 135875, Sep. 2024, doi: 10.1016/j.ijbiomac.2024.135875.

[183]S. Ramasamy *et al.*, "Optimized construction of a full thickness human skin equivalent using 3D bioprinting and a PCL/collagen dermal scaffold," *Bioprinting*, vol. 21, no. e00123, Mar. 2021, doi: 10.1016/j.bprint.2020.e00123.

[184]K. Duval *et al.*, "Modeling Physiological Events in 2D vs. 3D Cell Culture," *Physiology*, vol. 32, no. 4, pp. 266–277, Jul. 2017, doi: 10.1152/physiol.00036.2016.

[185]J. Kim, B.-K. Koo, and J. A. Knoblich, "Human organoids: model systems for human biology and medicine," *Nat Rev Mol Cell Biol*, vol. 21, no. 10, Art. no. 10, Oct. 2020, doi: 10.1038/s41580-020-0259-3.

[186]J. A. Crowe *et al.*, "Development of two-photon polymerised scaffolds for optical interrogation and neurite guidance of human iPSC-derived cortical neuronal networks," *Lab on a Chip*, vol. 20, no. 10, pp. 1792–1806, 2020, doi: 10.1039/C9LC01209E.

[187]F. Zhou *et al.*, "Rapid printing of bio-inspired 3D tissue constructs for skin regeneration," *Biomaterials*, vol. 258, p. 120287, Nov. 2020, doi: 10.1016/j.biomaterials.2020.120287.

[188]Q. Geng, D. Wang, P. Chen, and S.-C. Chen, "Ultrafast multi-focus 3-D nano-fabrication based on two-photon polymerization," *Nat Commun*, vol. 10, no. 1, Art. no. 1, May 2019, doi: 10.1038/s41467-019-10249-2.

[189]A. Koroleva *et al.*, "*In Vitro* Development of Human iPSC-Derived Functional Neuronal Networks on Laser-Fabricated 3D Scaffolds," *ACS Appl. Mater. Interfaces*, vol. 13, no. 7, pp. 7839–7853, Feb. 2021, doi: 10.1021/acsami.0c16616.

[190]C. M. A. Reijnders, A. van Lier, S. Roffel, D. Kramer, R. J. Scheper, and S. Gibbs, “Development of a Full-Thickness Human Skin Equivalent *In Vitro* Model Derived from TERT-Immortalized Keratinocytes and Fibroblasts,” *Tissue Engineering Part A*, vol. 21, no. 17–18, pp. 2448–2459, Sep. 2015, doi: 10.1089/ten.tea.2015.0139.

[191]N. L’Heureux, S. Pâquet, R. Labbé, L. Germain, and F. A. Auger, “A completely biological tissue-engineered human blood vessel,” *The FASEB Journal*, vol. 12, no. 1, pp. 47–56, 1998, doi: 10.1096/fsb2fasebj.12.1.47.

[192]O. I. Kolenc and K. P. Quinn, “Evaluating Cell Metabolism Through Autofluorescence Imaging of NAD(P)H and FAD,” *Antioxid Redox Signal*, vol. 30, no. 6, pp. 875–889, Feb. 2019, doi: 10.1089/ars.2017.7451.

[193]M. Skala and N. Ramanujam, “Multiphoton Redox Ratio Imaging for Metabolic Monitoring in vivo,” *Methods Mol Biol*, vol. 594, pp. 155–162, 2010, doi: 10.1007/978-1-60761-411-1_11.

[194]C. Lennicke and H. M. Cochemé, “Redox metabolism: ROS as specific molecular regulators of cell signaling and function,” *Mol Cell*, vol. 81, no. 18, pp. 3691–3707, Sep. 2021, doi: 10.1016/j.molcel.2021.08.018.

[195]T. P. L. Ung *et al.*, “Simultaneous NAD(P)H and FAD fluorescence lifetime microscopy of long UVA–induced metabolic stress in reconstructed human skin,” *Sci Rep*, vol. 11, p. 22171, Nov. 2021, doi: 10.1038/s41598-021-00126-8.

[196]L. Hu, N. Wang, E. Cardona, and A. J. Walsh, “Fluorescence intensity and lifetime redox ratios detect metabolic perturbations in T cells,” *Biomed. Opt. Express, BOE*, vol. 11, no. 10, pp. 5674–5688, Oct. 2020, doi: 10.1364/BOE.401935.

[197]A. Mamalis, D. Ho, and J. Jagdeo, “Optical Coherence Tomography Imaging of Normal, Chronologically Aged, Photoaged and Photodamaged Skin: A Systematic Review,” *Dermatol Surg*, vol. 41, no. 9, pp. 993–1005, Sep. 2015, doi: 10.1097/DSS.0000000000000457.

[198]J. Galbán, I. Sanz-Vicente, J. Navarro, and S. de Marcos, “The intrinsic fluorescence of FAD and its application in analytical chemistry: a review,” *Methods Appl Fluoresc*, vol. 4, no. 4, p. 042005, Dec. 2016, doi: 10.1088/2050-6120/4/4/042005.

[199]H. N. XU, B. WU, S. NIOKA, B. CHANCE, and L. Z. LI, “QUANTITATIVE REDOX SCANNING OF TISSUE SAMPLES USING A CALIBRATION PROCEDURE,” *J Innov Opt Health Sci*, vol. 2, no. 4, pp. 375–385, Oct. 2009, doi: 10.1142/S1793545809000681.

[200]I. Georgakoudi and K. P. Quinn, “Optical Imaging Using Endogenous Contrast to Assess Metabolic State,” *Annual Review of Biomedical Engineering*, vol. 14, no. 1, pp. 351–367, 2012, doi: 10.1146/annurev-bioeng-071811-150108.

[201]Z. Liu *et al.*, “Mapping metabolic changes by noninvasive, multiparametric, high-resolution imaging using endogenous contrast,” *Science Advances*, vol. 4, p. eaap9302, Mar. 2018, doi: 10.1126/sciadv.aap9302.

[202]A.-M. Pena *et al.*, “Multiphoton FLIM imaging of NADH and FAD to analyze cellular metabolic activity of reconstructed human skin in response to UVA light,” vol. 10882, p. 108820A, Feb. 2019, doi: 10.1117/12.2508858.

[203]H. Niehues, J. A. Bouwstra, A. El Ghalbzouri, J. M. Brandner, P. L. J. M. Zeeuwen, and E. H. van den Bogaard, “3D skin models for 3R research: The potential of 3D reconstructed skin models to study skin barrier function,” *Experimental Dermatology*, vol. 27, no. 5, pp. 501–511, 2018, doi: 10.1111/exd.13531.

[204]L. Souci and C. Denesvre, “3D skin models in domestic animals,” *Veterinary Research*, vol. 52, no. 1, p. 21, Feb. 2021, doi: 10.1186/s13567-020-00888-5.

[205]V. M. Schoop, N. Mirancea, and N. E. Fusenig, “Epidermal organization and differentiation of HaCaT keratinocytes in organotypic coculture with human dermal fibroblasts,” *J Invest Dermatol*, vol. 112, no. 3, pp. 343–353, Mar. 1999, doi: 10.1046/j.1523-1747.1999.00524.x.

[206]P. Zoio, S. Ventura, M. Leite, and A. Oliva, “Pigmented Full-Thickness Human Skin Model Based on a Fibroblast-Derived Matrix for Long-Term Studies,” *Tissue Eng Part C Methods*, vol. 27, no. 7, pp. 433–443, Jul. 2021, doi: 10.1089/ten.TEC.2021.0069.

[207]A. El-Tamer *et al.*, “Development of in vitro 3D brain models on laser fabricated scaffolds,” *Transactions on Additive Manufacturing Meets Medicine*, vol. 3, no. 1, Art. no. 1, Sep. 2021, doi: 10.18416/AMMM.2021.2109532.

[208]T. Gambichler, G. Moussa, M. Sand, D. Sand, P. Altmeyer, and K. Hoffmann, “Applications of optical coherence tomography in dermatology,” *J Dermatol Sci*, vol. 40, no. 2, pp. 85–94, Nov. 2005, doi: 10.1016/j.jdermsci.2005.07.006.

[209]K. Awasthi, F.-L. Chang, P.-Y. Hsieh, H.-Y. Hsu, and N. Ohta, “Characterization of endogenous fluorescence in nonsmall lung cancerous cells: A comparison with nonmalignant lung normal cells,” *Journal of Biophotonics*, vol. 13, no. 5, p. e201960210, 2020, doi: 10.1002/jbio.201960210.

[210]L. Ferrante di Ruffano *et al.*, “Optical coherence tomography for diagnosing skin cancer in adults,” *Cochrane Database Syst Rev*, vol. 2018, no. 12, p. CD013189, Dec. 2018, doi: 10.1002/14651858.CD013189.

[211]A. Rajabi-Estarabadi *et al.*, “Optical coherence tomography imaging of melanoma skin cancer,” *Lasers Med Sci*, vol. 34, no. 2, pp. 411–420, Mar. 2019, doi: 10.1007/s10103-018-2696-1.

[212]D. C. Whiteman, W. J. Pavan, and B. C. Bastian, “The melanomas: a synthesis of epidemiological, clinical, histopathological, genetic, and biological aspects, supporting distinct subtypes, causal pathways, and cells of origin,” *Pigment Cell Melanoma Res*, vol. 24, no. 5, pp. 879–897, Oct. 2011, doi: 10.1111/j.1755-148X.2011.00880.x.

[213]C. Naidoo, C. A. Kruger, and H. Abrahamse, “Photodynamic Therapy for Metastatic Melanoma Treatment: A Review,” *Technol Cancer Res Treat*, vol. 17, p. 1533033818791795, Aug. 2018, doi: 10.1177/1533033818791795.

[214]B. I and F. Ag, “Photodynamic therapy in melanoma--an update,” *Journal of physiology and pharmacology : an official journal of the Polish Physiological Society*, vol. 63, no. 2, Apr. 2012, Accessed: Oct. 14, 2024. [Online]. Available: https://pubmed.ncbi.nlm.nih.gov/22653896/

[215]S. G. Sokolovski, S. A. Zolotovskaya, A. Goltsov, C. Pourreyron, A. P. South, and E. U. Rafailov, “Infrared laser pulse triggers increased singlet oxygen production in tumour cells,” *Sci Rep*, vol. 3, no. 1, p. 3484, Dec. 2013, doi: 10.1038/srep03484.

[216]K. Murotomi, A. Umeno, S. Sugino, and Y. Yoshida, “Quantitative kinetics of intracellular singlet oxygen generation using a fluorescence probe,” *Sci Rep*, vol. 10, no. 1, p. 10616, Jun. 2020, doi: 10.1038/s41598-020-67155-7.

[217]S. Kim, T. Tachikawa, M. Fujitsuka, and T. Majima, “Far-Red Fluorescence Probe for Monitoring Singlet Oxygen during Photodynamic Therapy,” *J. Am. Chem. Soc.*, vol. 136, no. 33, pp. 11707–11715, Aug. 2014, doi: 10.1021/ja504279r.

[218]T. NAGANO, “Development of fluorescent probes for bioimaging applications,” *Proc Jpn Acad Ser B Phys Biol Sci*, vol. 86, no. 8, pp. 837–847, Oct. 2010, doi: 10.2183/pjab.86.837.

[219]S. E. Logue, M. Elgendy, and S. J. Martin, “Expression, purification and use of recombinant annexin V for the detection of apoptotic cells,” *Nat Protoc*, vol. 4, no. 9, pp. 1383–1395, Sep. 2009, doi: 10.1038/nprot.2009.143.

[220]M. V. Shirmanova *et al.*, “Insight into redox regulation of apoptosis in cancer cells with multiparametric live-cell microscopy,” *Sci Rep*, vol. 12, no. 1, p. 4476, Mar. 2022, doi: 10.1038/s41598-022-08509-1.

[221]M. Redza-Dutordoir and D. A. Averill-Bates, “Activation of apoptosis signalling pathways by reactive oxygen species,” *Biochim Biophys Acta*, vol. 1863, no. 12, pp. 2977–2992, Dec. 2016, doi: 10.1016/j.bbamcr.2016.09.012.

[222]A. Khokhlova *et al.*, “Effects of high and low level 1265 nm laser irradiation on HCT116 cancer cells: Mechanisms of Photobiomodulation Therapy XIV,”

Proceedings of SPIE - International Society for Optical Engineering, vol. 10861, no. 108610L, Mar. 2019, doi: 10.1117/12.2509529.

[223] D. Terutsuki, H. Mitsuno, and R. Kanzaki, "3D-Printed Bubble-Free Perfusion Cartridge System for Live-Cell Imaging," *Sensors (Basel)*, vol. 20, no. 20, p. 5779, Oct. 2020, doi: 10.3390/s20205779.

[224] T. M. Tsubone, M. S. Baptista, and R. Itri, "Understanding membrane remodelling initiated by photosensitized lipid oxidation," *Biophysical Chemistry*, vol. 254, p. 106263, Nov. 2019, doi: 10.1016/j.bpc.2019.106263.

[225] M. Azmanova and A. Pitto-Barry, "Oxidative Stress in Cancer Therapy: Friend or Enemy?," *Chembiochem*, vol. 23, no. 10, p. e202100641, May 2022, doi: 10.1002/cbic.202100641.

[226] "Cellular Mechanisms of Singlet Oxygen in Photodynamic Therapy." Accessed: Dec. 13, 2024. [Online]. Available: https://www.mdpi.com/1422-0067/24/23/16890

[227] S. George, M. R. Hamblin, and H. Abrahamse, "Effect of red light and near infrared laser on the generation of reactive oxygen species in primary dermal fibroblasts," *J Photochem Photobiol B*, vol. 188, pp. 60–68, Nov. 2018, doi: 10.1016/j.jphotobiol.2018.09.004.

[228] D. Trachootham, J. Alexandre, and P. Huang, "Targeting cancer cells by ROS-mediated mechanisms: a radical therapeutic approach?," *Nat Rev Drug Discov*, vol. 8, no. 7, pp. 579–591, Jul. 2009, doi: 10.1038/nrd2803.

[229] J. Navarro-Yepes *et al.*, "Oxidative Stress, Redox Signaling, and Autophagy: Cell Death Versus Survival," *Antioxid Redox Signal*, vol. 21, no. 1, pp. 66–85, Jul. 2014, doi: 10.1089/ars.2014.5837.

[230] X. An, W. Yu, J. Liu, D. Tang, L. Yang, and X. Chen, "Oxidative cell death in cancer: mechanisms and therapeutic opportunities," *Cell Death Dis*, vol. 15, no. 8, pp. 1–20, Aug. 2024, doi: 10.1038/s41419-024-06939-5.

[231] F. Anquez, I. El Yazidi Belkoura, P. Suret, S. Randoux, and E. Courtade, "Cell death induced by direct laser activation of singlet oxygen at 1270 nm," *Laser Phys.*, vol. 23, no. 2, p. 025601, Dec. 2012, doi: 10.1088/1054-660X/23/2/025601.

[232] "TMEM16F activation by Ca2+ triggers plasma membrane expansion and directs PD-1 trafficking | Scientific Reports." Accessed: Jan. 22, 2025. [Online]. Available: https://www.nature.com/articles/s41598-018-37056-x